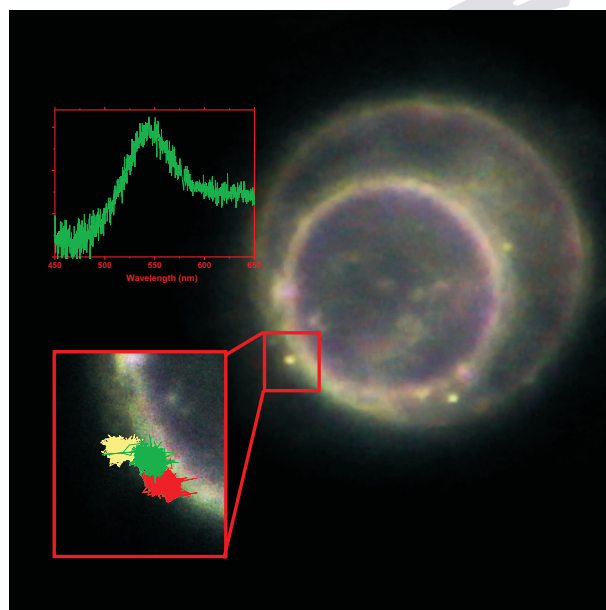

Plasmonic Heating of Gold Nanoparticles in an Optical Trap and on the Cell Membrane

Haojin Ba



München 2012

Plasmonic Heating of Gold Nanoparticles in an Optical Trap and on the Cell Membrane

Haojin Ba



München 2012

Plasmonic Heating of Gold Nanoparticles in an Optical Trap and on the Cell Membrane

Haojin Ba

Dissertation
an der Fakultät für Physik
der Ludwig-Maximilians-Universität
München

vorgelegt von
Haojin Ba
von Liaoning (China)

München
September 5th, 2012

Erstgutachter: Prof. Dr. Jochen Feldmann
Zweitgutachter: Prof. Dr. Dieter Braun
Tag der Verteidigung: October 5th, 2012

Titelbild: DFM image, scattering spectrum and diffusion trajectory of a Au NP covalently labeled to a Jurkat cell membrane.

Dedicated to God from whom all wisdom comes

List of publications

- H. Ba, J. Rodríguez-Fernández, F.D. Stefani and J. Feldmann
Immobilization of gold nanoparticles on living cell membranes upon controlled lipid binding
Nano Letters 10, 3006-3012 (2010).
- W.Ni & H. Ba, A.A. Lutich, F. Jäckel and J. Feldmann
Enhancing single-nanoparticle surface-chemistry by plasmonic overheating in an optical trap
Nano Letters Accepted (2012), DOI: 10.1021/nl301937j.
- H. Ba, J. Rodríguez-Fernández, L. Liu, A.A. Lutich and J. Feldmann
Probing the thermal sensitivity of cellular membranes by optical heating single gold nanoparticles
In preparation.

Contributions to conferences and workshops

- J. Stehr, H. Ba, C. Hrelescu, M. Wunderlich, A. Nicht, D. Heindl, K. Kurzinger and J. Feldmann
Ultrafast DNA analysis using laser heated gold nanoparticles
CeNS-NIM-SFB486 Winter School 2009 Nanosystems and Sensors, St. Anton and Arlberg, Austria, March 2009.
- H. Ba, J. Rodríguez-Fernández, F.D. Stefani and J. Feldmann
A general approach for labeling cellular membranes with CTAB-capped Au nanoparticles
E-MRS 2010 Spring Meeting, Strasbourg, France, June 2010.
- H. Ba, J. Rodríguez-Fernández, F.D. Stefani and J. Feldmann
Controlled binding of single gold nanoparticles to lipid molecules in the membrane of living cells
iNANO Autumn School of Nano-Optics, Aarhus, Denmark, September 2010.

-
- H. Ba, J. Rodríguez-Fernández, F.D. Stefani and J. Feldmann
Controlled binding of single gold nanoparticles to lipid molecules in the membrane of living cells
Annual meeting of the German Biophysical Society 2010, Bochum, Germany, October 2010.
 - H. Ba, J. Rodríguez-Fernández, F.D. Stefani and J. Feldmann
Controlled labeling of lipids with single gold nanoparticles on living cell membranes
Biophysical Society 55th Annual Meeting, Baltimore, Maryland, March 2011.
 - H. Ba
Optical manipulation on the living cell membrane
Workshop From Biophotonics to Optoelectronics, Riezlern, Austria, October 2011.

Table of Contents

Kurzfassung	xiii
Abstract	xv
1 Introduction	1
2 Fundamentals	5
2.1 Optical properties of gold nanoparticles	6
2.1.1 Dielectric properties of gold	6
2.1.2 Electrodynamics of gold nanoparticles	8
2.1.3 Surface plasmons of gold nanoparticles	11
2.2 Optothermal properties of gold nanoparticles	15
2.2.1 Optical heating of gold nanoparticles	15
2.2.2 Thermal heating of the surrounding	16
2.2.3 The Finite-Element Method	17
2.3 Optical trapping of gold nanoparticles	19
2.4 Biological membranes	22
2.4.1 Lipid bilayers and cellular membranes	22
2.4.2 Lipid membrane melting	24
2.4.3 Lipid diffusion	25
3 Experimental setups and sample preparation	29
3.1 Experimental Setups	30
3.1.1 Laser-equipped dark field microscope for trapping and heating	30
3.1.2 UV-Vis-NIR spectroscopy	31
3.1.3 Dynamic light scattering and ζ -potential	31
3.1.4 Electron microscopy	32

Table of Contents

3.1.5	FTIR microscopy	32
3.2	Sample preparation	32
3.2.1	Synthesis and oxidation of CTAB stablized gold nanorods	32
3.2.2	Synthesis and growth of CTAB stabilized gold nanospheres	33
3.2.3	Immobilization of gold nanoparticles on living cell membranes via covalent binding	35
4	Enhancing single gold nanoparticle surface-chemistry by plasmonic overheating in an optical trap	41
4.1	Single gold nanorod oxidation in an optical trap	42
4.1.1	Oxidation conditions: oxidant concentration and temperature effect	43
4.1.2	Single gold nanorod oxidation in an optical trap	45
4.2	Accelerated growth of single Au nanospheres in an optical trap . .	50
4.3	Characterization of the optical trap	53
4.3.1	Characterizing the optical trapping force	53
4.3.2	The optothermal effect in the optical trap	58
4.4	Conclusions	60
5	Optothermal manipulation of gold nanoparticles on cell membranes	61
5.1	Covalent labeling of cell membranes with gold nanoparticles . . .	62
5.2	Optothermal manipulation of gold nanoparticles on cell membranes	70
5.2.1	Gold nanoparticle diffusion on living cell membranes . . .	70
5.2.2	Optothermal manipulation of gold nanoparticle diffusion on cell membranes	73
5.3	Conclusions	78
6	Conclusions and outlook	81
	Bibliography	83
	Acknowledgements	99

Kurzfassung

Plasmonisches Heizen, eine nichtstrahlende Relaxation von Elektronenschwingungen in metallischen Nanopartikeln nach Anregung durch ein elektromagnetisches Feld, erhöht die Temperatur des Nanoteilchens und seiner Umgebung. Die optische Manipulation der lokalen Temperatur in der Nähe des Nanoteilchens hat aufgrund der Anwendung in der Pharmako- und Krebstherapie große Aufmerksamkeit erfahren. Goldnanoteilchen haben sich aufgrund ihrer faszinierenden Eigenschaften als geeignete Kandidaten für die Anwendung des plasmonischen Heizens erwiesen. Oberflächenplasmonen, die kollektiven Elektronenschwingungen an der Grenzfläche zwischen Gold und Dielektrikum als Antwort auf eine externe Anregung, ermöglichen Anwendungen in der Sensorik und Bildgebung. Zusätzlich machen die chemische Stabilität und die einfach zu verändernde Oberflächenchemie Goldnanoteilchen zu attraktiven Biomarkern.

In dieser Dissertation wird plasmonisches Heizen von Goldnanoteilchen angewandt um ihre Oberflächenreaktivität in einer optischen Falle zu manipulieren. Optisches Einfangen von Goldnanoteilchen mit einem Einzelstrahl erlaubt die Untersuchung von Goldnanoteilchen auf Einzelteilchenebene ohne sie an feste Oberflächen anzuheften. Der plasmonische Heizeffekt auf das Teilchen kann die lokale Temperatur des gefangenen Teilchens über die Siedetemperatur des Lösungsmittels anheben, wodurch er die Reaktionen des Einzelteilchens in der Falle verändert und beschleunigt. Unter bestimmten Intensitäten des Fallenlasers erhöht die Oxidation des einzelnen Nanostäbchens sein Aspektverhältnis, während die Oxidation im Ensemble dieses verringert. Die kritische Rolle der Teilchentemperatur ist zudem durch das Wachsen einzelner Nanokugeln in der Falle bestätigt. Dabei wird das gefangene Seedpartikel erhitzt, wodurch es schneller wächst und größere Teilchen erzeugt werden als durch das Wachstum in Ensembleexperimenten.

Der Effekt des plasmonischen Heizens wird zudem für die Manipulation von Zellmembranen benutzt, indem die lokale Temperatur von Nanoteilchen-markierten Zellmembranen verändert wird. Eine neue Strategie zum Binden von Goldnanoteilchen an lebende Zellmembranen basierend auf Vesikel/Zellmembran Fusogenese wird vorgestellt. Im Vergleich zu anderen Bindungsstrategien, ermöglicht das stabile, kovalente Anheften der Nanoteilchen an die Lipidmoleküle plasmonisches Heizen und optische Manipulation auf lebenden Zellmembranen, ohne die Partikel-Zellmembran Verbindung aufzubrechen. Die optothermische Manipulation der Goldnanoteilchen beschleunigt die Diffusion der Lipid-markierten Goldnanoteilchen auf Zelloberflächen. Sowohl Diffusionskoeffizient als auch Diffusionsfläche nehmen durch optisches Heizen dramatisch zu. Kovalent an Zellmembranen angeheftete Goldnanoteilchen bieten damit multifunktionelle Werkzeuge für die Untersuchung und Fernmanipulation von lebenden Zellen.

Abstract

Plasmonic heating, a non-radiative relaxation of electron oscillations in metallic nanoparticles upon applied electromagnetic field, elevates the temperature of the whole nanoparticle and its surroundings. Optical manipulation of local temperatures near nanoparticles has received great interest for its application in drug delivery and cancer therapy. Gold nanoparticles have emerged as suitable candidates for plasmonic heating applications due to their fascinating properties. Surface plasmons, the collective electron oscillations at the gold/dielectric interface in response to the external excitation, enable applications in sensing and imaging. Moreover, the chemical stability and easy modifiable surface chemistry of gold nanoparticles make them appealing markers for biological samples.

In this thesis, plasmonic heating of gold nanoparticles is applied to manipulate the surface reactivity of gold nanoparticles in an optical trap. Single beam optical trapping allows the investigation of gold nanoparticles at the single particle level without attaching them to any solid interface. The plasmonic heating effect on the particle can elevate the local temperature of the trapped particle above the boiling temperature of the solvent, thus modifies and accelerates the single particle reactions in the trap. Under certain trapping power, the oxidation of single gold nanorod increases its aspect ratio, while the oxidation in bulk decreases it. Additionally, the critical role of the particle temperature is verified by growing single nanospheres in the trap, in which the trapped seed particle is heated and thus grows faster and yields bigger particle than in bulk.

The plasmonic heating effect is further used for the manipulation of cellular membranes by changing the local temperature of gold nanoparticle-labeled cellular membranes. A new strategy to bind gold nanoparticles to living cell membranes based on vesicle/cell membrane fusogenesis is introduced. With respect to other binding strategies, the stable covalent binding between the nanoparticle and the thiolated lipid molecule enables the possibility to perform plasmonic heating and optical manipulation on the living cell membrane, without breaking the particle-cell membrane linkage. The optothermal manipulation of gold nanoparticles accelerates the diffusion of lipid-labeled gold nanoparticles on cell surfaces. Both the diffusion coefficient and the diffusion area increase dramatically during optical heating. Gold nanoparticles covalently labeled on cell membranes provide multifunctional tools for the investigation and remote manipulation of living cells.

1 Introduction

Metallic nanoparticles, especially gold nanoparticles, have received tremendous attention due to their distinctive properties and potential applications in a wide range of fields. The history of gold nanoparticle applications dates back to the Romans' time.[1] However, colloidal gold did not draw the attention of modern scientists until the first synthesis of a pure gold colloidal solution by Michael Faraday in 1857.[2] Extensive explorations of gold nanoparticles started after John Turkevich developed a method to synthesize gold nanospheres with homogeneous sizes.[3] Gold nanoparticles with different shape, size, surface coating or even core-shell structures, have been synthesized and their properties have been explored.[4–7]

Among all the fascinating properties of gold colloids, their optical properties have been the most intriguing. The characteristic optical properties of gold nanoparticles are attributed to the nanoparticle surface plasmons, which are the excitation of collective electron oscillations at the interface between gold and the dielectric. As the external excitation frequency approaches the natural resonance frequency of the nanoparticle, the electron oscillations amplify significantly. This resonance is called the localized surface plasmon resonance. The extinction cross-section reaches the maximum at the resonance frequency, so is the enhancement of electromagnetic fields in the near-field of the nanoparticles.[8] Gold nanoparticles are therefore applied to the enhancement of fluorescence, Raman scattering, due to this field-enhancement near the plasmon resonance.[4, 9–11] The plasmonic heating effect, a non-radiative decay of the absorbed electromagnetic excitation into the metal lattice, results in the thermalization of the whole nanoparticle and elevates the local temperature at and near the gold nanoparticles. Such effect, also named the photothermal effect, has been of great interest due to their application in drug delivery and cancer therapy.[12–15]

Optical trapping, the manipulation of small matter using a focused laser beam, has been widely established in physics, chemistry and biology. Ever since the first reported optical trapping of metallic nanoparticles in 1994,[16] this field has attracted more and more attention.[17–20] Optical trapping of nanoparticles in three dimensions provides a contact-less method to manipulate them while keeping the possibility to investigate them in solution without being immobilized to any solid interface.

Another appealing and notable application is to use gold nanoparticles as biological markers. Due to their chemical stability and modifiable surface chemistry, the surface of gold nanoparticles can be modified to obtain the functionality to label biological molecules such as proteins, antigens and DNA.[21–24] The detection of gold markers in biological samples benefits from the optical properties of gold nanoparticles. Optical microscopes have been mostly used to detect gold nanoparticles in biological environments, such as the dark field microscope due to their large scattering cross-sections.[5, 25, 26]

The scope of this thesis is to apply the plasmonic heating effect of gold nanoparticles to the manipulation of single nanoparticle reactions in an optical trap, and gold nanoparticles labeled to cellular membranes. The 3D optical confinement of a single gold nanoparticle by optical trapping allows the investigation of the kinetics of chemical reactions at the single nanoparticle level, such as nanoparticle oxidation and growth. The trapping laser not only takes control over the particle movement, but also induces the plasmonic heating effect on the particle. The temperatures of the trapped gold nanoparticles can exceed the boiling temperature of water (i.e. 100°C), which accelerate and modify the kinetics of surface chemical reactions on the gold nanoparticle surface.

The plasmonic heating of gold nanoparticles has been reported to induce local phase transition on artificial vesicles.[27] Here the application of gold nanoparticle plasmonic heating is further introduced to living cell membranes. A controlled and versatile labeling method based on gold nanoparticles covalently binding to fusogenic vesicles prior to vesicle/cell membrane fusogenesis is introduced. With respect to other binding strategies, such as protein-mediated binding, this strategy relies on the gold nanoparticle-lipid binding via thiol-maleimide reaction, which is stable under optical heating experiments and keeps the sensing properties of the nanoparticle. The lipid-labeling gold nanoparticle serves both as an optical marker to track lipid diffusion and as a local heating source for laser manipulation. Upon optical heating, the local temperature of the gold nanoparticle and its surrounding cellular membrane increases, accelerating the diffusion of gold-labeled lipid through a larger area in comparison to that without heating.

The fundamentals to understand this thesis are introduced in Chapter 2. The optical properties, especially the surface plasmons of gold nanoparticles are presented. The optically induced thermal effect of gold nanoparticles, and theoretical models to calculate the temperature change in the nanoparticle and its surroundings are further explained. The basis for optical trapping of plasmonic nanoparticles are also presented there. Thereafter, biological membranes, in particular cellular membranes, are introduced.

In Chapter 3 the experimental setups employed are introduced first. A dark field microscope equipped with laser for optical trapping and heating is presented.

In the second part, the sample preparation procedures are described in detail. The synthesis of CTAB-stabilized gold nanospheres and gold nanorods, as well as experimental details for single particle reactions in an optical trap are presented. After this, the preparation of labeling gold nanoparticles onto lipids in the living cell membrane is explained.

In Chapter 4 plasmonic heating of single gold nanoparticles in an optical trap is applied to modify the surface reactivity of the heated nanoparticle. A stable optical trapping provides a stable free standing single particle and the possibility to investigate single particle reactions, such as particle oxidation and particle growth, under the influence of plasmonic heating. Gold nanorods oxidation in bulk is performed and compared to the results of single nanorod oxidation in an optical trap. Thereafter, single gold nanosphere growing experiments are shown and discussed. In addition, the properties of the optical trap are characterized: the optical forces and the temperature of the nanoparticle in the trap.

In Chapter 5, gold nanoparticles are employed as both lipid markers and local heaters on living cell membranes. First, the gold nanoparticles are covalently labeled to living cell membranes, which endures the nanoparticle optical heating experiment without breaking the particle-membrane linkage. Then, the optothermally manipulated cellular membrane is investigated by tracking the motion of the lipid-labeled gold nanoparticles using dark field microscopy.

2 Fundamentals

The fundamentals of gold nanoparticles, optical trapping and biological membranes to understand this thesis are presented in this chapter. The optical properties of Au NPs, especially their surface plasmon resonance behavior, are introduced in the first section. Among all the shapes, the fundamental plasmonic properties of spherical and rod shaped nanoparticles are explained. In the second section, the plasmonic thermal effect, as a result of non-radiative relaxation of electron oscillations in the nanoparticle lattice, is explained. The theoretical method for calculating temperature distributions around plasmonically heated nanoparticles is introduced. The third section presents fundamentals of single beam Optical Tweezers and the optical trapping of nanometer size particles. Biological membranes, especially cellular membranes, are introduced in the fourth section of this chapter.

2.1 Optical properties of gold nanoparticles

Gold, a noble metal, is dense, non-transparent and resistant to oxidation and acid corrosion. Due to its robust chemical properties and its shiny appearance, gold has a long history of civil applications in jewelry, coins, and arts. The Romans are known to be the first using Au NPs (or colloidal gold) to stain glasses. For instance, the *Lycurgus Cup* (Figure 2.1), a glass embedded with 5 - 60 nm gold/silver alloy particles, changes its color depending on the illumination mode. The color of the glass appears green when it is illuminated from the outside, such as under the daylight. However, the glass appears red, when the illuminated light transmits through the glass. The fascinating colorful property comes from the optical properties of nanoparticles in the stained glass.

Figure 2.1: The *Lycurgus Cup*, shows green color when illuminated under daylight (left), and turns red when a light source is put inside the cup and shines through the glass (right). Reproduced with permission from [1].



2.1.1 Dielectric properties of gold

Gold belongs to the 11th group in the periodic table. Due to its completely filled valence bands (f and d), and partially filled conduction band (sp conduction band), [28] gold can be denoted as free-electron metal and its optical properties can be estimated by the Drude-Lorentz-Sommerfeld model. This model treats the electrons as ideal electron gas.[29] The interactions between electrons are neglected and the macroscopic behavior is calculated by multiplying the effect of a single electron with the number of electrons. The response of a free electron of mass m_e and charge e to an external field $\vec{E} = \vec{E}_0 e^{-i\omega t}$ is described as follows:

$$m_e \frac{\partial^2 r}{\partial t^2} + m_e \Gamma \frac{\partial r}{\partial t} = e \vec{E}_0 e^{-i\omega t}, \quad (2.1)$$

where Γ is the damping constant describing the relaxation time of the free electron in the external electric field. The mean free time $\tau = \Gamma^{-1}$ describes the relaxation process. Equation 2.1 describes the conduction band electrons and is valid for $\omega > 0$. This equation is extended to bound electrons by adding a

linear restoring force determining the eigenfrequency of the oscillating electron. Solving the equation above gives the dipole moment of a single electron $\vec{p} = e\vec{r}_0$ and the polarization $\vec{P} = n\vec{p}$, for the number of electrons per unit volume n . By definition, the dielectric function $\varepsilon(\omega) = \varepsilon_1(\omega) + i\varepsilon_2(\omega)$ is related to \vec{P} through $\varepsilon = 1 + P/(\varepsilon_0 E)$, while $\sqrt{\varepsilon} = n + ik$ and $\vec{P} = n\alpha\vec{E}$ for polarizability α , the dielectric function $\varepsilon(\omega)$ of a system of n free electrons per unit volume can be written as

$$\varepsilon(\omega) = 1 - \frac{\omega_P^2}{\omega^2 + i\Gamma\omega} = 1 - \frac{\omega_P^2}{\omega^2 + \Gamma^2} + i\frac{\omega_P^2\Gamma}{\omega(\omega^2 + \Gamma^2)}, \quad (2.2)$$

where $\omega_p = (ne^2/\varepsilon_0 m_e)^{1/2}$ is the Drude plasma frequency. The damping constant Γ is related to the electron mean free path ℓ and the Fermi velocity v_F by $\Gamma = v_F/\ell$. When $\omega \gg \Gamma$, the real and imaginary part of $\varepsilon(\omega)$ can be written as

$$\varepsilon_1(\omega) \approx 1 - \frac{\omega_P^2}{\omega^2}, \varepsilon_2(\omega) \approx \frac{\omega_P^2}{\omega^3}\Gamma, \quad (2.3)$$

The dielectric function can also be expressed by susceptibility χ , $\varepsilon(\omega) = 1 + \chi^{DS}(\omega)$, where $\chi^{DS}(\omega)$ is the free-electron Drude-Sommerfeld susceptibility.

The Drude model only considers the independent behavior of conduction band electrons. However, the contributions from the bound electrons, the interband processes, the direct excitation of $5d$ -band electrons into the conduction band $6sp$, are not negligible. Thus the dielectric function needs to be modified by the addition of the interband transition given as the interband susceptibility $\chi^{IB}(\omega)$:

$$\varepsilon(\omega) = 1 + \chi^{DS}(\omega) + \chi^{IB}(\omega). \quad (2.4)$$

The Drude model theoretically describes the interaction between electrons in the metal and the incoming electromagnetic field. Johnson and Christy have experimentally determined the permittivity of thin gold films.[30] The theoretical expansion of the Drude model (equation 2.4) matches well with the experimental results. Therefore, the experimental permittivity is used for further calculations.

In the previous discussion, the dielectric function has been considered as size-independent. However, the dielectric function is size-independent only when the particle satisfies $r \geq 10$ nm (extrinsic size effects). For particles smaller than 10 nm, the intrinsic size effects influence the dielectric function and give $\varepsilon = \varepsilon(\omega, r)$. In this work, the radius of the nanoparticles is larger than 10 nm and their dielectric function is considered as size-independent.

2.1.2 Electrodynamics of gold nanoparticles

Maxwell's equations successfully describe the propagation of electromagnetic waves in free space.[31] In order to treat the interaction between electromagnetic field and nanoparticles, Maxwell's equations were solved. Mie theory, developed by German physicist Gustav Mie and Danish physicist Ludvig Lorenz independently, is used to solve the electromagnetic wave propagating through spheres with sizes comparable to the wavelength. A simpler Quasi-Static model gives rough estimates of the particle resonance. Based on the Quasi-Static model, Richard Gans solved the extinction properties of spheroidal or ellipsoidal nanoparticles known as the Gans theory. Numerical approaches, such as finite-difference time-domain method, are employed to describe the absorption and scattering of light particles with arbitrary sizes and shapes.

2.1.2.1 The Mie theory

In 1908 Gustav Mie developed his rigorous solution of Maxwell's equation for spheres of arbitrary sizes, known as the Mie theory. [32, 33] Mie theory describes the interaction between a plane wave and a homogeneous sphere. Spherical coordinates are introduced to the electromagnetic field and the boundary conditions are set at the sphere-medium interface. Due to the spherical symmetry of the system, a multipole expansion of the field components gives the cross-sections in the form of infinite series:

$$C_{sca} = \frac{2\pi}{|k|^2} \sum_{n=1}^{\infty} (2n+1)(|a_n|^2 + |b_n|^2), \quad (2.5)$$

$$C_{ext} = \frac{2\pi}{|k|^2} \sum_{n=1}^{\infty} (2n+1)\Re(|a_n| + |b_n|), \quad (2.6)$$

with the Mie coefficients a_n and b_n expressed as:

$$a_n = \frac{m\psi_n(mx)\psi'_n(x) - \psi_n(x)\psi'_n(mx)}{m\psi_n(mx)\xi'_n(x) - \xi_n(x)\psi'_n(mx)}, \quad (2.7)$$

$$b_n = \frac{\psi_n(mx)\psi'_n(x) - m\psi_n(x)\psi'_n(mx)}{\psi_n(mx)\xi'_n(x) - m\xi_n(x)\psi'_n(mx)}, \quad (2.8)$$

where ψ_n and ξ_n are Riccati-Bessel cylindrical functions, $m = n/n_m = \sqrt{\epsilon_r}$ is the ratio of the refractive index of the particle to that of the surrounding medium. \vec{k} is the wave vector of the propagating electromagnetic wave. $x = |k|r = 2\pi r/\lambda$ is the product of wave vector and particle radius r , which can be expressed as the ratio of the particle radius to the wavelength of the scattered light λ . n is

the multipole order, and $n = 1$ corresponds to the dipole contribution, $n = 2$ corresponds to the quadrupole contribution, $n \geq 3$ correspond to higher order contributions. The absorption cross-section can be obtained from the following relationship:

$$C_{ext} = C_{abs} + C_{scat}. \quad (2.9)$$

MQMie, a software based on the Mie theory has been used to calculate optical properties of spherical nanoparticles analytically.[34] In this work, the extinction, absorption and scattering properties of spherical Au NPs were calculated using MQMie.

2.1.2.2 The Quasi-Static model and the Gans theory

The Mie theory gives an exact electrodynamic calculation for spheres, while the quasi-static model neglects the higher multipoles and phase retardation in the quasi-static regime. This reduces the complexity in the Mie calculations and enables a quick estimation of the particle response. In the Quasi-Static model, the size of the particle is much smaller than the incident wavelength ($r \ll \lambda$), and the electromagnetic field is assumed to be spatially constant (homogeneous electromagnetic field in the particle). Therefore the collective displacement of the conduction electrons in the particle is considered as one polarized dipole moment \vec{p} induced by the external field: [8]

$$\vec{p} = 4\pi\epsilon_0\epsilon_m r^3 \frac{\epsilon - \epsilon_m}{\epsilon + 2\epsilon_m} \vec{E}_0. \quad (2.10)$$

Within the equation, ϵ and ϵ_m are the dielectric function of the particle and the medium, respectively. By introducing $p = \epsilon_0\epsilon_m\alpha E_0$ into equation 2.10, the static polarizability of the sphere is expressed as follows:

$$\alpha = 4\pi\epsilon_0 r^3 \frac{\epsilon - \epsilon_m}{\epsilon + 2\epsilon}. \quad (2.11)$$

The scattering and extinction cross-sections can be written based on the relation of $\alpha = \alpha' + i\alpha''$ as:[29]

$$C_{sct} = \frac{|k|^4}{6\pi} \left| \frac{\alpha}{\epsilon_0} \right|^2, \quad (2.12)$$

$$C_{ext} = |k| \Im \left(\frac{\alpha}{\epsilon_0} \right). \quad (2.13)$$

In the quasi-static regime, the temporal dependence of the electromagnetic field is obtained. Hence, the complex terms ϵ and ϵ_m in equations 2.10 and 2.11 are replaced by frequency dependent values $\epsilon(\omega)$ and $\epsilon_m(\omega)$. Equation 2.11 is known as the Clausius-Mossotti equation. The extinction cross-section of a particle with

volume $V_0 = 4/3\pi r^3$ can be given as:

$$C_{ext}(\omega) = 9 \frac{\omega}{c} \varepsilon_m^{3/2} V_0 \frac{\varepsilon_2(\omega)}{[\varepsilon_1(\omega) + 2\varepsilon_m]^2 + \varepsilon_2(\omega)^2}. \quad (2.14)$$

Both the dipole moment and the polarizability show resonance behavior when $|\varepsilon + 2\varepsilon_m|$ is minimum (or $[\varepsilon_1(\omega) + 2\varepsilon_m]^2 + [\varepsilon_2(\omega)]^2$ is minimum). This means that a negative ε_1 is required, or in the case of small or slowly varying ε_2 , the resonance condition is satisfied when

$$\varepsilon_1(\omega) = -2\varepsilon_m. \quad (2.15)$$

This relationship is called the Froehlich Condition. For a sphere (the dielectric function as shown in equation 2.3) located in air, the position of the resonance can be approximated to be

$$\omega_1 = \omega_p / \sqrt{3}. \quad (2.16)$$

For ellipsoidal particles, Richard Gans developed the Gans theory based on the Quasi-Static Model.[35] The polarizability along the i axes ($i = a, b, c$) of the ellipsoid is derived from equation 2.11 as:

$$\alpha_i(\omega) = 4/3\pi\varepsilon_0 abc \frac{\varepsilon(\omega) - \varepsilon_m}{\varepsilon_m + P_i(\varepsilon(\omega) - \varepsilon_m)}, \quad (2.17)$$

where P_i is the geometrical depolarization factor for axis i , and $\sum_i P_i = 1$. For a prolate spheroid, $a > b = c$, P_i is a function of the eccentricity $e = \sqrt{(a^2 - b^2)}/a$:

$$P_a = \frac{1 - e^2}{e^2} \left(\frac{1}{2e} \ln \frac{1 + e}{1 - e} - 1 \right), P_b = P_c = \frac{1 - P_a}{2}. \quad (2.18)$$

For small or slowly varying ε_2 , similar to spheres, the resonance condition for ellipsoids is satisfied when $\varepsilon_1(\omega) = -\frac{1-P_i}{P_i}\varepsilon_m$, and the resonance position $\omega_1 = \omega_p P_i$. The extinction cross-section of the prolate spheroid is then expressed as follows:[29]

$$C_{ext}(\omega) = 4/3\pi\varepsilon_0 abc \frac{k\varepsilon_m^{3/2}}{3} \sum \frac{(1/P_i^2)\varepsilon_2}{(\varepsilon_1 + \varepsilon_m(1 - P_i)/P_i)^2 + \varepsilon_2^2}. \quad (2.19)$$

Gans theory calculates the approximate resonance of the ellipsoidal nanoparticles, while most synthesized nanorods are cylindrical ellipsoids. An exact calculation of the nanorods can be performed with numerical methods, such as Finite-Difference Time-Domain (FDTD) method. FDTD solves the Maxwell's equations on a discretized spatial grid based on the algorithm originally proposed by Kane Yee and refined by Sullivan and Taflove.[36–38] Details of the FDTD algorithm

can be found in several reports.[39–42] In this work, a Lumerical software based on the FDTD method [43] has been used to calculate the electromagnetic field, and estimate the cross-sections of the gold nanorods, the laser spot size through objectives, and the optical trapping forces (see section 2.3).

2.1.3 Surface plasmons of gold nanoparticles

The Quasi-Static model describes the collective displacement of electrons in the nanoparticles due to an external electric field, which gives rise to polarized charges at the surface of the nanoparticle and to a restoring force. As shown in Figure 2.2, in a spherical nanoparticle, the conduction band electrons oscillate with respect to the positive ions. The generated surface polarization produces a restoring force, which determines the eigenfrequency of the system, termed ω_1 as in equation 2.16 for nanoparticles in the free space. The collective electron gas oscillations at the metal-dielectric interface is called the surface plasmons. When the frequency of the external electric field is close to the eigenfrequency of the collective electron oscillation, the oscillation reaches the maximum. This phenomenon is called the localized surface plasmon and the resonance frequency named localized surface plasmon resonance or the plasmon resonance. As the nanoparticle is described as a dipole, the Quasi-Static model is also called the Dipole Approximation.

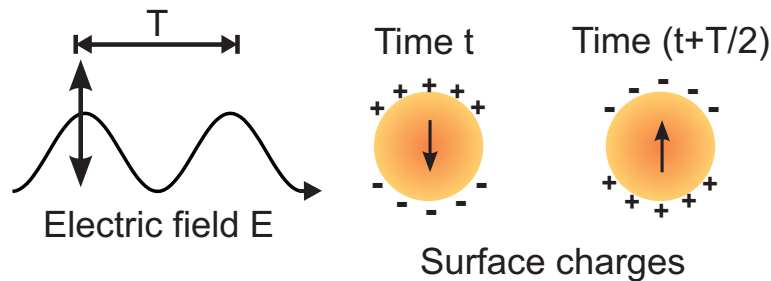


Figure 2.2: The dipolar surface plasmon of a nanoparticle excited by an electromagnetic field $E = E_0 e^{-i\omega t}$. The surface charges oscillates with the electric field E with a frequency $\omega = 1/T$.

The oscillation of nanoparticle plasmon is damped on a time scale of 10 femto-seconds.[4, 44, 45] The damping process is due to scattering of electrons at electrons, phonons, lattice defects (grain boundaries, dislocations and impurities), etc.[46] Assuming the relaxation processes i are independent, the Mathiessen rule can be applied to the damping constant Γ , and the mean free time τ can be

expressed as below:[47]

$$\Gamma = \tau^{-1} = \sum_i \tau_i^{-1} = \tau_{point\ defects}^{-1} + \tau_{dislocations}^{-1} + \tau_{grain\ boundaries}^{-1} + \tau_{e-phonons}^{-1} + \tau_{e-e}^{-1}. \quad (2.20)$$

The ultrafast damping of particle plasmons is attributed to two effects: the radiation damping and the non-radiative damping (Landau damping). In the radiation damping the dipole energy is lost by re-radiation, causing coherent scattering, which can be detected in the far-field as luminescent light. The decay rate of photon emission (γ) for nanoparticles is size-dependent (for nanospheres $\gamma \propto r^3$), as a result of increased coupling to the radiation field with increased particle size.[48–51]

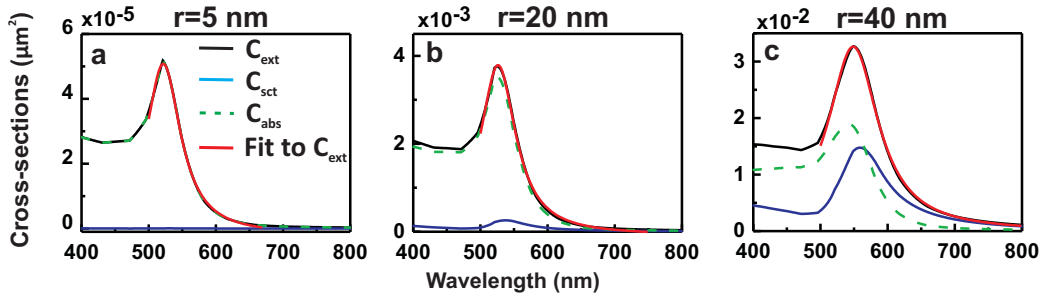


Figure 2.3: MQMie calculations of extinction (black solid), scattering (blue solid) and absorption (green dashed) cross-sections of Au nanospheres with radius (a) 5 nm, (b) 20 nm and (c) 40 nm, respectively. The extinction resonance and FWHM are determined by Lorentz fittings to the extinction cross-sections against excitation wavelength (red solid).

In the non-radiative damping process, the dipole energy decayed into electron-hole pairs, leading to the excitation of intraband electron-hole pairs and interband electron-hole pairs. The decay into interband electron-hole pairs occurs when the energy of particle plasmon is higher than the energy distance between the d-band and the Fermi edge in the sp-band. For Au nanospheres, the interband absorption from d-band to the Fermi edge is 2.38 eV and the interband decay is possible. Thereafter, thermalization occurs in the Fermi-sea, due to the electron-electron scattering of the excited electrons and holes that possess much higher energies than the thermal distribution of the Fermi-sea. The thermalization process is in the range of 1 picosecond.[52] Subsequently, on the time scale of 4 picosecond, the thermal energy in the conduction band electrons is transferred to the lattice of the nanoparticle due to electron-phonon scattering. The thermalization effect induced by the energy decay will be discussed in more details in section 2.2.

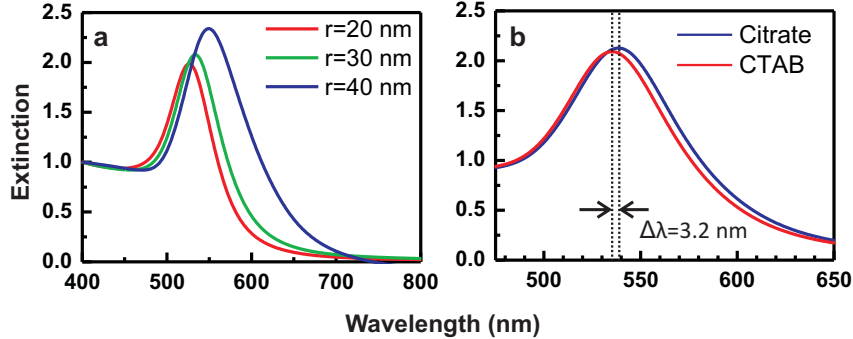


Figure 2.4: Extinction spectra of (a) citrate surface stabilized $r=20$ nm (red), 30 nm (green), 40 nm (blue) Au nanoparticles in water and (b) $r=30$ nm Au nanoparticles with citrate (blue) and CTAB (red) as surface stabilizers. Lorentz fitting of the spectra give the plasmon resonances: $\lambda_{20nm}=526nm$, $\lambda_{30nm}=535nm$, $\lambda_{40nm}=552nm$ for citrate stabilized spheres, and $\lambda_{30nm}=538.2nm$ for CTAB stabilized $r=30nm$ spheres. The plasmon resonance wavelength shifted from citrate-Au to CTAB-Au by $\Delta\lambda=3.2nm$.

Now we will discuss the parameters that influence the plasmon band. The extinction cross-section of nanoparticles (equation 2.14) can be written as a function of ω_1 and Γ : [29]

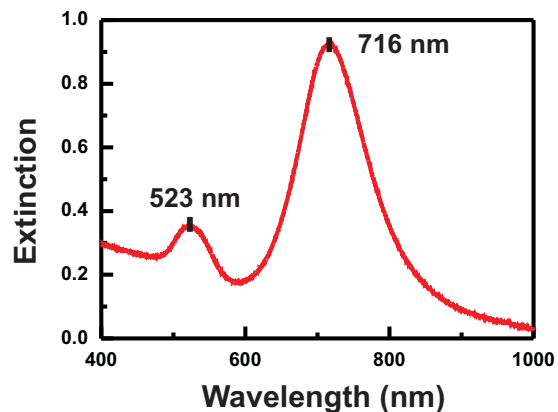
$$C_{ext} = C_o \frac{1}{(\omega - \omega_1)^2 + (\Gamma/2)^2}. \quad (2.21)$$

For free electron metals with $\omega \ll \Gamma$ ($2r < 25$ nm for gold [29]), only the dipole absorption contributes to the extinction cross-section of the nanoparticles. This is also proven by the MQMie calculation of $r=5$ nm Au nanoparticle, as shown in Figure 2.3a. In this size range, the plasmon resonance position and shape can be well approximated by equation 2.15. As for the Au nanoparticle in Figure 2.3a, the plasmon resonance wavelength calculated from the quasi-static theory is 521 nm, the same as that from the Mie theory. In the vicinity of the resonance, the extinction peak can be described by a Lorentzian and the band width is determined by the damping constant Γ . As discussed above, the plasmon damps on a time scale of 8 femtoseconds. Due to Fourier theory, this damping corresponds to a broad resonance with a full width half maximum (FWHM) of 160 meV, corresponds to a FWHM of around 50 nm in the extinction spectrum.

For larger Au NPs ($2r > 25$ nm), the extinction cross-section contains the contribution from multipole absorptions and scattering. The damping is thus retarded by these multipole oscillations at different energy levels, and the plasmon

band width is broadened. As the nanoparticles become larger, the plasmon resonance shifts to lower energies, and the bandwidth increases due to a dramatical shift and broadening of the scattering cross-section. This is clearly shown in the MQMie calculations (Figure 2.3b and c) as well as experimental measurement of Au nanospheres in water solution (Figure 2.4a). In Figure 2.3b and c, the contribution from scattering becomes significant with the increase of particle size, and the broadening of the plasmon band is induced by increasing contributions from the higher multipoles. With increasing particle size, the plasmon resonance red-shifts. The extinction resonances of experimental values (Figure 2.4a) match well with the Mie calculations.

Figure 2.5: The extinction spectrum of $80 \times 30 \times 30$ nm Au nanorods in water solution. The longitudinal plasmon resonance is 716 nm, and the transversal plasmon resonance is 523 nm.



Apart from the intrinsic parameters of the nanoparticle, such as size, shape and material that determine the plasmon band position and shape, the extrinsic parameters, such as the dielectric constant of the surrounding medium ϵ_m and the nanoparticle surface charge also shift the spectral plasmon resonance position. With increasing ϵ_m , the surface charge of the nanoparticle decreases correspondingly. The polarization on the particle surface is partially compensated by the polarization of the medium. This decrease in the polarization leads to a smaller restoring force, which red-shifts the plasmon resonance wavelength. The nanoparticle surface stabilizing molecules also influences the plasmon position and width. [49, 53] As shown in Figure 2.4, a resonance shift of 3.2 nm and broadening of the plasmon band is found in the extinction spectra of $r = 30$ nm Au nanospheres with two different types of surface stabilizing molecules. It is difficult to use the change of ϵ_m as an explanation, since the single- or double-layered surface molecules can hardly modify the medium permittivity. Interface damping, which is the energy transfer between cluster and the surface molecules by temporary charge-transfer reactions, was identified as the main reason for such phenomenon. The excited conduction electrons collide with the lattice interface and temporar-

ily shift into the "affinity levels" of the surrounding chemicals and then transfer back to the lattice. This temporal residence of electrons in the surface molecules could disturb the phase coherence of the collective excitation, hence induces plasmon resonance shift. The interface damping increase the damping lifetime, which consequently expands the plasmon band.

As for Au nanorods with $a > b = c$, as shown in Figure 2.5, $a=80$ nm, $b=c=30$ nm, two characteristic plasmon bands present the oscillation along the a axis (longitudinal mode) and perpendicular to the a axis (transversal mode). For this nanorod in water ($n = 1.33$), $P_a = 0.126$, $P_b = P_c = 0.437$ (according to equation 2.18), and the plasmon resonant wavelengths are $\lambda_a=523$ nm, $\lambda_b = \lambda_c=716$ nm.

2.2 Optothermal properties of gold nanoparticles

2.2.1 Optical heating of gold nanoparticles

The optical heating of Au NPs is a result of optically induced oscillations in the nanoparticle lattice. As discussed in section 2.1.3, the collective oscillations of electrons in response to the applied electromagnetic field contributes to the extinction spectrum of Au NPs. The width of the extinction spectrum is determined by the decay time of the surface plasmon, which is on the time scale of 10 femtosecond. Femtosecond laser pulse excitation had been applied to investigate the physical reasons for this ultrafast dephasing.[4, 45, 54] Two processes contribute to the plasmon decay: the radiative decay into photon emission and the non-radiative decay. The latter process finally induces the thermalization.

In the non-radiative decay process, electron thermalization occurs first, then the energy is transferred from the electrons to the lattice, homogeneously heating the whole nanoparticle. Upon external electromagnetic field excitation, conduction electrons are excited to higher energy states, forming a broad non-Fermi distribution of electrons with energies up to the pump energy above the Fermi level (nonthermalized distribution). The "hot" electrons then couple with each other to exchange energy and form an internally thermalized distribution state. The temperature of electrons at this state can reach several thousand degrees Celsius. This internal thermalization of the "hot" electrons is also known as electron-electron coupling (also see equation 2.20). Such process occurs on the time scale of 1 picosecond.[52, 55] Afterwards, the absorbed energy is further relaxed by electron-phonon coupling, known as the external thermalization. This process starts during the internal thermalization process, and has a time constant of 1-3 picosecond.[55–57] The thermalized electrons and phonons then transfer the energy into the lattice, and the whole nanoparticle reaches a thermal equilib-

rium. This process occurs on the time scale above 50 picosecond, depending on the particle size.[54]

2.2.2 Thermal heating of the surrounding

Illuminated Au NPs can efficiently absorb the photon energy and create heat inside the particle. The generated heat dissipates into the surrounding medium and induces temperature increase in the vicinity of the Au NP surface. The temperature change in the medium can be described by the following heat transfer equation:[24, 58–60]

$$\rho(\vec{r})c(\vec{r})\frac{\partial T(\vec{r}, t)}{\partial t} = \nabla k(\vec{r})\nabla T(\vec{r}, t) + Q(\vec{r}, t), \quad (2.22)$$

where $T(\vec{r}, t)$ is temperature as a function of coordinate \vec{r} and time t , $\rho(\vec{r})$, $c(\vec{r})$ and $k(\vec{r})$ are the mass density, specific heat, and thermal conductivity, respectively. The local heat intensity $Q(\vec{r}, t)$ comes from light dissipation in Au nanoparticles:

$$Q(\vec{r}, t) = \langle \vec{j}(\vec{r}, t) \cdot \vec{E}(\vec{r}, t) \rangle_t = -\frac{1}{2} \Re \left[i\omega \frac{\varepsilon(\vec{r}) - 1}{4\pi} \vec{E}(\vec{r}) \vec{E}^*(\vec{r}) \right], \quad (2.23)$$

where $\vec{j}(\vec{r}, t)$ is the current density, $\vec{E}(\vec{r}, t) = \Re[\vec{E}(\vec{r}) \cdot e^{-i\omega t}]$ is the resulting electric field in the system, and $\varepsilon(\vec{r})$ is the dielectric constant. In this work, the nanoparticle is excited with the external laser field $\vec{E}_0(t) = \Re[\vec{E}_0(t) \cdot e^{-i\omega t}]$. When the laser excites at time $t = 0$, the light intensity is given by:

$$I(t) = I_0 = \begin{cases} c\vec{E}_0^2\sqrt{\varepsilon_0}/8\pi & \text{for } t > 0 \\ 0 & \text{for } t < 0 \end{cases} \quad (2.24)$$

where I_0 is the light intensity inside the medium and ε_0 is the dielectric constant of the medium. For a single spherical Au NP with radius R_{NP} and dielectric constant $\varepsilon_m(\omega)$ in water, the steady state temperature distribution outside the nanoparticle ($t \rightarrow \infty$) can be described by:

$$\Delta T(\vec{r}) = \frac{V_{NP}Q}{4\pi k_0 r} \quad (r > R_{NP}), \quad (2.25)$$

where k_0 is the thermal conductivity of water. Q is the heat dissipation rate, which is a function of the electric field inside Au NP:

$$Q = -\Re \left[i\omega \frac{\varepsilon(\vec{r}) - 1}{8\pi} \vec{E}_0^2 \left| \frac{3\varepsilon_0}{2\varepsilon_0 + \varepsilon_m} \right|^2 \right]. \quad (2.26)$$

The absorption of water in the visible spectrum is negligible in comparison to that of the Au NPs. Hence the absorbing Au NP is the only heating source, and the temperature inside the particle is homogeneous. The maximum temperature is obtained at $r = R_{NP}$. Inserting equation 2.26 into equation 2.25, the maximum temperature increase can be expressed by:

$$\Delta T_{max}(I_0) = \frac{R_{NP}^2}{3k_0} \Re \left[i\omega \frac{1 - \varepsilon(\vec{r})}{8\pi} \left| \frac{3\varepsilon_0}{2\varepsilon_0 + \varepsilon_m} \right|^2 \right] \frac{8\pi \cdot I_0}{c\sqrt{\varepsilon_0}}, \quad (2.27)$$

The maximum temperature increase is dependent on the nanoparticle size $\Delta T_{max} \propto R_{NP}^2$, provided that the medium and the light intensity are constant. The time required to reach a temperature increase $\Delta T(t) = \Delta T_{max}/2$ can be approximately evaluated by:

$$t = \tau_0 = R_{NP}^2/\alpha_0 = R_{NP}^2(c_0\rho_0/k_{t0}). \quad (2.28)$$

where α_0 is the thermal diffusivity of the medium, c_0, ρ_0, k_0 are the specific heat capacity, the mass density and the thermal conductivity of the medium, respectively. For single Au NP in 25°C water, under this temperature $\alpha_0 = 1.39 \times 10^{-7} \text{ m}^2/\text{s}$, the equation 2.28 gives $\tau_0 = 2.88 \text{ ns}$ for $R_{NP} = 20 \text{ nm}$; $\tau_0 = 6.47 \text{ ns}$ for $R_{NP} = 30 \text{ nm}$. This is in a time scale much longer than the thermal equilibration time inside the nanoparticle (several tens of picoseconds).

2.2.3 The Finite-Element Method

Section 2.2.2 gave an analytical method to estimate temperature changes induced by laser illuminated Au NPs in a medium. Alternatively, the temperature increase can be determined numerically with the Finite-Element Method. The Finite-Element Method solves partial differential equations by rendering them into an approximate system of ordinary differential equations, and subsequently integrating them numerically. For steady state calculations, the differential equations could be eliminated. In this work, the COMSOL Multiphysics software is used to carry out the finite-element analysis.[27, 61]

In the finite-element analysis of heat transfer, the steady state model is used to simulate the temperature distribution in the system at equilibrium. In this model, the medium is set to be a sphere with radius $R_m \gg R_{NP}$. The outer boundary of the medium sphere is thermally insulated. Therefore the heat transfer equation can be further simplified into:

$$\delta_{ts}\rho C_p \partial T / \partial t - \nabla \cdot (k \nabla T) = Q, \quad (2.29)$$

where $\rho=19320 \text{ kg/m}^3$ is the mass density of gold, $C_p=0.128 \text{ J/(kg}\cdot\text{K)}$ the heat capacity of gold at constant pressure, $k = 317 \text{ W/(m}\cdot\text{K)}$ the thermal conductivity of gold and Q the laser power density per gold volume (W/m^3) derived from the equation 2.26, 2.12 and 2.13:

$$Q = \frac{\omega}{8\pi} E_0^2 \left| \frac{3\varepsilon_0}{2\varepsilon_0 + \varepsilon_m} \right|^2 \Im \varepsilon_m = C_{abs} P / V_{NP}. \quad (2.30)$$

C_{abs} is the absorption cross-section of a single Au NP, which could be determined by the Mie theory or FDTD simulation. $P(\text{W/m}^2)$ is the laser power density, and $V_{NP}(\text{m}^3)$ is the volume of the Au NP.

Figure 2.6: Temperature distribution of a 532 nm laser illuminated single Au nanosphere with a radius of 20 nm (black), 30 nm (blue) and 40 nm (red) in water, respectively. The laser power intensity is 1 kW/cm^2 . The water temperature is set to be 25°C . The Finite-element analysis with Multiphysics software was used to render the results. The inset plots the temperature distribution in 2D with a color bar indicating the temperature.

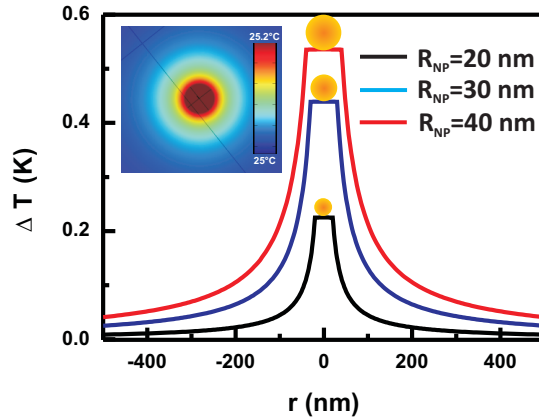


Figure 2.6 shows the calculated size dependent ΔT_{max} induced by the same laser power $P = 1 \text{ kW/cm}^2$ ($\lambda = 532 \text{ nm}$). The inset of the figure is a color plot of the temperature distribution of the $R_{NP}=40 \text{ nm}$ Au NP. The temperature is homogeneous and reaches the maximum value at the nanoparticle. With increasing distance r from the particle surface, the temperature decreases exponentially. For the same illumination power density I_0 , the effective heated volume around the particle increases with increasing particle size. From the equation 2.28, it takes several nanoseconds for the nanoparticle to reach the half of its maximum temperature.

2.3 Optical trapping of gold nanoparticles

Optical trapping and manipulation of matter has been developed during the past 30 years and has been widely applied in various fields including both physics and biology. The Brownian movement of small objects is confined within a certain region by the laser beam, known as the optical trap. Single-beam, double-beam or even multi-beam geometries have been employed so far to achieve the optimized trapping. In this work, single-beam laser trapping, also known as Optical Tweezers, is used. Therefore the following discussion is focused on single-beam trapping experiments. The sizes of the trapped objects vary from the Rayleigh regime ($r \ll \lambda$), such as atoms,[62] to the ray optics regime ($r \gg \lambda$), such as micrometer-size objects and cells.[63–65] Recently, nanoparticles of the Mie regime ($r \simeq \lambda$), especially metallic nanoparticles, have been successfully trapped by light.[16, 66]

A general explanation of optical trapping is the transfer of momentum from the light beam to the object. For particles within ray optics regime, the light beam changes its direction and momentum while passing through a dielectric particle. Consequently, the particle experiences a force along the focused laser beam, and is pulled towards the focus of the beam. This force is known as the gradient force $F_{grad}^{\vec{}}$. Light scattered from the particle gives rise to another force, called scattering force $F_{sct}^{\vec{}}$. The gradient force pulls the particle towards the focus of the light beam, while the scattering force pushes the particle along the light propagation direction, i.e. destabilize the trap. To realize stable trapping, the gradient force needs to overcome the scattering force.

For particles in the Rayleigh regime, $r \ll \lambda$, the photon model is introduced, in which each photon collides with the particle elastically or inelastically. In the elastic case, part or all of the linear momentum of the photon is transferred to the particle, hence changing the travel direction of the particle. In the inelastic collision, the photon is absorbed and all its momentum is transferred to the particle. The particles can be described as point-like dipoles that absorb (inelastic collision) and re-radiate light (elastic collision). The optical forces can be calculated by solving the electromagnetic field through the particle, described by classical electrodynamics.

For metallic nanoparticles in the Mie regime, neither the Rayleigh explanation nor the ray optics explanation can be applied to calculate the optical force correctly. The particle sizes are too big for the Dipole Approximation. Therefore a modified dipole approximation has been applied to describe the trapping in the Mie regime.

To solve the optical trapping force acting on a particle, one needs to know the electromagnetic field distribution of the incident and the scattered field. The

Maxwell stress tensor T_{ij} describes the relationship between the electromagnetic field and the mechanical momentum. T_{ij} gives the momentum density of the electromagnetic field:

$$T_{ij} = \sum_k \varepsilon E_i E_j^* + \mu H_i H_j^* - \frac{1}{2} \delta_{ij} (\varepsilon E_k E_k^* + \mu H_k H_k^*), \quad (2.31)$$

in which $\varepsilon = \varepsilon_0 \varepsilon_m$ is the permittivity and $\mu = \mu_0 \mu_m$ is the magnetic permeability of the medium. * denotes the complex conjugate. Integrating the Maxwell stress tensor over a surface S including the particle of interest and averaging over one optical cycle leads to the expression for the total optical force induced by the incident electromagnetic field onto the particle:

$$\langle F_i \rangle = \frac{1}{2} \Re \left\{ \int_s T_{ij} n_j ds \right\}. \quad (2.32)$$

The Maxwell stress tensor gives a general solution to calculate the optical force of any light on the surface or in the far field of particles with any shape or size. This is based on the information of electromagnetic field in the system. For particles with non-spherical shapes, the calculation becomes difficult. As mentioned in section 2.1.2.2, FDTD gives a numerical solution of the Maxwell's equation, and it is employed in this work to calculate the optical force using the presented equations.

Another way to express the optical force of an electric charge q in an electric field \vec{E} with a velocity \vec{v} and a magnetic field \vec{H} with the Lorentz force is as follows:

$$\vec{F} = q(\vec{E} + \vec{v} \times \mu \vec{H}), \quad (2.33)$$

The total optical force can be given by integrating the optical force density from equation 2.33 over the volume of the particle. For Rayleigh particles, this integration can be simplified into dipole approximation, in which the Taylor expansion of the incident electric and magnetic fields are only kept to the second term. Introducing the dipole moment $\vec{P} = \varepsilon \alpha \vec{E}$, and the polarizability $\alpha = \alpha' + i\alpha''$ the total force can be written as:

$$\langle \vec{F} \rangle = \frac{1}{4} \varepsilon_0 \varepsilon_m \alpha' \nabla (\vec{E}^* \cdot \vec{E}) + \frac{1}{2} \varepsilon_0 \varepsilon_m \alpha'' \Im \left\{ \sum_j E_j^* \nabla E_j \right\}, \quad (2.34)$$

The total force can be decomposed into:

$$\langle \vec{F}_{grad} \rangle = \frac{1}{4} \varepsilon_0 \varepsilon_m \alpha' \nabla (\vec{E}^* \cdot \vec{E}), \quad (2.35)$$

$$\langle \vec{F}_{sct} \rangle = \frac{1}{2} \varepsilon_0 \varepsilon_m \alpha'' \Im \left\{ \sum_j E_j^* \nabla E_j \right\}. \quad (2.36)$$

From equations 2.35 and 2.36, the optical forces are determined by the dielectric properties of the medium, and the polarizability of the particle. For metallic nanoparticles in the Rayleigh regime, the polarizability can be determined from the Clausius-Mossotti equation 2.11. As for Mie regime nanoparticles, the dipole approximation no longer holds, and a modified expression is used to calculate the spherical particle polarizability: [9, 67]

$$\alpha = \frac{4\pi\varepsilon_0 r^3}{3} \frac{1 - \frac{1}{10}(\varepsilon + \varepsilon_m)(|k/n_m|r)^2}{\left(\frac{1}{3} + \frac{\varepsilon_m}{\varepsilon - \varepsilon_m}\right) - \frac{1}{30}(\varepsilon + 10\varepsilon_m)(|k/n_m|r)^2 - i \frac{\varepsilon_m^{2/3} |k/n_m|^3 4\pi r^3}{6\pi} \frac{4\pi r^3}{3}}. \quad (2.37)$$

where n_m is the refractive index of the medium. This formula is an expansion of the first TM mode of Mie's formula. The second term in the denominator describes the energy shift of the retardation effect. The third term represents the radiative loss and is purely imaginary. The fourth term is the higher order correction to the second term and is real.

A comparison between the calculated polarizabilities according to the Clausius-Mossotti equation (CM) and the modified Clausius-Mossotti equation (CMmod) for $r=5$ nm (the Rayleigh regime) and $r=30$ nm (the Mie regime) Au nanospheres is shown in Figure 2.7a and b. As for the particle size in the Rayleigh regime, both equations give similar polarizability in the visible spectrum. While for the particle size in the Mie regime, the two equations give distinct results, especially in the visible range.

The extinction and scattering cross-sections of the corresponding polarizability values were calculated based on equations 2.13 and 2.12, to compare with those calculated based on the Mie theory. Again, the results from the three methods are similar for particle $r=5$ nm (Figure 2.7c). As for larger particle $r=30$ nm, the CMmod gives similar results as the Mie theory, while the CM fails to render the same results. Since Mie theory is an accurate solution to Maxwell's equation for spherical nanoparticles, the CMmod which fits best with the Mie results is a proper equation to calculate the polarizability of spheres in the Mie regime. In this work, the dipole approximation in combination with the CMmod equation was employed to calculate the optical forces of Au nanospheres in the optical trap. In section 4.3, the optical forces calculated with FDTD have been compared with those from the dipole approximation.

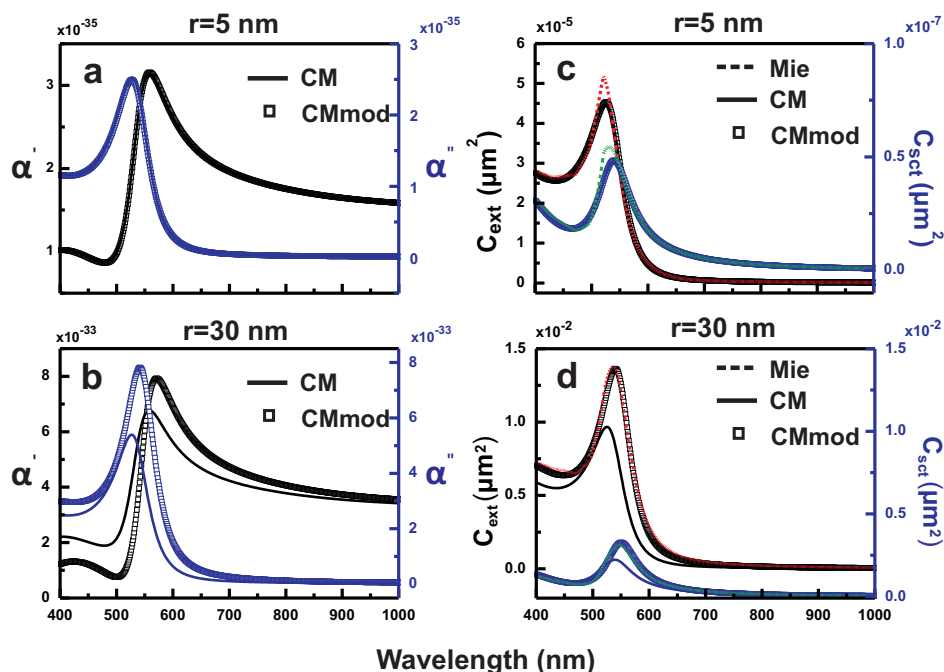


Figure 2.7: Left: the real (black) and imaginary (blue) part of polarizability for (a) $r = 5$ nm, (b) $r = 30$ nm Au nanospheres, calculated according to the Clausius-Mossotti equation (CM, solid line) and the modified Clausius-Mossotti equation (CMmod, squares). Right: the extinction (black) and scattering (blue) cross-sections of (c) $r = 5$ nm, (d) $r = 30$ nm Au nanospheres, calculated according to the Clausius-Mossotti equation (CM, solid line), the modified Clausius-Mossotti equation (CMmod, squares) and Mie theory (Mie, dashed line, red for C_{ext} and green for C_{sct}). In (a) and (c), the CM and CMmod results match so well that the curves overlap in the figures.

2.4 Biological membranes

2.4.1 Lipid bilayers and cellular membranes

Lipids are amphiphilic molecules consisting of a hydrophilic polar head group and a hydrophobic apolar chain. Phospholipids are the most abundant lipids in nature. They are typically glycerolipids with two fatty acid chains and a phosphate-containing head group. Figure 2.8 shows the chemical structure of two phospholipids: DPPC (1,2-palmitoyl-glycerol-3-phosphocholine) and DOPE (1,2-dioleoyl-glycerol-3-phosphoethanolamine). Other non-phospholipids also exist in cellular membranes and play important roles in cell biology. For instance, sphingomyelin (Figure 2.8) is relevant to the formation

of lipid subdomains in biological membranes (namely rafts).[68, 69] Cholesterol (Figure 2.8) is an essential component of mammalian cell membranes, which modulates the fluidity and transition temperature of the membrane. [70]

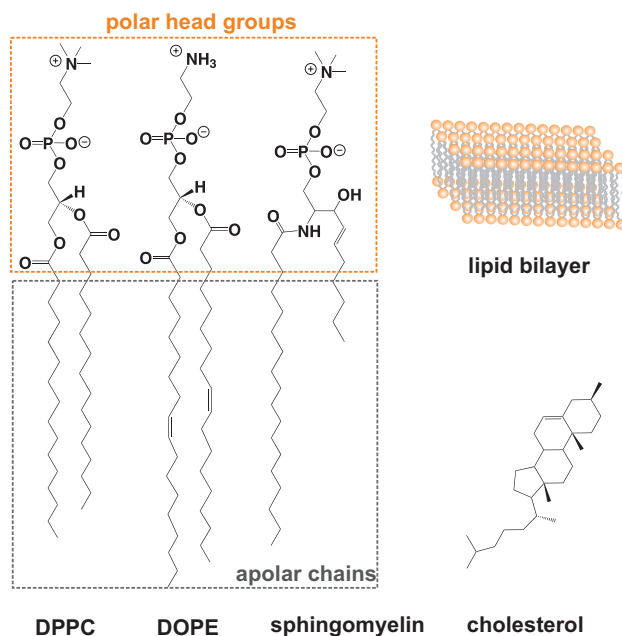


Figure 2.8: The chemical structures of some phospholipids: phosphatidylcholine (DPPC), phosphatidylethanolamine (DOPE), and lipids without phosphate groups: sphingomyelin and cholesterol. Right: a cartoon illustration of lipid bilayer consisting of two opposing monolayers.

In water, lipids spontaneously form aggregates, and bilayer membranes are formed under proper lipid concentrations. Lipid bilayers are two-dimensional sheets, consisting of two layers of lipid molecules, as shown in Figure 2.8: the hydrophilic head groups are exposed to the water and the hydrophobic chains point towards the center of the bilayer, where water is excluded.[71] The formation of lipid bilayers is mainly driven by hydrophobic interactions between the apolar chains of the lipid molecules. The close packing of the hydrophobic chains is favored by van der Waals interactions among the hydrocarbon chains, and the bilayer is further stabilized via hydrogen bonding and electrostatic interactions between the polar head groups and water molecules.[72]

Lipid bilayers are the fundamental units of biological membranes, which seal the cells and provide cells with protection against external harm and plays an important role in cellular signaling and ion trafficking. Cell membranes are not merely mixed lipid bilayers containing various membrane proteins, ion channels,[71] but have more complicated subdomainal structures rich in cholesterol, sphingomyelin,

and membrane proteins.[73–77] These subdomains have been reported to be 10 – 200nm large, and exist in an intermediate state between fluid phase and gel phase (see section 2.4.2).[78, 79] These subdomains have important physiological functions in ion exchange as well as nutrition intake, cellular responses, etc.[80] The regulation of membrane proteins, ion channels and membrane signal molecules is controlled by the cell and varies for different cell types, cell phases, as well as the environmental parameters, such as temperature, chemical environment, pH.

2.4.2 Lipid membrane melting

Lipid membranes display solid-like order at low temperatures. The lipids are arranged in a crystalline order and the apolar chains display all-trans configurations. At high temperatures, the solid-order within the membrane is lost, and lipids are randomly organized, behaving as in a liquid. The temperature induced membrane transition is similar to phase transitions in solid state physics, thus this phase transition is called solid-liquid transition, or membrane melting. The solid-like ordered phase is normally called "gel-phase", and the liquid-like disordered phase is called "fluid phase". This phase transition can be characterized by calorimetry recording the heat capacity c_p of a membrane at different temperatures. For lipid membranes consisted of one lipid type, the transition occurs in a very narrow temperature range.[81] The transition temperature of the pure membrane is determined by the chemical structure of the lipid, mainly the carbon chain length and the degree of saturation in the chain, and external factors, such as the pH, ionic strength and pressure in the solution.[82] Lipids with longer chains have more surface area for van der Waals interactions, which stabilizes the gel phase, and consequently their transition temperature is higher. On the other hand, unsaturated carbon-carbon double bonds do not favor the van der Waals interactions, and lipids with more unsaturated bondings in the side chain have lower transition temperature. For instance, DPPC (Figure 2.8), a saturated lipid with 16 carbons, has a phase transition temperature at 41°C; while DSPC, a saturated lipid with 18 carbons, has a phase transition temperature at 55°C; as for 18 carbons DOPE lipid (Figure 2.8), its transition temperature decreases to –16°C due to the unsaturated double bond in the carbon chain. [83]

In comparison to lipid membranes with one lipid type, biological membranes have mixed lipid compositions and more complex subdomain structures. Their melting temperatures are found to be 10-15 K below body or growth temperature (in the range of 10 – 25°C). The change of heat capacity in biological membranes is not as sharp as that in one composition membranes. Due to their mixed composition, the bending modulus of biological membranes is higher than the one

composition membranes. The incorporation of cholesterol (Figure 2.8) increase the melting temperature of biological membranes, and the bending modulus up to 10 fold.[84, 85] Hence, in comparison to one composition lipid membrane, temperature fluctuations have much less influence on the properties of biological membranes. This stability of the membrane properties under various temperatures is essential to provide the cell with a stable environment.

2.4.3 Lipid diffusion

The thermal motion of lipid molecules in lipid membranes has two forms: lateral motion and rotational motion. The lateral motion is commonly called diffusion, as a result of the stochastic motion of lipid molecules due to thermal collisions with other lipids in the membrane. Therefore lipid diffusion can be related to the Brownian motion as described by Einstein:[86]

$$\langle r^2 \rangle \propto Dt \quad (2.38)$$

The equation above displays a linear relation between the mean square displacement of a lipid $\langle r^2 \rangle$ and the time t . The constant D is the diffusion coefficient as described in the Stokes-Einstein equation:

$$D = \frac{k_B T}{6\pi\eta r} \quad (2.39)$$

in which η is the viscosity of the surrounding fluid, i.e. viscosity of the membrane; r is the radius of the molecule, assuming that the molecule has a spherical shape. The diffusion constant is proportional to the temperature and the molecule size, while inversely related to the viscosity of the membrane. At the membrane phase transition temperature T_m , lipid membranes undergo a phase transition from gel to fluid phase, during which the molecular order of the membrane becomes less compact and thus the viscosity of the membrane decreases. Hence, the lipid diffusion constant in the gel phase is lower than that in the fluid phase membrane. This phenomenon has been widely recognized and experimentally demonstrated.[27, 87–89] The difference of diffusion constants between gel phase and fluid phase is typically 2-3 order of magnitude.

The diffusion in lipid membrane is mostly considered as a two dimensional motion (lateral motion). Figure 2.9 shows all possible types of diffusion in biological membranes: free diffusion in homogeneous membranes; anomalous diffusion in heterogeneous membranes, where different types of lipids coexist; anomalous diffusion in membranes with obstacles, such as membrane proteins; confined diffusion in membrane with closed obstacle boundaries.[79, 87] Free diffusion can

be described by a linear relation between the mean square displacement $\langle r^2 \rangle$ and diffusion time t as:

$$\langle r^2 \rangle = 4Dt \quad (2.40)$$

Anomalous diffusion exists in biological membranes, where membrane proteins and subdomains form obstacles or heterogeneous membrane components that hinder the free motion of lipids in the membrane. Anomalous diffusion is commonly described as:

$$\langle r^2 \rangle = 4Dt^\alpha, \alpha < 1 \quad (2.41)$$

where α is a parameter describing the freedom of anomalous motion. A larger α represents a higher degree of freedom in diffusion.

Confined diffusion is also called corralled diffusion. It describes the lipid diffusion within an isolated region surrounded by connected obstacles. This exists in membranes with high concentration of membrane proteins or within a lipid subdomain. If the isolated region is a circle with radius r_c , the confined motion can be described as:

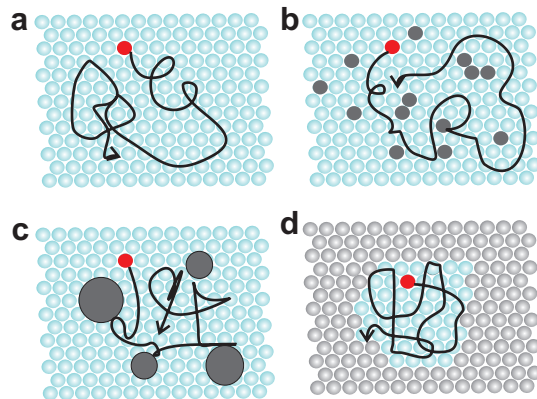
$$\langle r^2 \rangle = \langle r_c^2 \rangle \left[1 - \exp\left(-\frac{4Dt}{\langle r_c^2 \rangle}\right) \right] \quad (2.42)$$

Directed motion happens when directed transportation takes place in the membrane, or an experimental artifact due to sample movement. If the velocity of the steady motion is v , directed motion can be expressed as:

$$\langle r^2 \rangle = 4Dt + (vt)^2 \quad (2.43)$$

The lipid diffusion can be experimentally observed by fluorescence techniques such as fluorescence recovery after photobleaching (FRAP),[90] fluorescence correlation spectroscopy (FCS),[91] by labeling the lipid molecules with fluorescent

Figure 2.9: Schematic drawing of four diffusion modes: a) free diffusion in a homogeneous membrane; b) anomalous diffusion in a heterogeneous membrane; c) anomalous diffusion in a membrane with obstacles; d) confined diffusion within a local domain. Grey shades indicate regions where diffusion is not possible.



markers and observing the ensemble fluctuations in the membrane. The diffusion of individual lipids can be measured by single particle tracking (SPT),[92] in which fluorescence or gold markers are used to label lipids, and the diffusion path is tracked. Other methods such as nuclear magnetic resonance (NMR) in field gradient was also applied to obtain diffusion constants,[93, 94] and neutron scattering is used to observe the diffusion over very short distance.[95]

3 Experimental setups and sample preparation

In this chapter, the experimental setups and the sample preparation details are described. Section 3.1 first describes the laser equipped dark field microscope (DFM) for nanoparticle trapping and plasmonic heating experiments. After this, the setups for characterizing nanoparticles, i.e. UV-VIS-NIR spectrometer, dynamic light scattering setup, electron microscopes and FTIR microscope, are introduced. The synthesis and oxidation of CTAB-stabilized Au nanorods are described in section 3.2.1. The experimental details to synthesize and grow CTAB-stabilized gold nanospheres in an optical trap are described in section 3.2.2. Section 3.2.3 describes the experimental strategy to immobilize the PEG-modified gold nanospheres on living Jurkat cell membranes by covalently binding the nanospheres to the thiolated lipid molecules before cell-membrane fusogenesis.

3.1 Experimental Setups

3.1.1 Laser-equipped dark field microscope for trapping and heating

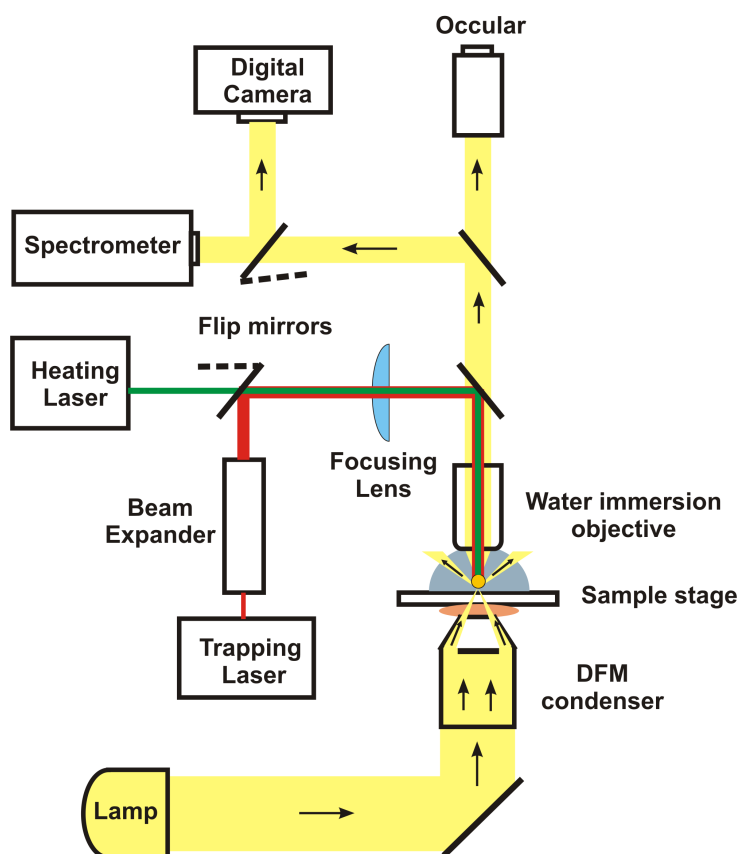


Figure 3.1: Illustration of laser equipped dark-field microscope for trapping and heating Au NPs

An up-righted dark field microscope (DFM) is the main setup of this work. An illustration of this setup is shown in Figure 3.1. The DFM configuration is up-righted (Axio Scope A1, Carl Zeiss), with a continuous light source (Halogen lamp, 100W, Carl Zeiss), a Carl Zeiss oil immersion dark field condenser (NA=1.2-1.4), a nanometer precision sample positioning stage (PI), a temperature controlling sample holder (Olympus, POC-R2) and a water immersion objective NA=1.0 (Achromplan 100 \times , Carl Zeiss). A refractive index matching immersion oil ($n = 1.518$) was applied between the condenser and the glass sample substrate (0.19 – 0.23 mm thickness) for the observation of the samples in

water-based solutions. For imaging and spectroscopy, the microscope is equipped with a digital camera (Canon EOS500D), a spectrometer with SP2556 monochromator and PI eXcelon CCD chip (Spec-10). A half mirror (50/50) was used in between the digital camera and the spectrometer to enable simultaneous imaging and spectroscopy. If only one observation method was required, a flip mirror was used additionally.

A solid state infrared laser (Cobalt Rumba CW) operating at 1064 nm, with maximum output power of 2.1 W, was used as the trapping laser for the Au NPs in the trapping experiments. The laser beam was expanded by a beam expander (Edmund Optics 1064 nm) and then coupled into the DFM through a focusing lens (biconvex, $f=1000$ mm, Thorlab) to compensate the chromatic aberration in the objective. The typical laser power density used for trapping Au nanorods or nanospheres was 9-20 MW/cm². For plasmonic heating experiments, a Nd:YAG laser (Millenia Vs 532 nm, Spectra-Physics) operating at 532 nm under continuous wave mode was coupled into the DFM through a 100 \times water immersion objective. The laser beam was converged by a focusing lens (biconvex, $f=250$ mm, Thorlab) to achieve a large laser spot (ca. 5 μ m full width half maximum) at the focus of the objective.

3.1.2 UV-Vis-NIR spectroscopy

A UV-Vis-NIR spectrophotometer (Cary 5000, Varian) was used to characterize the extinction spectra of Au nanospheres and Au nanorods at room temperature. Quartz cuvettes with a path length of 10 mm or 4 mm were filled with nanoparticle solutions and inserted into the sample holder for measurements. Temperature related extinction spectra were performed with an UV-Vis spectrophotometer (Cary 50, Varian) equipped with a self-made sample holder heated by a temperature controller (single cell peltier accessory).

3.1.3 Dynamic light scattering and ζ -potential

To determine the hydrodynamic size distribution of the small vesicles and the nanoparticles, dynamic light scattering experiments were performed with a Zetasizer Nano-ZS (Malvern Instruments) using a 4 mW He-Ne laser operating at 633 nm and a detection angle of 173°. The ζ -potential of nanoparticles was also measured with the same setup. For this, the nanoparticle solution was injected into a capillary cell with built in electrodes, and the sample was inserted into the machine under set temperature. The obtained zeta-potential values were used to determine the surface character of the nanoparticles.

3.1.4 Electron microscopy

Transmission electron microscopy (TEM) was performed on a JEOL JEM 1011 microscope operating at 100 kV. To prepare the sample for TEM observation, a droplet of washed and diluted Au NP solution was added on a carbon coated copper grid and left dry in air.

Scanning electron microscopy (SEM) was performed on a Carl Zeiss ULTRA PLUS field emission scanning electron microscope (FE-SEM) operating at 1 kV with 2.1 mm working distance. Prior to SEM measurements, glass substrates deposited with Au NPs were coated with Au/Palladium using a Leica EM SCD005 Cool Sputter Coater at 15 mA for 20 sec.

3.1.5 FTIR microscopy

FTIR spectra were collected with an Hybrion 2000 microscope equipped with an MCT (Mercury Cadmium Telluride) detector in reflection mode by averaging 200 scans with 1.93 cm^{-1} resolution. The samples were prepared by drop casting $10\text{ }\mu\text{L}$ of a concentrated sample onto a gold-coated glass substrate.

3.2 Sample preparation

3.2.1 Synthesis and oxidation of CTAB stablized gold nanorods

3.2.1.1 Synthesis of CTAB stabilized gold nanorods

Au nanorods were prepared using the Ag ion-assisted seed-mediated method.[96, 97] A Au seed solution was prepared by borohydride reduction of 5 mL 0.25 mM HAuCl_4 in an aqueous CTAB solution 0.1 M. The average particle size measured by TEM was $2.8 \pm 0.7\text{ nm}$. $3.75\text{ }\mu\text{L}$ of the obtained seed solution was added to 10 mL growth solution containing 0.1 M CTAB, 0.5mM HAuCl_4 , 0.8 mM ascorbic acid, 0.12 mM silver nitrate and 18.6 mM HCl. The as-prepared Au nanorods were washed twice by centrifugation and the nanorods were redispersed into the same volume of 0.1 M CTAB solution, in order to remove the chemical residues from synthesis.

3.2.1.2 Oxidation of CTAB stabilized gold nanorods

The size and aspect ratio of Au nanorods can be tailored by oxidation. Here a mild oxidation approach based on hydrogen peroxide oxidation at a certain pH and temperature was applied.[98, 99] The oxidation in bulk solution was performed

in a quartz cuvette and the corresponding extinction spectra were monitored by UV-Vis-NIR spectroscopy every two minutes. First, the pH of the Au nanorod solution obtained from previous synthesis process was tuned to 3 by adding 1 M HCl. The oxidation of Au nanorods was then started by adding H₂O₂ (35 wt%) into the Au nanorod solution. The concentration of H₂O₂ in the nanorod solution was fixed at 147, 49, 9.8, 2.94, 0.49, 0.29 and 0.1 mM, when the experiment was performed at 35, 45, 55, 65, 75, 85 and 95°C, respectively (see Figure 4.2).

The oxidation of Au nanorods on a piranha-cleaned glass slide was performed in a temperature-controlled perfusion chamber. 0.5 mL of the as-synthesized nanorods were added into the perfusion chamber, and left for 30 min at 30°C to allow nanorods to deposit on the substrate. Here two approaches were used to remove the excess nanorods. In the first approach, the excess solution was removed directly and the substrate was dried out in air. While in the other approach, the substrate was washed for several rounds by diluting the excess solution with a 0.1 M CTAB solution and carefully removed the diluted solution without drying out the substrate. Thereafter, 4 mL of the 0.1 M CTAB solution, 0.08 mL of the 1 M HCl solution, and 0.05 mL H₂O₂ (35 wt%) were added into the chamber which was kept at 30°C. Scattering spectra from the nanorods on the substrate were monitored under the DFM and recorded as a function of time (Figure 4.6).

The oxidation of Au nanorods in an optical trap was performed in a temperature-controlled perfusion chamber. 1.25 μ L of the washed Au nanorod solution was diluted into 20 mL of the 0.1 M CTAB solution. The pH of the solution was tuned to 3 by adding 0.4 mL of the 1 M HCl solution. The mixture was purified by 2 cycles of filtration with 0.2 μ m pores-filter. After purification, 4 mL of the final solution was injected into the perfusion chamber on the stage of the laser-equipped DFM. The temperature of the chamber was kept at 30 °C to prevent the crystallization of the CTAB during the measurement. 20 μ L of the H₂O₂ solution was injected and mixed in the chamber, followed by the experiment for the oxidation of Au nanorods in the optical trap. Scattering spectra from the nanorod in the trap were monitored and recorded as a function of time (see Figure 4.3).

3.2.2 Synthesis and growth of CTAB stabilized gold nanospheres

3.2.2.1 Synthesis of CTAB-stabilized gold nanospheres

The synthesis of CTAB (cetyltrimethylammonium bromide, Aldrich) stabilized Au nanospheres was based on a seeded-growth process consisting of the preparation of CTAB-stabilized Au seeds and the overgrowth of Au seeds to Au

nanospheres.[100] In the first part, citrate reduction of Au (III) was achieved by adding 25 mL of a warm sodium citrate solution (1wt%) to 500 mL of a boiling 0.5 mM HAuCl₄ aqueous solution under vigorous stirring, followed by 15 min of continuous boiling.[3] The obtained citrate-stabilized Au seeds (12 nm diameter, named Au@citrate) were cooled down and the citrate molecules were replaced by CTAB through the addition of the same volume of 0.03 M CTAB solution into the Au@citrate solution. The CTAB concentration in the final obtained CTAB-stabilized Au seed solution was 0.015 M and the Au concentration 4.5×10^{-4} M. In the second part, CTAB stabilized Au seeds were over-grown in Au (III) solution in the presence of ascorbic acid. In order to estimate the relative concentration of Au seeds and Au (III) to obtain a desired nanoparticle size, the following equation was used:[101]

$$r = r_{seed} \left(\frac{[M_{added}] + [M_{seed}]}{[M_{seed}]} \right)^{1/3} \quad (3.1)$$

where r is the expected radius of the grown particles; r_{seed} is the radius of the seeds and $[M_{seed}]$ is the final metal concentration in the seeds, $[M_{added}]$ is the concentration of added ions.

From equation 3.1, the 12 nm Au seeds were grown up to 40 nm (theoretical size) as following: 2.5 mL of 0.1 M ascorbic acid solution was added to 500 mL of the growth solution consisting of 0.12 mM HAuCl₄ and 0.015 M CTAB at 35 °C. The mixture was thoroughly mixed and followed by the addition of 2.57 mL Au seed solution ($[Au]=4.5 \times 10^{-4}$ M), vigorously mixed, and kept at 35 °C for 2 hours.

3.2.2.2 Growth of CTAB stablized gold nanospheres

The growth of the as-synthesized 37 nm Au nanospheres was performed both in bulk and in an optical trap. The as-synthesized 37 nm Au nanospheres were used as seeds, and Au(III) ions were added under controlled pH and temperature conditions to allow for the controlled growth of Au nanospheres. The growth of Au nanospheres in bulk solution was performed in a quartz cuvette with a path length of 2 mm and the extinction spectra were collected with a UV-IR spectrophotometer with a temperature-controlled sample holder. A growth solution was prepared by mixing 10 mL of a 0.1 M CTAB solution, 0.125 mL of a 0.01 M HAuCl₄, 0.2 mL of a 1 M HCl, and 0.02 mL of a 0.1 M ascorbic acid solution. For growth, 0.1 mL of the starting Au nanosphere solution was mixed with 0.9 mL of the growth solution in a quartz cuvette. The solution temperature during the measurements was set to 95 °C. Extinction spectra were monitored and recorded every two minutes (see Figure 4.9a).

The growth of single Au nanospheres in the optical trap was performed in a temperature-controlled perfusion chamber on the laser-equipped DFM setup. The growth solution was the same as that in the bulk growth experiments: 10 mL of 0.1 M CTAB solution, 0.125 mL of 0.01 M HAuCl₄, 0.2 mL of 1 M HCl, and 0.02 mL of 0.1 M ascorbic acid solution. Prior to usage, the growth solution was purified by 2 cycles of filtration with 0.2 μm pore-filters. The as-synthesized Au nanosphere solution was washed twice and diluted 10⁴ times in the CTAB solution. The diluted solution was also purified by 2 cycles using the 0.2 μm pores-filters. Thereafter, 4 mL of the growth solution was added into the perfusion chamber. The temperature of the chamber was kept at 27 °C. 20 μL of the diluted Au nanosphere solution was added and mixed with the growth solution, immediately followed by the start of the experiment for the growth on Au nanospheres in the optical trap. Scattering spectra from the nanoparticles in the trap were monitored and recorded as a function of time (see Figure 4.9b). The growth was stopped by bringing the nanoparticles to the substrate and removing the laser trap. The as-grown nanoparticle was attached to the substrate due to electrostatic force. Carefully removing the growth solution, the substrate was dried and examined by SEM to characterize the size and shape of grown particles.

3.2.3 Immobilization of gold nanoparticles on living cell membranes via covalent binding

3.2.3.1 Synthesis of CTAB-stabilized gold nanoparticles

CTAB-stabilized 70 nm (theoretical size) Au nanospheres were prepared as described before in section 3.2.2. Briefly, 2.76 mL Au seed solution was added (4.5×10^{-4} M) into 500 mL growth solution with 0.25 mM HAuCl₄, 0.5 mM ascorbic acid and 0.015 M CTAB at 35 °C.

3.2.3.2 PEGylation of CTAB-stabilized gold nanoparticles

Prior to PEG grafting, the excess surfactant was removed and the as-synthesized Au@CTAB solution was concentrated. Typically, 120 mL of the Au@CTAB spheres ([Au]= 0.25 mM, [CTAB]=0.015M) were centrifuged twice (30 min, 1157g) and redispersed with water up to a final volume of 28 mL to obtain [CTAB]~0.5 mM and [Au]~1.1 mM.

Thereafter a mixture of CH₃O-PEG-SH (mPEG-SH, Mw 5000 Da) and HS-PEG-NH₂×HCl (HS-PEG-NH₂ Mw 5000 Da) was added so as to provide the Au NPs with ca. 150 PEG molecules/Au nm², ensuring adequate surface grafting and particle stability in PBS. This is a clear excess, as according to the literature ca. 2.85 mPEG-SH molecules can be accommodated per Au nm². [102] Typically,

HS-PEG-NH₂ and mPEG-SH were initially mixed and diluted with 500 μ L of water. The mixture was then sonicated for 15 min and subsequently added dropwise under vigorous stirring to 4.5 mL of the washed Au colloid so as to obtain the following final conditions: [Au]=1 mM, [HS-PEG-NH₂]=0.25 mM and [mPEG-SH]=2.3 mM (1:9 ratio, respectively). Those grafting conditions provide ca. 1 order of magnitude less reactive (amino) vs. non-reactive (methoxy) terminal groups. The mixture was allowed to react overnight under moderate stirring. Thereafter the PEG-capped particles were diluted with water in a 1:10 volume ratio and centrifuged (30 min, 1157g) in 10 mL tubes. From each tube the supernatant was discarded and the pellet was redispersed in 10 mL of PBS buffer (pH 7.6) under sonication. The centrifugation was repeated and each pellet was finally redispersed in 5 mL of the PBS buffer (pH 7.6). The as-synthesized PEG modified particles are referred to as Au@mPEG-SH/HS-PEG-NH₂.

3.2.3.3 Maleimide derivatization

The amino groups from the Au@mPEG-SH/HS-PEG-NH₂ surface were derivatized in order to render the nanoparticles with a maleimide reactive group for the subsequent lipid labeling. For the maleimide derivatization, typically 2 mL of the as-prepared Au@mPEG-SH/HS-PEG-NH₂ nanoparticles ([Au]=0.4 mM), 2 mL of a fresh solution of the maleimide crosslinker 4-(N-Maleimidomethyl)cyclohexane-1-carboxylic acid 3-sulfo-N-hydroxysuccinimide ester sodium salt (sulfo-SMCC), with [sulfo-SMCC]=40 μ M in PBS, pH 7.6, were added dropwise and allowed to react for 15 min under moderate stirring. The amount of sulfo-SMCC added was calculated to yield a ratio [HS-PEG-NH₂]:[sulfo-SMCC]=1:2 (assuming that all the added HS-PEG-NH₂ grafts on the Au surface). This ensures the presence of sufficient crosslinker to react with the terminal amino groups. Thereafter the sample was diluted in a 1:5 volume ratio with PBS buffer (pH 7.6), centrifuged once (30 min, 1157g) and redispersed in 4 mL of PBS (pH 6.9) under sonication. Hereafter, the as-functionalized particles are referred to as Au@mal.

3.2.3.4 Preparation of fusogenic vesicles and giant unilamellar vesicles

Small (multi-/unilamellar) liposomes based on SOPC (1-octadecanoyl-2-(9Z-octadecenoyl)-sn-glycero-3-phosphocholine) and DOPE (1,2-di-(9Z-octadecenoyl)-sn-glycero-3-phosphoethanolamine) and containing the thiolated lipid PTE-SH (1,2-Dipalmitoyl-sn-Glycero-3-Phosphothioethanol (Sodium Salt)) were prepared using dry-rehydration and bath sonication. Typically the total lipid concentration was adjusted to 1 mg/mL. The lipid ratios were fixed to SOPC:DOPE=3:1, since this mixture is known to be fusogenic with the plasma membrane of cells.[103, 104]

The ratio PTE-SH:total number of lipids was adjusted to 1:200. The lipid mixture was dissolved in chloroform, gently dried with a nitrogen flow and allowed to dry under vacuum overnight in order to obtain a completely dehydrated lipid film. Thereafter, 1 mL of PBS buffer (pH 6.9) was quickly added under bath sonication. The sample was further sonicated for additional 5 min. The obtained liposomes have an average hydrodynamic diameter (measured from zeta-sizer) of ca. 620 nm, with a second population of ca. 120 nm.

Giant (3-5 μm) unilamellar vesicles (GUVs) based on DPPC and with the same concentration of PTE-SH as above were obtained by electroformation in PBS (pH 6.9).[105] In brief, 60 μL of a chloroform solution containing 0.5 mg/mL SOPC and 2.5×10^{-3} mg/mL PTE-SH were added dropwise to the platinum wire of the vesicle growing chamber preheated to ca. 50°C, followed by the addition of 4.5 mL PBS buffer. Alternating current fields (sinusoid) of preprogrammed amplitudes and frequencies were generated by a function generator and applied to the chamber to produce the GUVs. An adapted protocol of the fields to growth GUVs in PBS buffer is shown in Table 3.1. 0.5 mL of 260 mM glucose solution was added into 0.5 mL of the as prepared GUV suspension to precipitate the GUVs for further experiments.

Field strength (V/m)	Frequency (Hz)	Time (min)
50 \rightarrow 1300	500	30
1300	500	90
1300	500 \rightarrow 50	30

Table 3.1: Electroformation protocol for growing GUVs in the PBS solution

3.2.3.5 The Jurkat cell culture

Jurkat cells were chosen in this work as an example cell line to investigate the lipid-Au NP labeling. Jurkat cells are an immortalized cell line of human T cell *leukemia*. The Jurkat cell line was established from the JM line of the peripheral blood cells of children with acute *lymphoblastic leukemia* by Schneider et al.[106] Jurkat cells are model cells for studying acute T cell *leukemia*,[107] T cell signaling,[108] and are known to produce large amount of *interleukin 2*,[109] a type of cytokine signaling molecule in the immune system.

Jurkat cell Clone E6-1 (ATCC, TIB-152), a clone of the the Jurkat-FHCRC cell line,[109] was purchased and maintained in the S1 cell culture laboratory. The cell culture was kept in a cell incubator under 37°C and 5% CO₂ environment. The Jurkat cell growth medium contained a basis medium RPMI-1640 (Biochrom AG, VLE-RPMI-1640) with very low endotoxin and 2.0 g/L NaHCO₃. To prepare

the growth medium, 5 mL of HEPES buffer (Biochrom AG, 1M), 50 mL of Fetal Bovine Serum (Biochrom AG, 10%), 5mL of L-Glutamine (Sigma-Aldrich, 20mM) and 5 mL of D-(+)-Glucose (Sigma-Aldrich, 45%) were added into 430 mL basis medium and homogenized.

The maintenance of jurkat cells follows the standard procedure of non-adhesive cell cultures. Typically, the cell culture was incubated for 3-4 days in a cell incubator, and the cell culture concentration was checked with a bright field optical microscopy using a 20 \times objective. 5 mL of the cell culture was centrifuged at 1 rpm (revolutions per minute) for 2 minutes and the supernatant was discarded, leaving only the cell pellet. 5 mL of the growth medium was added to redisperse the pellet and 0.5 mL of the redispersant was added into a cell culture bottle containing 5 mL growth medium. The bottle was kept in the cell incubator for cell proliferation. Prior to usage, the cell culture was centrifuged at 1000 rpm for 2 min and the cell pellet was redispersed in PBS buffer (50mM, pH 6.9) for further processing.

3.2.3.6 Immobilization of maleimide-derivatized gold nanoparticles onto GUV and cell membranes

Au@mal binding to either small or giant vesicles containing sulfhydryl groups (PTE-SH) was carried out via addition of 0.2 mL of Au@mal nanoparticles (containing [Au]=0.2 mM and [maleimide] ca. 5 μ M, assuming that all the added HS-PEG-NH₂ was grafted on the Au surface and that all the -NH₂ reacted with the sulfo-SMCC crosslinker) to 1 mL of the thiolated liposomes (containing [PTE-SH]=5 μ M) in PBS (pH 6.9). The final [maleimide]:[PTE-SH] ratio was fixed to 1:5 in order to ensure optimal PTE-SH/Au@mal binding and that no excess of Au@mal nanoparticles was present in the vesicle solution, since they could potentially bind to other thiolated entities at the cellular membrane during incubation with the cells. The reaction was allowed to proceed for 30 min under gentle orbital shaking. Subsequently 1 mL of Jurkat cells in RPMI medium was centrifuged (1 min, 100g). The pellet was directly and gently redispersed in 1 mL of the Au@mal-labeled fusogenic liposomes (PBS, pH 6.9). The Liposome-cell membrane fusion was allowed to proceed for 30 min. The non-fused Au-labeled liposomes were separated from the cells by centrifugation (twice, 1 min, 100g) and redispersion in 1 mL of PBS (pH 6.9).

3.2.3.7 I₂/KI oxidation

I₂/KI mixture was used to oxidize Au@mal nanoparticles to exam whether the nanoparticles were on the cell surface. A stock solution consisting of a mixture of I₂ and KI in water was prepared (the final concentration was fixed to 10 mM and

60 mM, respectively). The oxidation of the Au@mal nanoparticles in solution (Figure 5.5) was carried out by addition of 35 μL of the I_2/KI stock solution to 1 mL of Au@mal nanoparticles ($[\text{Au}]=0.081$ mM). The oxidation was followed by UV-Vis-NIR spectroscopy in a 1 cm path length quartz cuvette.

The oxidation of Au@mal nanoparticles labeled to the cell membrane as a result of fusogenesis was performed using the I_2/KI mixture. The experiment consisted of the addition of 3.5 μL of the I_2/KI stock solution to 100 μL of the cells (previously incubated with the Au@mal-labeled liposomes and washed twice) deposited on a piranha-cleaned glass slide.

3.2.3.8 Cytochalasin D treatment of cells

Cytochalasin D (from *Zygosporium mansonii* in DMSO, Sigma) was added into Jurkat cell medium suspended with Au@mal-labeled cells to achieve a cytochalasin D concentration of 1 μM . After 30 min incubation, cells were separated by centrifugation (twice, 1 min, 100g) and redispersion in the same volume of PBS (pH 6.9).

4 Enhancing single gold nanoparticle surface-chemistry by plasmonic overheating in an optical trap

Optical trapping is a well-established technique that has been widely applied to single-molecule force and optical spectroscopy; non-invasive manipulation, and monitoring chemical reactions.[65, 110–114] Here optical trapping is applied to manipulate Au NPs, which have localized electromagnetic field enhancement close to their surface due to their localized surface plasmon resonances.[115] These optical and field-enhancement properties allow for the enhancement of fluorescence, Raman scattering, charge and energy transfer, as well as the manipulation of the local temperature.[116–119] Among these plasmonic effects, the elevation of local temperature in the optical trap has been of great interest due to its application in drug delivery and photothermal therapy.[120]

In this chapter, the plasmonic heating effect on a single Au NP in an optical trap has induced both accelerated and modified chemical reactions on the surface of the particle. Depending on the optical trapping power, Au nanorods can exhibit red-shifts of their plasmon resonance (i.e. increasing aspect ratio) under oxidative conditions. In contrast, in bulk exclusively blue shifts (decreasing aspect ratio) are observed. Supported by calculations, this finding can be explained by local temperatures in the trap exceeding the boiling point of the solvent which can not be achieved in bulk. The critical role of particle temperature is further illustrated by modified kinetics of single Au nanosphere growth in the optical trap.

4.1 Single gold nanorod oxidation in an optical trap

CTAB-stabilized Au nanorods were used for oxidation experiments. The experimental details to synthesize Au nanorods are described in 3.2.1. Figure 4.1 displays the extinction spectrum and TEM image of the synthesized nanorods. The longitudinal plasmon resonance wavelength of the nanorods was at 716 nm. The shape and dimension of the nanorods measured with TEM were $79.5 \pm 6.9 \times 30.2 \pm 2.7$ nm, with an aspect ratio of 2.7 ± 0.3 .

Mild oxidation conditions based on hydrogen peroxide in CTAB solutions were employed for Au nanorod oxidation (see details in 3.2.1). The oxidant concentration and the reaction temperature are the two variables that influence the oxidation speed and the reaction results. Prior to single particle experiments, the oxidation condition, especially the influence of H_2O_2 concentration and temperature, need to be determined. Therefore, we first discuss the nanorod oxidation in bulk solutions under various H_2O_2 concentration and temperature. Thereafter, results of the single particle oxidation experiments in the trap are described and discussed, in comparison to the bulk oxidation results.

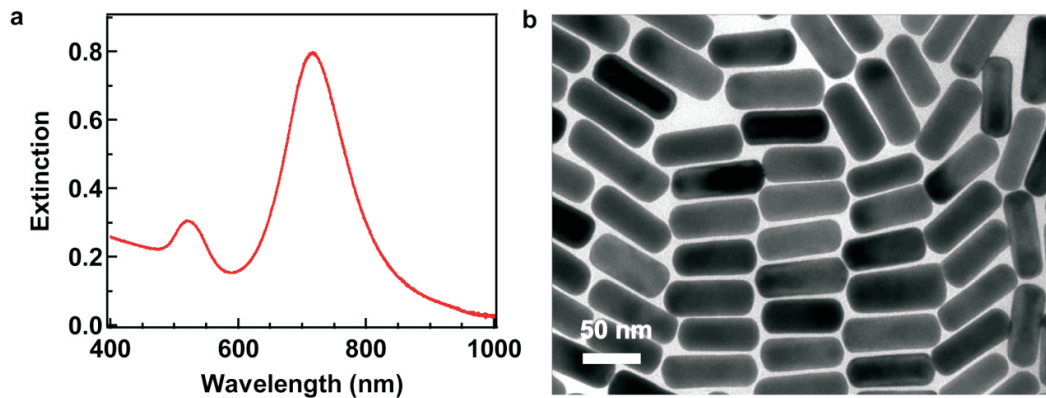


Figure 4.1: (a) Extinction spectrum of as-synthesized Au nanorods. The longitudinal plasmon resonance wavelength of the nanorods is 716 nm. (b) Representative TEM image of the Au nanorods. The Au nanorod dimensions are $79.5 \pm 6.9 \times 30.2 \pm 2.7$ nm, with an aspect ratio of 2.7 ± 0.3 .

4.1.1 Oxidation conditions: oxidant concentration and temperature effect

Various oxidant H_2O_2 concentrations were used to oxidize CTAB-stabilized Au nanorod solutions at different temperatures. To characterize the oxidation process, the extinction spectra of the bulk solution were recorded over time. Figure 4.2 shows the time dependent extinction spectra of Au nanorods during the oxidation in bulk solutions under various temperatures. Similar rates at different temperatures can be achieved by adjusting the oxidant concentrations, i.e. lower concentration at higher temperatures. This also shows that higher temperature accelerates the reaction in bulk solutions.

In Figure 4.2, we have observed exclusive blue-shift of the nanorod longitudinal resonance wavelength, i.e. the aspect ratio decreases, during oxidation. Nanorod reshaping, another process that may coexist with oxidation, occurs at high temperatures.[121] In the temperature range of this experiment (below 100 °C) nanoparticles reshape slowly, and the reshaping time scale (hours or days) is much larger than the measurement time in this experiment (tens of minutes). Reshaping of nanorods often starts from the tips, due to their large surface tension, which decreases the aspect ratio of nanorods towards 1. Therefore, reshaping induces blue-shift in spectra and enhancement of the transversal resonance as a result of enhanced electron oscillations along the short axis of the rod. However, in Figure 4.2, with the shift of the longitudinal resonance, the intensity of the transversal resonance decreased with time, which indicated that the observed phenomena were due to oxidation rather than particle reshaping.

The relationship between oxidation rate and the reaction temperature (T) can be fitted exponentially. From the Arrhenius equation (4.1),[122] the reaction coefficient k is a function of temperature and activation energy E_a .

$$k = A \exp\left(-\frac{E_a}{k_B T}\right) \quad (4.1)$$

Using the fact that the reaction rate is of the first order with respect to the H_2O_2 concentration, the oxidation reaction coefficient k can be expressed in terms of the resonance wavelength change per minute as a function of $1/T$, as shown in Figure 4.2h.[123] The activation energy can be estimated according to equation 4.1 to be $1.1 \cdot 10^2$ kJ/mol.

The results of H_2O_2 oxidation of Au nanorods in the bulk solution showed that, during the reaction the nanorod longitudinal resonance blue-shifted. Oxidation is the main cause of blue-shifted resonance. For constant H_2O_2 concentrations, the oxidation rate showed exponential increase with elevated temperature, matching the Arrhenius equation in kinetics.

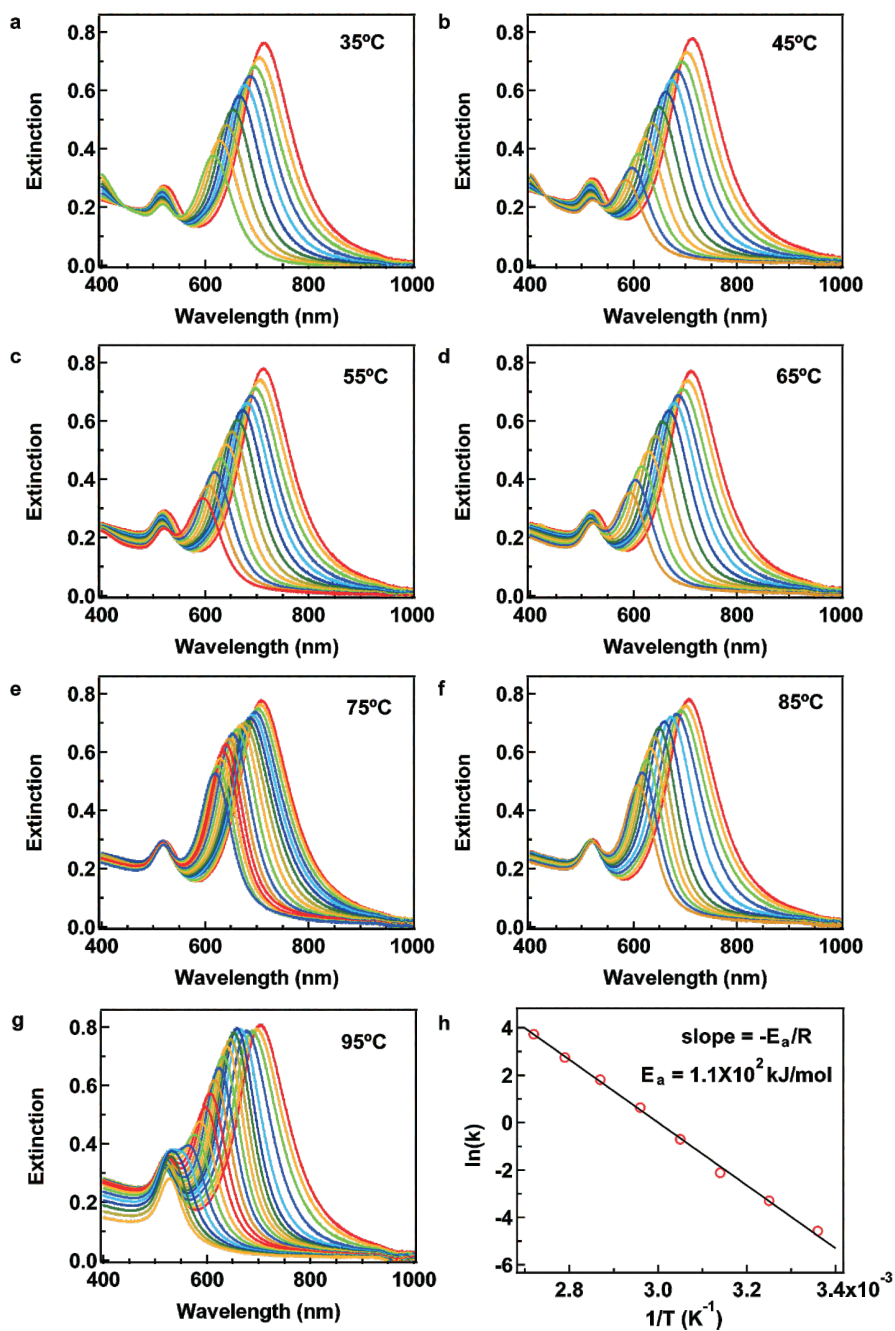


Figure 4.2: (a)-(h) Time dependent extinction spectra of Au nanorods oxidized in bulk solutions at 35 (a), 45 (b), 55 (c), 65 (d), 75 (e), 85 (f), and 95 (g) degrees centigrade, respectively. H_2O_2 concentrations in the bulk solutions were controlled at 147 (a), 49 (b), 9.8 (c), 2.94 (d), 0.49 (e), 0.29 (f), and 0.1 (g) mM, respectively. The spectra were recorded every two minutes. (h) Oxidation reaction rate in terms of the resonance wavelength change per minute as a function of $1/T$. The activation energy E_a is estimated to be $1.1 \cdot 10^2 \text{ kJ/mol}$.

4.1.2 Single gold nanorod oxidation in an optical trap

In the single particle oxidation experiments, the oxidation conditions, such as H_2O_2 concentration, environment temperature, pH and nanorod concentration in solution (see section 3.2.1) were kept constant. The scattering spectra of trapped nanorods under oxidation conditions were recorded over time, and the diffusion trajectories were monitored simultaneously by using a digital camera. Figure 4.3 displays representative scattering spectra of three distinct oxidation behaviors of single Au nanorods in the optical trap: the longitudinal plasmon resonance of the rod either blue shifted or red shifted over time or did not display a shift at all. All three cases were accompanied by a reduction in scattering intensity. This is in clear contrast to the corresponding bulk reaction in which exclusively blue shifts are observed over a wide range of oxidant concentrations and temperatures (Figure 4.2). This shows that in the trap, in contrast to bulk, the oxidation can be altered such that the aspect ratio increases and the plasmon resonance red shifts or the aspect ratio stays constant and the resonance does not shift. It is also noted that the single nanorods shifted on a time scale of minutes while the bulk reaction took tens of minute to complete at room temperature even when the oxidant concentration is ten times higher.

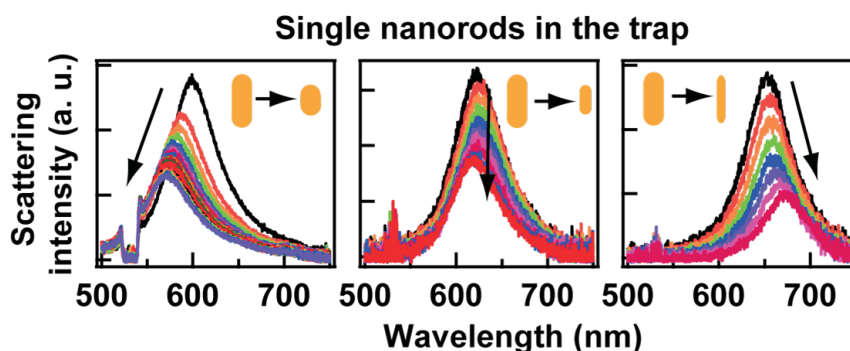
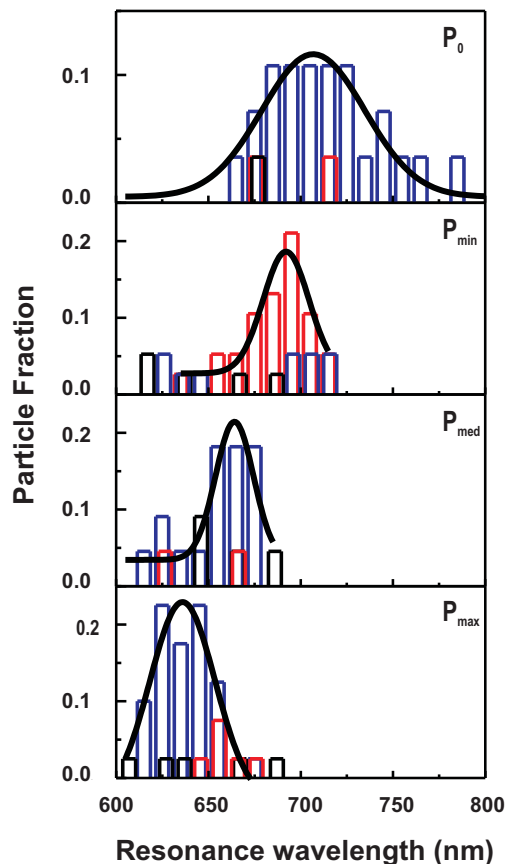


Figure 4.3: Typical time evolution of single-nanorod scattering spectra exhibiting a blue-shift (left), no shift (middle), and red-shift (right) of the resonance wavelength during oxidation in the trap, respectively. Trapping laser power density is 20.1 MW/cm^2 . Time intervals between spectra are 21.1 sec, 19.2, and 27.3 sec for blue-, no-, and red-shift, respectively. The H_2O_2 concentration was 49 mM, the solution temperature was kept at 30°C .

A statistical study of the oxidation behaviors under different laser powers was performed. Figure 4.4 displays histograms of the initial scattering peak wavelength of individual nanorods in the trap under oxidative conditions as a function of trapping power and were sorted into the three categories described above, i.e. blue shift, red shift, or no shift. Without trapping laser (single nanorods on

a surface without drying), 89% of the nanorods blue shifted. At 9.2 MW/cm^2 (P_{min}) trapping power about 60% of the nanorods red shifted, while at powers of 14.7 MW/cm^2 (P_{med}) and 20.1 MW/cm^2 (P_{max}) 77% and 72% of the nanorods blue shifted, respectively. In addition, with increasing trapping power the peak of the distributions blue shifted: 707 nm in P_0 , 692 nm in P_{min} , 664 nm in P_{med} , and 636 nm in P_{max} . With increasing power, increasing number of nanorods melted in the trap on a time scale faster than needed to acquire scattering spectra. These events were not included in the histogram.

Figure 4.4: Histograms of initial plasmon resonance wavelength of Au nanorods under oxidative conditions grouped according to blue shift (blue bars), red shift (red bars), or no shift (gray) of the resonance upon oxidation. Panels represent different trapping powers: P_0 (no trapping, rods deposited on the substrate surface) 25× blue shift, 1× red, 2× no shift; $P_{min}=9.2 \text{ MW/cm}^2$, 8× blue shift, 23× red shift, 7× no shift; $P_{med}=14.7 \text{ MW/cm}^2$, 17× blue shift, 3× red, 3× no shift; $P_{max}=20.1 \text{ MW/cm}^2$, 29× blue shift, 6× red shift, 5× no shift. Black lines depict the results of Gaussian fits for each histogram.



The particle temperature in the optical trap under different laser power densities have been estimated using the Finite-Element method (the calculation method is presented in 4.3). Figure 4.5 depicts the estimated temperature for a nanorod in the optical trap as a function of resonance wavelength under laser power P_{min} , P_{med} , and P_{max} , respectively. From the estimated results, the nanorod temperature increased up to 180°C , much higher than the boiling point of water. This leads to destabilization of the ligands on the nanorod sidewalls which allows for inverting the anisotropy of the oxidation process. As described

in 4.1.1, the oxidation of the nanorods in bulk is anisotropic since the nanorod sidewalls are better protected by the CTAB ligands than the tips. Therefore the oxidation leads to a decreasing aspect ratio and consequently a blue shift of the longitudinal plasmon resonance. The same behavior is observed for individual nanorods on a surface without trapping laser (P_0). Consequently, the observation of a majority of nanorods exhibiting red shifts at low trapping powers indicates that these particles are oxidized such that the aspect ratio increases. This suggests that at low trapping power (P_{min}) the nanorod surface ligands are destabilized, which allows for effective etching the nanorod sidewalls, thus increasing the aspect ratio. Such ligand destabilization is attributed to plasmonic heating of the particle by the trapping laser. The temperature of the red shifting particles at low trapping power is between 90 and 140°C. It has been shown in the literature that CTAB ligands are destabilized in the bulk if the temperature approaches 100°C.[124] In this scenario, nanorods exhibiting no shift are likely to exhibit a lower degree of ligand shell destabilization.

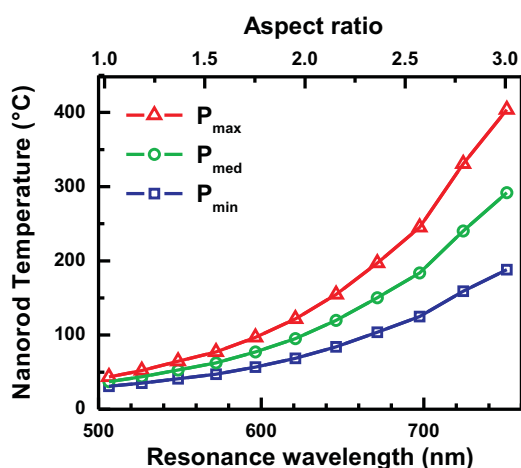


Figure 4.5: Simulated temperature for a nanorod in the optical trap as a function of resonance wavelength under various power densities. The temperature was obtained from COMSOL simulation on the basis of absorption cross sections.

A cross-check experiment was performed by depositing Au nanorods on a glass substrate and applying oxidative solution to the Au nanorods, recorded the scattering with time and plotted the shift of resonance wavelength as function of etching time. Two types of substrate treatment were applied after the nanorod deposition: Au nanorods were dried before adding the oxidative solution; Au nanorods were kept in aqueous CTAB solution until adding the oxidative solution (Figure 4.6a and c). Drying out the water solution usually leads to damages of the CTAB layer around the Au NPs, while the latter treatment preserved the integrity of the CTAB layers. The results were plotted in Figure 4.6b and d. For Au nanorods without CTAB protection during drying procedure, a clear red-shift

was observed; and for the Au nanorods with CTAB protection, a blue-shift was observed with time. This further proves the previous argument that the depletion of CTAB on the Au surface would induce faster etching on the side-walls.

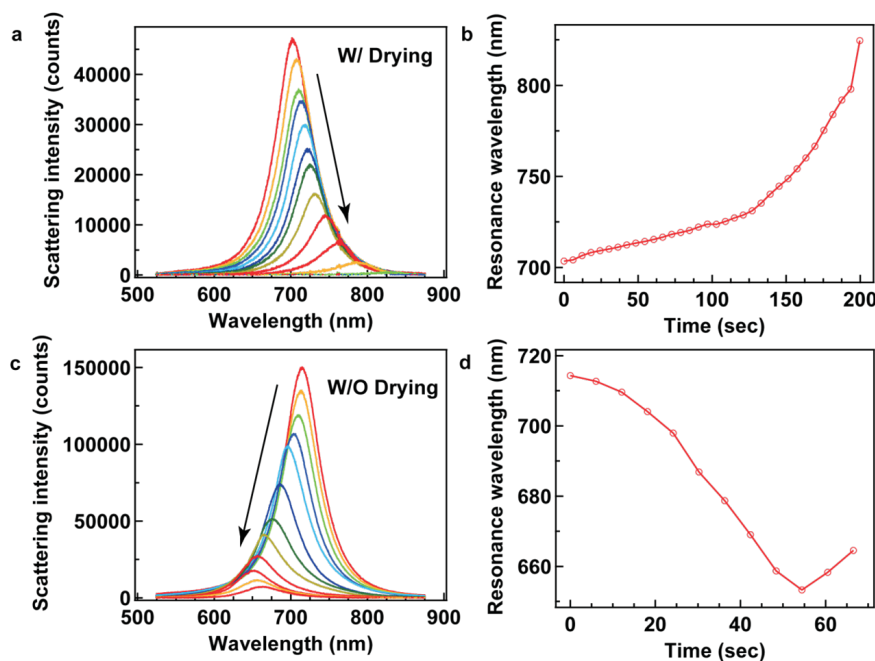


Figure 4.6: (a) Control experiment for single Au nanorod oxidation on a glass substrate with drying. The nanorods were deposited on the substrate, dried in the air, and recorded in the solution after the addition of H_2O_2 . (b) Time dependence of the resonance wavelength for the nanorod shown in (a). (c) Control experiment for single Au nanorod oxidation on a glass substrate without drying. The nanorods were deposited on the substrate and directly recorded in the solution after the addition of H_2O_2 . (d) Time dependence of the resonance wavelength for the nanorod shown in (c).

Upon further increase of the trapping power (P_{med} , P_{max}), the majority of the nanorods blue-shifted. Since now the particle temperature increased up to 180°C (Figure 4.5) the ligand shell can be expected to be further destabilized. Therefore, an additional mechanism counteracting the etching of the sidewalls must come into play to explain the blue shift. As has been shown in the literature pronounced melting and reshaping of Au nanorods has been observed for nanorods in the temperature range from 100 to 250°C accelerating with higher temperature.[121] This dominance of blue shifts at higher temperature is therefore attributed to melting and reshaping of the nanorods which redistributes material from the tip to the sidewalls thereby compensating the etching of the sidewalls.

The overheating of Au nanorods in the optical trap is further demonstrated by comparing the SEM images of Au nanorods that were deposited on the substrate in water (without any oxidants or laser irradiation) and those irradiated with the trapping laser at P_{max} (without any oxidants). The average aspect ratio of the Au nanorods treated with the laser irradiation was 1.9 ± 0.55 , much smaller than that of the nanorods without laser irradiation (2.7 ± 0.3). Three representative SEM images of Au nanorods without laser irradiation (Figure 4.7 a-c) and with irradiation (Figure 4.7 d-f) are presented. A clear trend of nanorod shortening after laser irradiation has been observed. As this experiment was performed without the existence of oxidants, the changes of shape and aspect ratio are contributed from melting and reshaping during laser irradiation. In some extreme cases (d), the temperature on the particle was high enough to reshape the nanorods into spherical shape instantly.

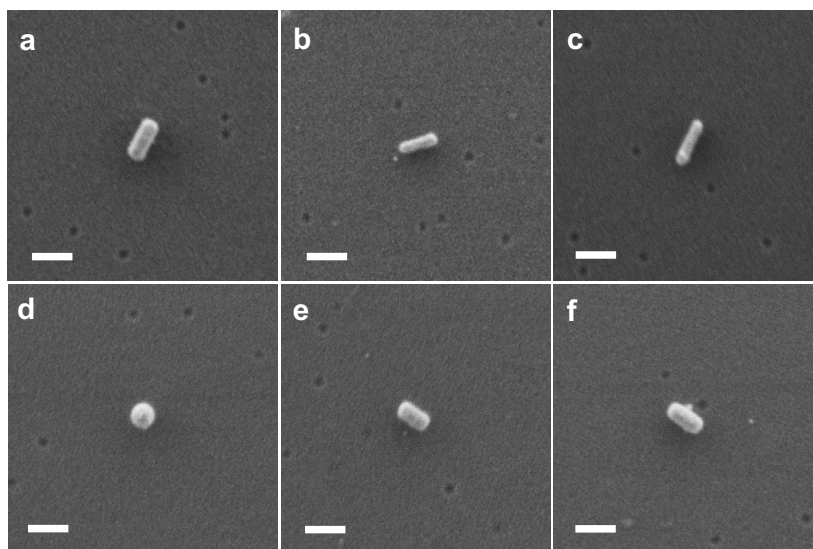


Figure 4.7: Scanning electron microscope (SEM) images of (a-c) three representative Au nanorods deposited on the glass substrate, and (d-f) three representative Au nanorods after laser irradiation for one minute under the laser power P_{max} . No oxidants were introduced. Scale bars, 100 nm.

Even though the particle temperatures were calculated without direct experimental proves, the estimated temperatures are consistent with previous reports of significant off-resonant nanoparticle heating.[125] Another indirect proof is the fact that no bubble nucleation was observed on trapped nanoparticles. Vapor bubbles smaller than 200 nm in diameter would require temperatures in excess of

200°C to nucleate.[125, 126] Our estimated temperature is well below the bubble nucleation temperature.

The plasmonically increased particle temperature also explains the acceleration of the reaction as compared to the bulk room temperature case. For any chemical reaction the energetic activation barrier can be overcome more easily at higher temperatures. In the present case it is particularly intriguing that the particle temperature can exceed the boiling point of the solvent. Therefore this mechanism is expected to apply to a range of chemical reactions on plasmonic particles surfaces. Further evidence for the critical role of the particle temperature from the growth experiment will be discussed in next section.

4.2 Accelerated growth of single Au nanospheres in an optical trap

CTAB-stabilized Au nanospheres synthesized as described in 3.2.2 were used to perform growth experiments. The as-synthesized Au NPs were characterized via UV-Vis-NIR spectroscopy and TEM (4.8). The obtained colloid mainly consisted of spherical nanoparticles (Au@CTAB) of 37 ± 2.5 nm in size and ca. 25% plate- and rod-like morphologies. The plasmon resonance wavelength of the nanospheres was at 530 nm.

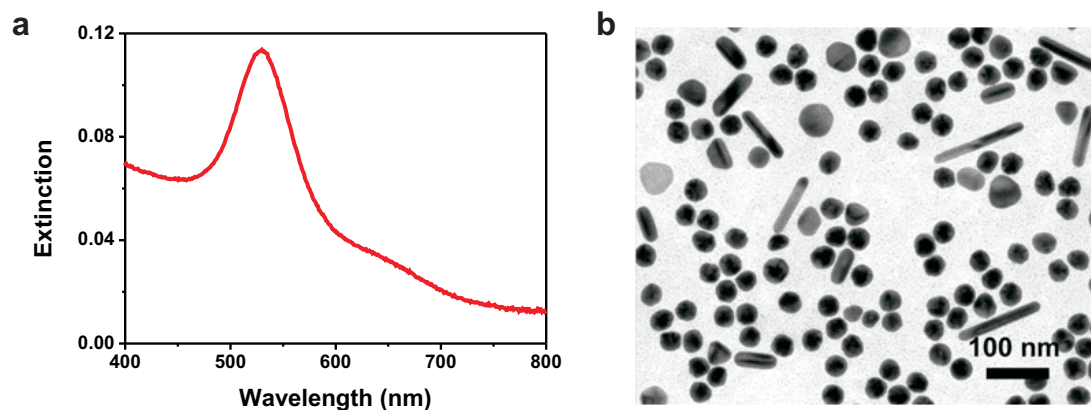


Figure 4.8: (a) Extinction spectrum of as-synthesized Au nanospheres. The plasmon resonance wavelength is 530 nm. (b) Representative TEM image of as-synthesized Au nanospheres. The diameter of the final Au nanospheres is 36.7 ± 2.5 nm.

The experimental conditions for Au nanosphere growth in bulk and in the optical trap are described in section 3.2.2. A mixed CTAB solution with Au(III) ions

and ascorbic acid was used as the growth solution. The growth of Au nanospheres in bulk solution at 95°C was monitored with an UV-Vis spectrophotometer, and the obtained extinction spectra are plotted in Figure 4.9a. The growth of single Au nanosphere in the optical trap was performed under the maximum laser power P_{max} , with the same $[\text{Au(III)}]$ concentration and pH as that of the bulk growth. The scattering spectra of the nanosphere are plotted in Figure 4.9b. The time intervals between spectra were 16.1 sec and 4.8 sec for bulk and single particle growth, respectively. The resonance shift, which represents the growth rate, is plotted against the growth time in Figure 4.9c.

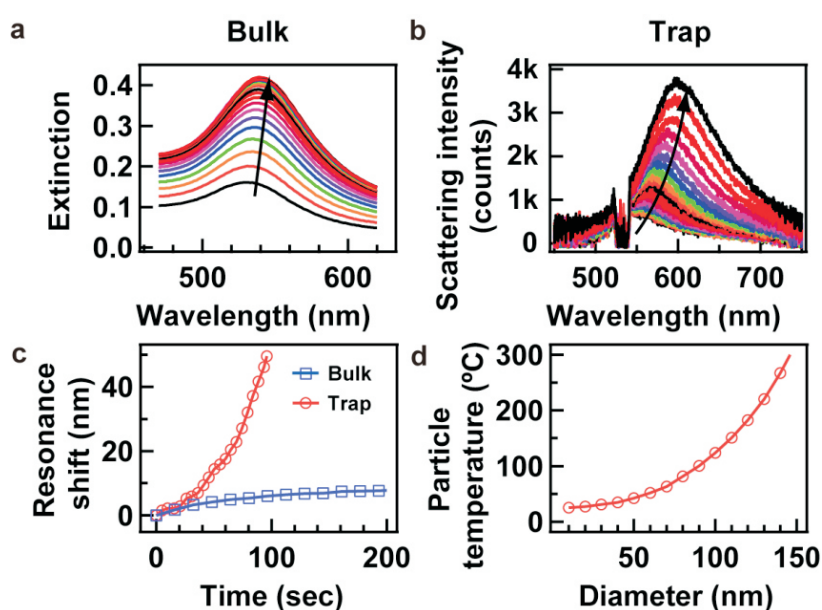


Figure 4.9: Comparison of the growth of Au nanospheres in bulk solutions and of single nanospheres in the optical trap. (a) Time evolution of the extinction spectra of Au nanospheres during growth in bulk solutions at 95°C . Time interval between spectra is 16.1 sec. (b) Typical time evolution of single particle scattering spectra of a Au nanosphere during growth in the trap at 27°C . Time interval between spectra is 4.8 sec. Trapping power density was $P_{max} = 20.1 \text{ MW/cm}^2$. (c) Comparison of the time-dependent resonance wavelength shift between nanospheres in bulk solutions (a) and the optical trap (b). (d) Simulated particle temperature in the optical trap as a function of particle diameter.

In bulk growth, the resonance shift saturated over time, indicating a decreased growth rate. This is due to the depletion of Au(III) ions in the solution. In contrast, in the optical trap, the trapped seed particle is heated and thus grows

faster than the non-trapped seed particles. The 1064 nm trapping laser is far away from the resonance wavelength of $r = 20$ nm Au nanospheres (resonance wavelength at 530 nm), and the temperature elevation is less significant in comparison to that of the Au nanorods (resonance wavelength at 750 nm). However, as the nanosphere grows, its resonance peak red-shifts, and the particle temperature increases exponentially, following the relationship depicted in equation 2.27 (Figure 4.9d). Hence, the temperature on the nanosphere surface increases as the particle radius (R_{NP}) increase. The reaction coefficient k is a function of the activation energy and the reaction temperature (Equation 4.1). Thus the growth rate increases exponentially with temperature. The optothermal effect on the nanoparticle yields accelerated growth of the trapped nanoparticle. Since the heating becomes more efficient with larger particles (Figure 4.9d), this acceleration becomes increasingly important. According to Figure 4.9d, the estimated particle temperature reaches 200°C when the Au NP grows to 120 nm in diameter. This temperature is close to the vapor formation temperature of 200 nm bubble.[125] In our experiment, when the nanoparticle was grown to over 110 nm in diameter (measured with SEM, as described below), we observed bubble formation on the particle surface and destabilization of the trap, which indirectly confirmed the consistency of our temperature estimations with real experiments.

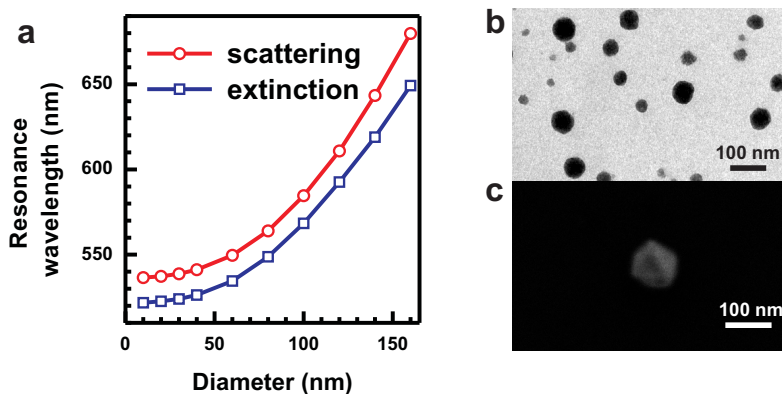


Figure 4.10: (a) The resonance wavelength of scattering (red) and extinction (blue) for Au nanospheres with different diameter. (b) The TEM image of Au nanospheres after growing in the bulk solution under 95°C for 35 minutes. The average particle size is 65 ± 4 nm. (c) The SEM image of a Au nanoparticle after growing in a trap for two minutes. The particle size is 104.6 nm.

In order to monitor the size of the trapped particle, a correlation between the scattering resonance and the particle radius is plotted in Figure 4.10a. The curve of extinction resonance against the particle size follows that of the scattering resonance. Therefore the particle size change can be measured by monitoring the extinction or scattering spectra. By comparing the resonance wavelength of the last spectrum in Figure 4.9a and b with the Figure 4.10a, the size of the grown nanoparticle in the bulk solution was estimated to be 69 nm (extinction resonance at 542 nm), and the size of the grown nanoparticle in the trap was 105 nm (scattering resonance at 590 nm). These values were checked by the TEM image of grown nanoparticle in bulk and the SEM image of the grown nanoparticle in a trap (Figure 4.10b and c). The average particle size was 65 ± 4 nm for the bulk growth particles, and the nanoparticle grown in the trap was measured to be 104.6 nm. The spectroscopic results match well with the SEM imaging results. The growth time for the bulk and the trap growth were 35 minutes and two minutes, respectively. A much bigger nanoparticle was grown within 20 fold shorter time in the trap. At the seed concentration in this experiment, the trapped particle grows at virtually constant Au(III) concentration in contrast to the bulk reaction where Au(III) is depleted. Therefore it is possible to grow bigger particles much faster with the optothermally-enhanced nanoparticle growth method in an optical trap.

4.3 Characterization of the optical trap

The characterization of the optical trap, such as the optical forces applied on the particle, the equilibrium position of the trap, the temperature change in the trap induced by optothermal effect, is essential for single particle trapping. In this section, the optical trapping forces on the nanoparticles are estimated with FDTD and dipole approximation (see also section 2.3). The optothermal induced temperature increase on the particle and in solution is simulated using the Finite-Element Method.

4.3.1 Characterizing the optical trapping force

A laser-equipped dark field microscope for optical trapping (see figure 3.1) was used to optically confine nanoparticles in solution and to perform further chemical manipulation. In order to achieve a stable trapping of nanoparticles, the property of the optical trap, especially the optical trapping forces, need to be characterized.

The TEM_{00} mode of a focused laser beam can be approximated to be a Gaussian beam (Figure 4.11), and the generated electromagnetic field is expressed as follows:[127]

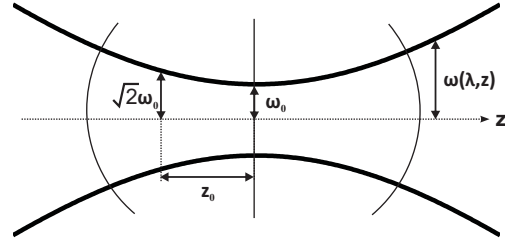
$$E(\lambda, r, z) = E_0(\lambda) \sqrt{\frac{2}{\pi}} \frac{\omega_0(\lambda)}{\omega(\lambda, z)} \exp \left\{ -\frac{r^2}{\omega^2(\lambda, z)} + i \left[k(\lambda) \left(\frac{r^2}{2R(\lambda, z)} + z \right) + \zeta(\lambda, z) \right] \right\} \quad (4.2)$$

In this cylindrical coordinate system, the z -axis is along the laser propagation and the r -axis is perpendicular to the laser propagation direction. The laser focus point is set to be the center $r = 0, z = 0$, and the laser beam width is a function of the waist width $\omega_0(\lambda) = 2\lambda/(\pi \cdot NA)$:

$$\omega(\lambda, z) = \omega_0(\lambda) \sqrt{1 + \left(\frac{z}{z_0(\lambda)} \right)^2} \quad (4.3)$$

with the Rayleigh range $z_0(\lambda) = (\pi\omega_0^2(\lambda))/(n\lambda)$ and the radius of curvature of the wavefront $R(z) = z[1 + z_0(\lambda)/z]$, and $\zeta(z) = \arctan(z/z_0(\lambda))$ is the Gouy phase. The electric field at the beam center is $E_0(\lambda) = \sqrt{2\eta P}/(\omega_0(\lambda))$, and η is the characteristic impedance of the medium in which the laser beam is propagating. In water, $\eta = \sqrt{\mu/\varepsilon} = 142.7\Omega$. P is the laser power density at the center of the laser beam at the waist ($r = z = 0$). And the numerical aperture is $NA = 1$ for the water immersion objective.

Figure 4.11: An illustration of a Gaussian beam passing through a medium along the z -axis. The width of the beam $\omega(\lambda, z)$, the waist width at $z = 0$ is ω_0 , and the Rayleigh range $z_0(\lambda)$.



Introducing the calculated electric field from equation 4.2, and the calculated polarizability from the modified Clausius-Mossotti equation (equation 2.37) into the equation 2.35 (\vec{F}_{grad}) and 2.36 (\vec{F}_{scat}), the optical forces in the trap are calculated for a $r=20$ nm Au nanosphere (Figure 4.12).[128] The equilibrium position of the trap is close to the laser focus, where the total force is approximately zero ($\vec{F} \rightarrow 0$ pN) and the particle is confined near this point due to the attractive optical forces acting on the particle. As shown in Figure 4.12, the equilibrium position is on the z -axis of the Gaussian beam, and slightly away from the laser focus, with $z_e = 11$ nm. The maximum trapping force is 0.262 pN.

The calculations above are based on the approximation that the trapping laser beam is a Gaussian beam. This is true for objectives with small NA ($NA < 1$), but invalid when $NA \geq 1$. Introducing the values $\lambda = 1064$ nm and $NA=1$ into

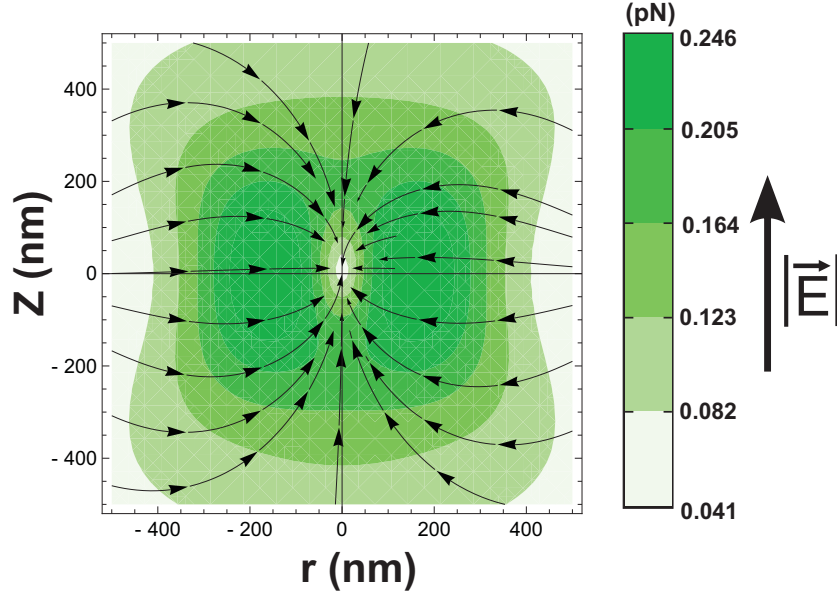


Figure 4.12: The total optical forces on a $r=20$ nm Au nanosphere in water. The laser power $P=0.1$ W. The contour arrows point to the direction of the total optical force ($\vec{F} = \vec{F}_{grad} + \vec{F}_{sct}$), the color bar indicates the absolute value of the total optical force within the trap. The maximum trapping force is 0.262 pN, and the equilibrium position (where $\vec{F}=0$ fN) is at $r=0$, $z_e=11$ nm, near the laser focus point.

the equation $\omega_0(\lambda) = 2\lambda/(\pi \cdot NA)$, the waist width of the laser beam $\omega_0 = 677.4$ nm is obtained. While a FDTD simulation for a 1064 nm laser beam passing through a thin lens with $NA=1$ yields $\omega_0 = 514$ nm. Therefore the calculations above give only a rough estimation of the optical forces.

A more precise analysis of the optical trap is based on FDTD calculations. From section 2.3, the total force contains contributions of the gradient force and the scattering force, which are proportional to the real and imaginary part of the particle polarizability, respectively. When the trapping laser wavelength is fixed, the polarizability of the nanoparticle of a certain size is constant, and the trapping forces can be determined by the electromagnetic field induced by the trapping laser. FDTD provides numerical calculation of the fields and the total force at each point in the system can be calculated according to equation 2.35 and 2.36. Figures 4.13a,b compare the optical forces calculated from the Dipole Approximation and FDTD for an $r=20$ nm Au nanosphere in the optical trap ($P=0.1$ W). The results of the two methods match quite well while the equilibrium

position shifts from $z_e=11$ nm with Dipole Approximation to $z_e=40$ nm with FDTD calculation, and the maximum force along r -axis shifted by 100 nm. This may due to the approximations in the laser beam as a Gaussian beam.

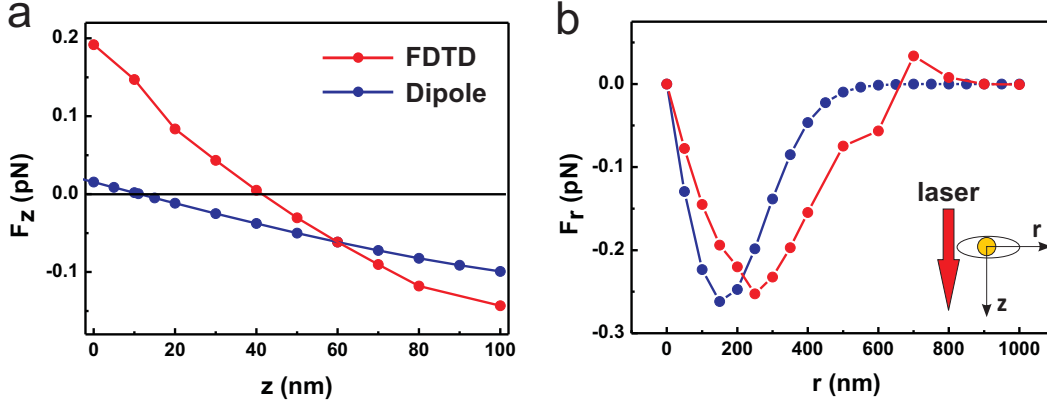


Figure 4.13: Calculated optical forces on an $r=20$ nm Au nanoparticle along (a) z -axis ($r=0$) and (b) r -axis ($z=z_e$) calculated with the Dipole Approximation (red) and FDTD (blue), respectively. The equilibrium point is $z_e=11$ nm using the Dipole Approximation and $z_e=40$ nm using the FDTD calculation, respectively. The maximum optical force on the r -axis is $F_r = -0.262$ pN with the Dipole Approximation and $F_r = -0.252$ pN with the FDTD calculation. The inset indicates the r - and z - axis. F_z points toward the equilibrium point of the trap and F_r points toward the center of the trap. The laser power at the focus $P=0.1$ W.

In real experiments, the nanoparticle is not a stationary object at equilibrium, but randomly diffuses within the trap. The movement of a nanoparticle in an optical trap is analogous to a spring obeying the Hooke's law.[129, 130] The particle encounters a thermal force (F_t), which drives the particle out of the equilibrium position; a restoring force (F_r), which drives the particle back to the equilibrium position; a damping force (F_d), which is caused by the viscous drag force of the solution and an inertial force (F_i):

$$F_i + F_d + F_r = F_t, \quad (4.4)$$

Equation 4.4 above can be written as:

$$m \frac{\partial^2 x(t)}{\partial t^2} + \gamma \frac{\partial x(t)}{\partial t} + \kappa x(t) = \sqrt{2k_B T \gamma} R(t). \quad (4.5)$$

in which the thermal force F_t (Langevin force) is a random Gaussian process describing the Brownian motion in a potential with temperature T , Boltzmann's

constant k_B and a noise term $R(t)$. The inertial force is neglected in comparison to the damping force, since the Reynolds number of nanoparticles is very small. The damping force is determined by the drag coefficient $\gamma = 6\pi\eta r$ according to the Stoke's law. The restoring force F_r is linearly proportional to the displacement of the particle: $F_r = \kappa x$. The trap stiffness κ represents the total optical force acting on the nanoparticle. The harmonic potential of the particle is determined by:

$$U(x) = F_r \frac{x}{2} = \frac{\kappa_x}{2} x^2, \quad (4.6)$$

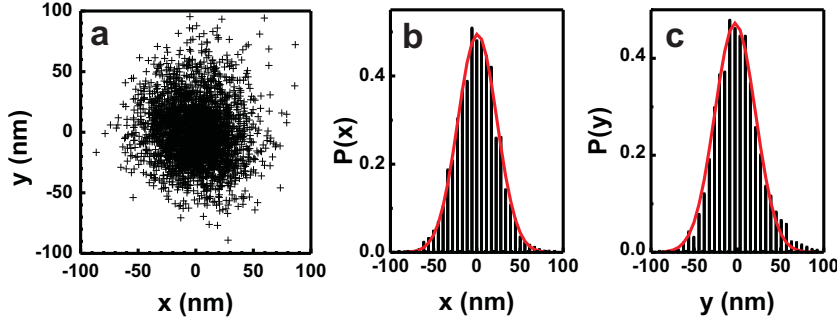


Figure 4.14: (a) A typical diffusion trajectory of a nanorod in an optical trap over 3000 frames (within one minute) at 30° C and the probability density over 3000 frames (1min) along the (b) x -axis and (c) y -axis. Gaussian fitting to the probability density histograms (red) gives the width $\sigma_x=22.6$ nm, $\sigma_y=23.6$ nm, and the trap stiffness $\kappa_x=8.2$ fN/nm, $\kappa_y=7.5$ fN/nm.

The trap stiffness can be experimentally determined by recording the nanoparticle motion with a digital video camera and extracting the distribution of the nanoparticle positions over time. Figure 4.14 shows a typical trajectory of a nanorod in an optical trap over 3000 frames (within one minute). With sufficient statistics, the position distribution shows a Gaussian distribution. The probability density function is then determined by:

$$P(x) = \frac{1}{\sigma_x \sqrt{2\pi}} \exp -\frac{(x - \mu)^2}{2\sigma_x^2}, \quad (4.7)$$

From Boltzmann statistic, the potential energy $U(x)$ of the particle in the trap follows the distribution:

$$P(x) = C \exp -\frac{U(x)}{k_B T}, \quad (4.8)$$

in which C is a constant which normalizes the probability distribution with $\int P(x)dx = 1$. Therefore, the potential energy can be experimentally plotted:

$$U(x) = -k_B T \ln P(x) + k_B T \ln C. \quad (4.9)$$

Introducing the value of Boltzmann's constant $k_B = 1.3806488 \times 10^{-23}$ J/K, the experimentally determined $U(x)$ into the equation 4.9, the trap stiffness κ can be experimentally determined. The probability density $P(x)$ and $P(y)$ for the trajectory in Figure 4.14a is then plotted in Figure 4.14b and c, and the stiffness of the trap is then calculated: $\kappa_x = 8.2$ fN/nm, $\kappa_y = 7.5$ fN/nm. The spring model provides the trap stiffness in real experiment. Such model is limited to x and y dimension, while the optical forces along the laser propagation direction (z) is difficult to measure with the current experimental condition.

4.3.2 The optothermal effect in the optical trap

The optical heating of Au NPs, as discussed in section 2.2, is a result of non-radiative relaxation of electron oscillations into the nanoparticle lattice upon optical excitation. Optical heating with resonant wavelength lasers has been investigated in many reports,[14, 27, 59, 131] but optical heating with off-resonant IR lasers in an optical trap was only mentioned recently.[120, 126] Optically heated nanoparticles transfer heat into the surrounding, causing a temperature gradient near the particle surface.

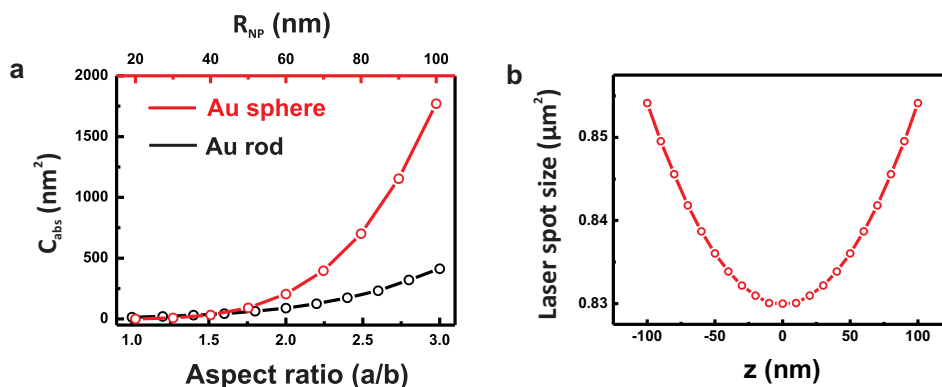


Figure 4.15: (a) The absorption cross section of Au nanospheres (red) v.s. nanoparticle radius (R_{NP}) and Au nanorods (black) v.s. the aspect ratio (a/b) at the trapping laser wavelength $\lambda = 1064\text{nm}$. (b) FDTD calculated trapping laser spot size along z -axis.

The Finite-Element Method was used to numerically characterize the optical induced temperature change near the particle surface. The Au nanorod was modeled as a cylindrical tube with two half spheres at the ends; and the Au nanosphere was modeled as a perfect sphere. The absorption cross sections (C_{abs}) and the resonant wavelength of the Au nanospheres and Au nanorods (longitudinal mode) with various sizes are calculated with the Mie theory and FDTD simulation, respectively (Figure 4.15a).

According to equation 2.30 ($Q = C_{abs}P/V_{NP}$), three parameters have influence on the particle temperature: the absorption cross-section of the particle C_{abs} , the particle volume V_{NP} , and the laser power density P . The absorption cross-section and particle volume are intrinsic properties of the particle. The laser power can be measured experimentally. Since the equilibrium position of the trap is off-focus, i.e. the beam profile of the equilibrium position ($\omega(z_e)$) is slightly different from the beam center (ω_0). Comparing the actual laser spot size at the equilibrium position to that on the beam center, a variance of less than 5% was found from FDTD calculations, as illustrated in Figure 4.15b.

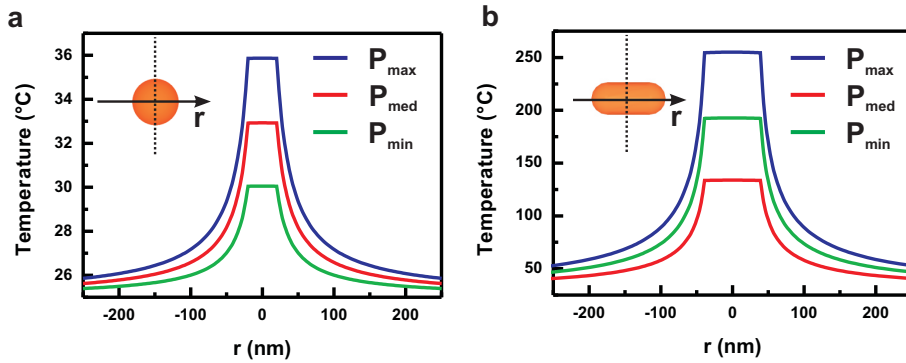


Figure 4.16: The temperature distribution of (a) $R_{NP}=20\text{nm}$ Au nanosphere and (b) $78 \times 30 \times 30 \text{ nm}$ Au nanorod along the r -axis (as shown in the inset) in an optical trap. The trapping laser power densities are $P_{max}=20.1 \text{ MW/cm}^2$, $P_{med}=14.7 \text{ MW/cm}^2$, $P_{min}=9.2 \text{ MW/cm}^2$.

From the experimental trajectories of nanoparticles in the trap (such as in Figure 4.14a), one can tell that the nanoparticle is diffusing in an area $r \leq 100 \text{ nm}$ around the trap center ($r=0, z=z_e$). The actual power density applied on the nanoparticle is the average power density within this $r_{real}=100 \text{ nm}$ area (6.4% of the total power, calculated from FDTD). For the trapping laser power used in this work, the calculated laser power densities are: $P_{max}=20.1 \text{ MW/cm}^2$, $P_{med}=14.7 \text{ MW/cm}^2$, $P_{min}=9.2 \text{ MW/cm}^2$, for measured laser power of 0.102 W, 0.072 W, 0.045 W, respectively. Hence, the temperature distributions of Au nanosphere

and Au nanorod in the optical trap are calculated numerically with the Finite-Element Method, as shown in Figure 4.16.

4.4 Conclusions

Plasmonic heating has been applied to enhance and modify the reactions on the surface of single Au NPs in an optical trap. The outcome and kinetics of the reactions is mainly determined by the particle temperature, which can exceed the solvent boiling point due to plasmonic heating. In particular, single Au nanorods in the trap can be etched such that their aspect ratio either increases or decreases depending on the trapping laser power, while in bulk it exclusively decreases. The elevated temperature due to plasmonic heating was also shown to accelerate the single Au nanosphere growth in the optical trap, giving much bigger nanoparticle within much shorter reaction time in comparison to the bulk growth.

The employment of optical trapping reduces the particle reaction down to single particle level. The miniaturization of reaction volume is expected to lead to high-throughput, portable analytical and sensing applications, and to fundamental insights into single-molecule chemical reactions.[132–134] Emerging lab-on-a-chip applications frequently employ micro- or nanofluidic structures.[135–138] However, these approaches do not change the outcome of the chemical reaction. In this work, individual optically trapped plasmonic particles can alter and accelerate chemical reactions on the surface by plasmonic heating to yield different and faster results, as compared to the corresponding bulk reactions. Since optical trapping is compatible with emerging nanofluidic systems we expect this method to be applicable to many reactions in the vicinity of particle surfaces, in nanofluidic systems and for fundamental studies in colloidal chemistry.

5 Optothermal manipulation of gold nanoparticles on cell membranes

A large number of vital processes, such as photosynthesis, nutrient recognition and signaling occur across or on the membranes of biological cells.[139] Mapping, sensing and manipulation of cellular membranes and their related processes have attracted a great deal of attention, and the applicability of several nanomaterials, such as quantum dots,[140, 141] magnetic nanoparticles[142] and carbon nanotubes[143] is being actively explored. Au NPs have emerged as appealing optical markers for living cells due to their chemical stability and unique optical properties.[144] Sensing cell membrane processes with Au NPs may benefit not only from the high sensitivity of their localized surface plasmon resonance,[10, 11] but also from their potential as ultrasensitive Surface-Enhanced Raman Scattering (SERS) reporters.[145] Moreover, the spatially-confined thermal manipulation of the plasma membrane can become feasible by irradiating the Au cores with an external laser source.[146] Inspired by the previous work, in which localized phase transitions of artificial vesicles were induced by plasmonically heated Au NPs attached to the membrane,[27] we explore the plasmonic heating of Au NPs to living cell membranes.

In this chapter, Au NPs are used as powerful optical toolboxes for the investigation and manipulation of cellular membranes. First, a general, versatile and controlled strategy to immobilize Au NPs on cellular membranes, while retaining their full capabilities for sensing and optothermal manipulation in living cells, is presented. Second, the diffusion of lipid labeling Au NPs on cellular membranes is studied by single particle tracking of the Au markers. Last, it is shown how the immobilized Au NPs can serve as localized heat sources to manipulate cellular membranes optically.

5.1 Covalent labeling of cell membranes with gold nanoparticles

To date, various approaches have been exploited for cell surface labeling with Au NPs. Several methods rely on the rather uncontrolled electrostatic attachment of weakly stabilized nanoparticles to the cellular surface,[147, 148] which usually results in particle aggregation under physiological conditions. Others deal with the direct adsorption or surface functionalization of the nanoparticles with ligands/antibodies that specifically bind to membrane receptors/antigens.[12, 22] The latter approaches are useful for membrane protein studies, but do not provide the freedom for general cell membrane investigations, and may be disadvantageous for some applications. For example, plasmonic heating investigations may be limited because thermal changes can easily induce protein denaturation and subsequent loss of biological function. Furthermore, the plasmon sensing capability can be reduced as a result of the large coating thickness imposed by the size of the proteins. Clearly, in order to exploit the full capabilities of Au NPs as active nano-tools on cellular membranes, ways to attach them controllably and directly to membrane lipids are needed.

In this section, a general, versatile and controlled strategy to immobilize Au NPs on cellular membranes, while retaining their full capabilities for sensing and optothermal manipulation in living cells, is presented. This method is based on Au NP/lipid binding via maleimide-thiol reaction prior to cell incubation and therefore avoids the nonspecific, uncontrolled anchoring of the Au NPs to random cell membrane components.

The approach to covalently bind AuNPs to lipids on cell membranes can be described in three steps. First, the surface chemistry of Au nanospheres is modified. CTAB or citrate stabilized Au NPs are not stable in a high ionic solution, such as cell medium, buffer solution, and therefore membrane labeling with a non-aggregated sample is not possible. Here, PEG (polyethyleneglycol) is grafted on the nanoparticles to increase their colloidal stability in high ionic strength media and biocompatibility. To provide the surface reactivity for lipid binding, a maleimide derivatization reaction is applied to the PEGylated Au NPs. Second, the nanoparticles are chemically bound to fusogenic liposome membranes via a maleimide-thiol reaction between the nanoparticle and thiolated lipids. Finally, liposome-cell membrane fusogenesis enables the incorporation of the nanoparticle-labeled lipids to the living cell membrane surface. Experimental descriptions of these steps are presented in section 3.2.3 and their results are discussed here.

CTAB is a surfactant extensively used in the synthesis of noble metal, as well as magnetic nanoparticles of varying sizes and shapes.[7, 96, 100, 149, 150] Hence, for the general applicability of the labeling approach, CTAB-stabilized

5.1. Covalent labeling of cell membranes with gold nanoparticles

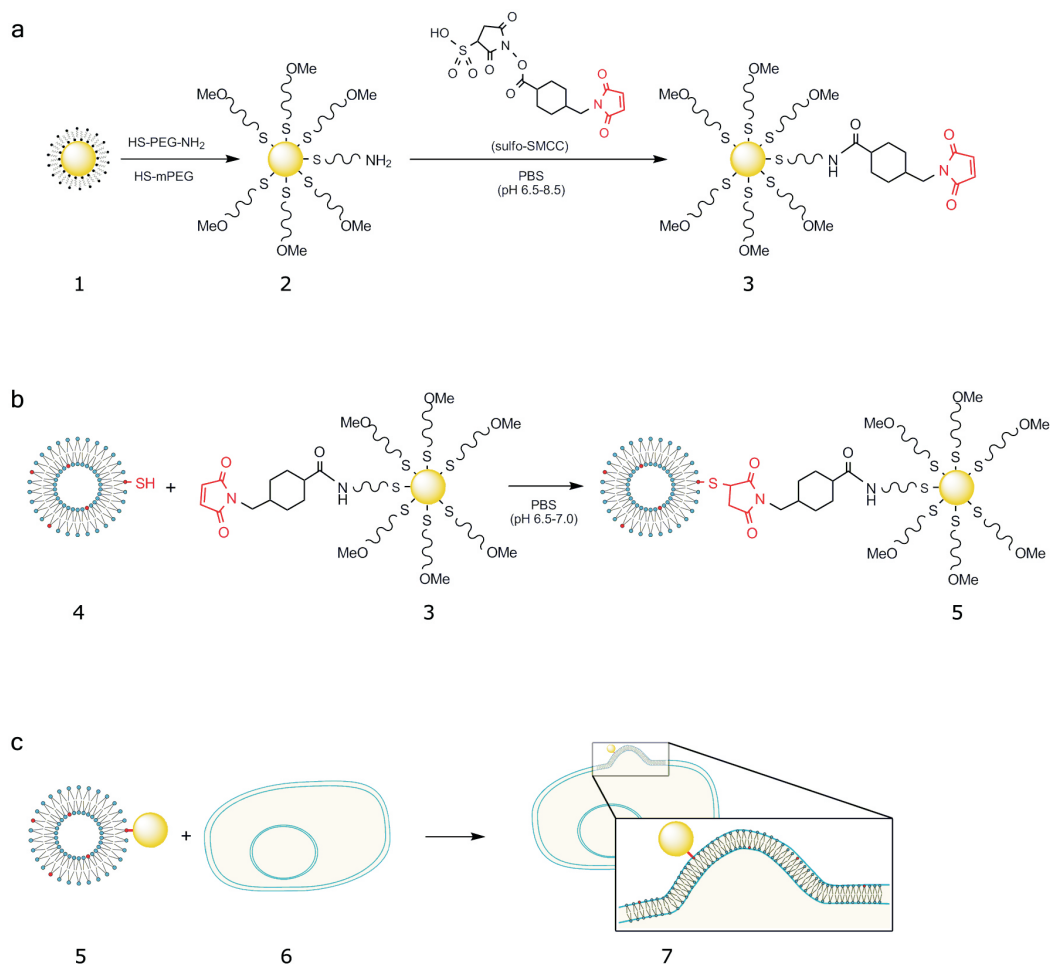


Figure 5.1: Illustration depicting the general strategy for surface modification, lipid binding, and final cell membrane incorporation of Au NPs. (a) PEGylation and subsequent maleimide functionalization of CTAB-capped Au nanospheres. (b) Conjugation of the maleimide-functionalized nanospheres to liposomes containing a thiolated lipid (PTE-SH). (c) Fusion of the Au@mal-tagged liposomes with the cell membrane of Jurkat cells. The numbers refer to Au@CTAB (1), Au@mPEG-SH/HS-PEG-NH₂ (2), and Au@mal (3) nanoparticles, respectively; small liposomes containing PTE-SH (4), Au@mal bound to PTE-SH in liposomes (5), living (Jurkat) cell (6), and Au@mal tagged to PTE-SH in the cell membrane, after liposome/membrane fusogenesis (7).

Au nanospheres (Au@CTAB) have been selected as a model colloid. The TEM image and the extinction spectrum of as-synthesized Au@CTAB nanoparticles are shown in Figure 5.2a and c. The diameter of the nanospheres is 64 ± 3 nm from TEM measurement. The plasmon band of the nanospheres is centered at 537 nm.

The general strategy used for labeling Au NPs with Jurkat cell membranes is shown in Figure 5.1. In the first step (a), CTAB molecules on Au NP surfaces (Au@CTAB, 1) are exchanged with a mixture of mono-(mPEG-SH) and heterobifunctional HS-PEG-NH₂ (PEGylation). Thereafter, the terminal amino groups of the PEGylated particles (Au@mPEG-SH/HS-PEG-NH₂, 2) are reacted with an amino-reactive, heterobifunctional, crosslinker sulfo-SMCC (see section 3.2.3.2 for details) bearing a terminal maleimide functionality. As such, Au NPs (Au@mal, 3) are stable in biological media and contain the maleimide-functionality. In the second step (b), the Au@mal nanoparticles are bound to a thiol-ended lipid PTE-SH (see section 3.2.3.2 for details) which is part of small fusogenic liposomes, via maleimide-sulfhydryl chemistry. Finally (c), fusogenesis of the Au@mal-labeled liposomes (c, 5) with the cellular membrane (c, 6) leads to the controlled delivery of the Au NPs to the cellular membrane (c, 7).

In order to functionalize CTAB-capped AuNPs with maleimide functionality, a mixture of mono-(mPEG-NH₂) and heterobifunctional (HS-PEG-NH₂) PEG was used to exchange with CTAB molecules from the Au NP surface (5.1a). The PEGylation has a 2-fold function. First, it increases the colloidal stability of the nanoparticles in the high ionic strength cellular medium, where the interparticle repulsion potential (in this case determined by the positive CTAB bilayer) can be fully screened leading to irreversible particle aggregation. Second, it makes them biocompatible by reducing their cytotoxicity[15] and resistant against protein adsorption.[15] In addition, using a binary mixture of thiolated PEGs bearing reactive and nonreactive terminal groups, serves as a platform for further surface modification, where the number of reactive terminal groups (-NH₂) can be simply adjusted by modifying the ratio of both polymers. As an additional advantage, the PEG-based coating allows for a direct control over the coating thickness by just changing the polymer molecular weight.

As a result of PEG grafting, the ζ -potential of Au nanospheres changed from +40 to 0 mV, in agreement with previous reports.[15] As further confirmed by the optical spectra shown in Figure 5.2c, the Au@mPEG-SH/HS-PEG-NH₂ nanoparticles remained stable after washing and final redispersion in PBS buffer (pH 7.6). No plasmon shift, only a slight decrease in extinction intensity was observed, suggesting that only minor particle destabilization occurred.

After PEGylation, the terminal amino groups of the PEGylated AuNPs (Au@mPEG-SH/HS-PEG-NH₂) were reacted with a heterobifunctional cross linker sulfo-

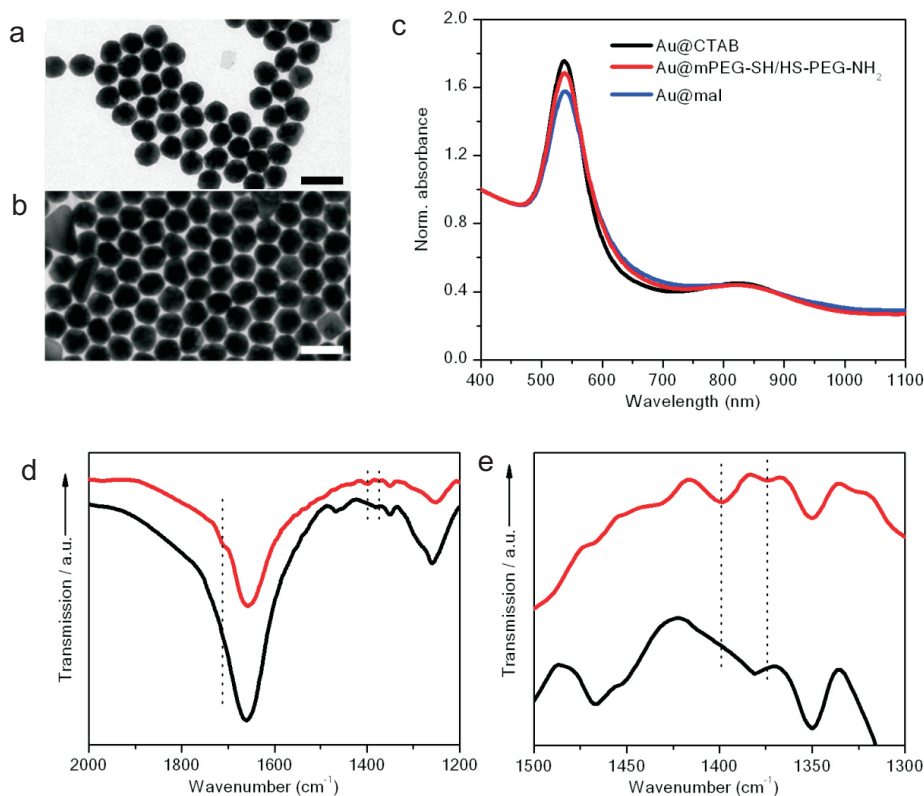


Figure 5.2: Representative transmission electron micrographs of the Au NPs before (a), and after (b) PEGylation/maleimide functionalization. Scale bars, 100 nm. (c) vis-NIR spectra of the Au@CTAB colloid (black), after surface modification with mPEG-SH/HS-PEG-NH₂ (red), and after maleimide derivatization (blue). FTIR spectra of Au@mPEG-SH/HS-PEG-NH₂ and Au@mal nanoparticles (black and red curves, respectively) in the range of 2000 - 1200 cm⁻¹ (d), and an enlargement in the 1500 - 1300 cm⁻¹ range (e).

SMCC, bearing a terminal maleimide functionality and an amino-reactive succinimide ester terminal (Figure 5.1a). Sulfo-SMCC and analogous cross-linkers containing succinimidyl ester and maleimide groups have been traditionally exploited for maleimide derivatization of amino-functionalized self-assembled monolayers on gold films.[152, 153] Here, the usage of this cross-linker is extended for maleimide-functionalization on the nanoparticle surface. The reaction between the succinimide ester and the primary amino group is typically performed first to minimize hydrolysis, and under controlled pH conditions, to prevent reaction of

the maleimide group with amines.[21, 154] The succinimide ester in sulfo-SMCC couples to primary amines via amide bond formation at a buffer pH 6.5-8.5, and the coupling between maleimide and sulfhydryl groups via thioether linkage is buffered at pH 6.5-7.0.[154] Therefore, the reaction between Au@mPEG-SH/HS-PEG-NH₂ and sulfo-SMCC took place in PBS buffer pH 7.6, and the washed Au@mal nanoparticles were redispersed in PBS pH 6.9 for further binding to sulfhydryl groups in step two.

Maleimide derivatization was confirmed by Fourier transform infrared (FTIR) spectroscopy (Figure 5.2d and e). The FTIR spectrum of the Au@mal nanoparticles shows the characteristic asymmetric stretching mode of the imidyl group (O=C-N-C=O, 1712 cm⁻¹), the symmetric maleimide C-N-C stretching (1399 cm⁻¹) and the maleimide C-N stretching (1374 cm⁻¹), in agreement with the literature.[153, 155] The characteristic amide I or amide II bands of the newly formed amide linkage did not appear in the FTIR spectra, probably because the concentration is too low to be detected. The ζ -potential of Au@mal nanospheres remained unchanged with respect to that before the maleimide derivatization ($\zeta = 0$ mV). As shown in the TEM images in Figure 5.2c, no observable changes occurred to the nanoparticles after maleimide derivatization. They remained stable, unaggregated, as further confirmed by the spectrum displayed in Figure 5.2d, where only a minor decrease in the plasmon intensity was observed.

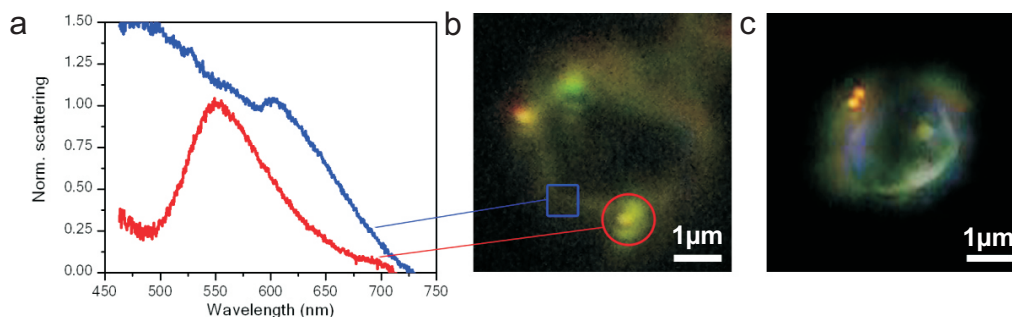


Figure 5.3: (a) Scattering spectra of the areas highlighted in (c): vesicle's lipid bilayer (square) and Au@mal nanoparticle bound to it (circle). DFM image of a DPPC giant unilamellar vesicle (containing PTE-SH) after incubation with Au@mal (c) and Au@mPEG-SH/HS-PEG-NH₂ (d) nanospheres.

In the second step, Au@mal nanoparticles were bound to vesicles via maleimide-thiol reaction. Large liposomes (2-5 μ m) consisting of SOPC, DOPE and a small amount of a thiolated lipid (PTE-SH) were produced using the electroformation method (see section 3.2.3). Liposomes composed of SOPC and DOPE have been reported to favor liposome fusogenesis with the cellular membrane.[103, 104]

PTE-SH lipids provide a few thiol anchor points for the selective binding of the Au@mal nanoparticles, as sketched in Figure 5.1b. The ratio of maleimide groups on the nanoparticles to PTE-SH lipids in the liposomes was fixed to 1:5 and the reaction was performed in PBS buffer pH 6.9. This process gave SOPC/DOPE liposomes labeled with Au@mal nanoparticles anchoring to PTE-SH lipids. However, the labeling Au NPs diffused fast on the liposomes as the liposome membranes are in the fluid phase at room temperature. This issue hampered the realization of single particle spectroscopy (DFM) measurements on the Au NPs. In order to overcome this drawback we prepared DPPC/PTE-SH liposomes. The higher phase transition temperature (41°C) of DPPC slows down the diffusion of Au NPs on DPPC liposomes at room temperature, enabling DFM characterization. Figure 5.3b displays a representative DFM image from an Au@mal-labeled DPPC/PTE-SH vesicle. A relatively low particle loading (ca. 2-3 Au@mal per vesicle) was typically achieved. By increasing the number of PTE-SH lipids in the vesicles and the concentration of Au@mal nanoparticles added, higher particle loading could be obtained. Importantly, most of the particles were bound to the vesicles in a single-particle fashion, effectively scattering green light under dark field illumination and showing a clear localized surface plasmon resonance characteristic of individual Au nanospheres of ca. 60 nm, with a plasmon band centered at ~ 550 nm (see spectrum in Figure 5.3a). Compared to the spectrum of the ensemble in water (Figure 5.2c), the plasmon band of the single particles investigated was typically red-shifted. This is mainly ascribed to the refractive index increase from water ($n=1.33$) to the aqueous glucose solution (0.13 M, $n=1.34$), where the Au@mal-labeled vesicles are suspended for DFM characterization, as well as to slight deviations from the sphericity of the particles measured.

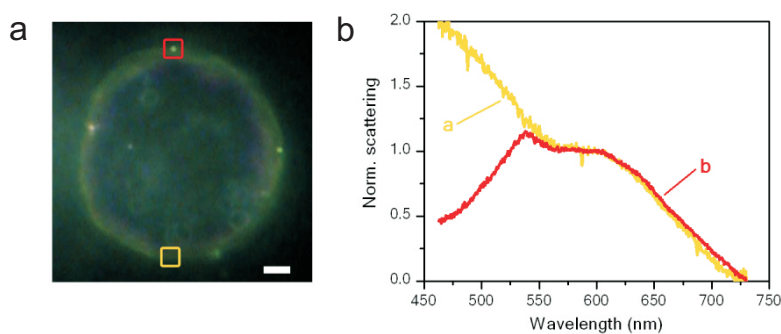


Figure 5.4: (a) Representative DFM image of a Jurkat cell after incubation with the Au@mal-labeled fusogenic liposomes. Scale bar, 2 μm . (b) Scattering spectra of the cell membrane and of a gold nanoparticle on it, yellow and red squares in (a), respectively.

Incubation of DPPC/PTE-SH vesicles with Au NPs without maleimide functionality (Au@mPEG-SH/HS-PEG-NH₂ nanoparticles) under identical conditions typically yielded a lower particle loading, with many particles attached as aggregates (Figure 5.3c), rather than as individual particles. The lack of preferential binding sites at the Au NP surface toward PTE-SH results in unspecific adsorption. In contrast, the binding of the Au@mal nanoparticles is a chemically driven process directed by the high affinity of the maleimide terminal groups at the Au NP surface toward PTE-SH at the vesicles. The number of thiolated lipid per vesicle was kept low so as to minimize particle aggregation and favor single particle binding.

In order to deliver Au NPs to the cellular membrane, small fusogenic vesicles (120-620 nm, hydrodynamic diameter) were used. The fusogenic vesicles were composed of SOPC, DOPE and PTE-SH. The ratio of PTE-SH lipids to maleimide groups on the Au NP surface was set to 5:1, in order to minimize the number of unbounded Au@mal after the maleimide-thiol reaction, since they could potentially bind to other thiolated membrane components.

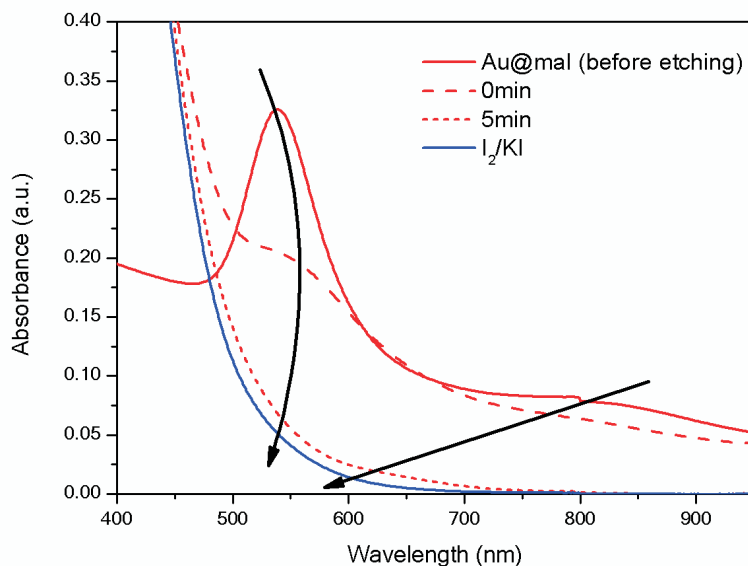


Figure 5.5: Time evolution of the vis-NIR extinction spectra of Au@mal nanoparticles upon addition of an I₂/KI mixture. The spectrum of the oxidized colloid matches that of the oxidizing I₂/KI mixture.

In the third step, the Au@mal-labeled vesicles were incubated with Jurkat cells to induce the fusogenesis (and lipid exchange) with the cellular membrane and thereby promote the incorporation of the Au@mal-tagged PTE-SH lipids (Figure 5.1c). As a result, single gold nanospheres (typically ca. three to five Au NPs per

cell) are effectively delivered to the cellular membrane and identified under the DFM as green scattering spots (Figure 5.4a). By following the approximation of Au@mal labeled fusogenic liposomes filled with fluorescein toward the cells in a DFM setup adjusted to detect scattering and fluorescence, we have observed that from ca. 10 events of contact liposome-cell ca. 2 lead to the successful delivery of Au NPs to the cell membrane. Figure 5.4b shows representative scattering spectra of the plasma membrane and of an Au@mal nanoparticle bound to it. The membrane shows a large scattering throughout the visible, particularly pronounced at the particle's plasmon resonance and lower wavelengths. While the scattering contribution from the membrane cannot be fully overcome in the background-corrected spectrum of the Au NP, its plasmon mode can be distinguishable at ~ 540 nm.

In order to elucidate whether the as-delivered Au@mal nanoparticles are on the cell surface, a control experiment based on the I_2/KI etching method was performed. It has been reported that Au NPs attached to the cellular surface are readily oxidized upon addition of a membrane non-permeable I_2/KI mixture.[147] This makes them easily distinguishable from those being internalized into the cells. Figure 5.5 displays the time evolution of the extinction spectra of Au@mal nanoparticles upon addition of an I_2/KI mixture. 5 min after the addition of I_2/KI , the spectrum of the oxidized Au@mal matched that of the I_2/KI mixture, indicating that all nanoparticles were oxidized. Through Vis-NIR spectroscopy, it was confirmed that the Au@mal nanoparticle in PBS was rapidly oxidized in the presence of I_2/KI .

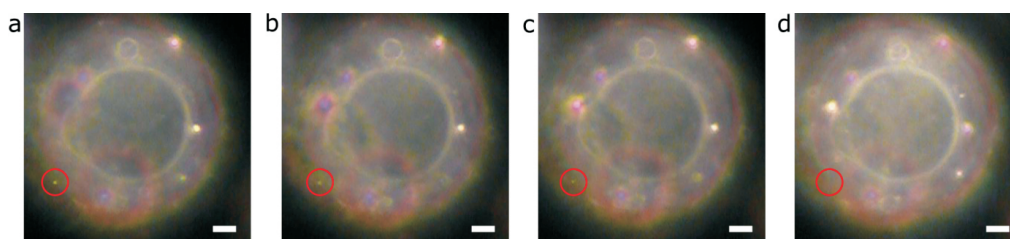


Figure 5.6: DFM images showing the oxidation of an Au@mal nanoparticle (highlighted) on the cell membrane of a Jurkat cell. The images are taken before (a) and 10 s (b), 16 s (c), and 24 s (d) after the addition of an I_2/KI aqueous solution. Scale bars, $2 \mu\text{m}$.

The oxidation of Au@mal nanoparticles anchored to the cell membrane as a consequence of liposome-assisted delivery was directly performed under DFM ob-

ervation. Figure 5.6 illustrates the oxidation results for Au@mal nanoparticles on the cellular membrane. The scattering from the single Au NP showed dramatical decreases only a few seconds after the addition of the oxidizing mixture and fully vanished after 24 seconds of reaction. These results confirm that the Au@mal nanoparticles are accessible to the I₂/KI mixture, and therefore it can be concluded that Au@mal were effectively located on the cell membrane surface.

5.2 Optothermal manipulation of gold nanoparticles on cell membranes

Au NPs have been reported to be good lipid markers for the investigation of lipid diffusions in cellular membranes.[87, 156] Here Au@mal lipid markers have been tracked by dark field microscopy for the investigation of lipid motions in the living cell membrane. Au NPs also serve as local heating sources upon laser irradiation (section 4.2). During laser irradiation, the electric field of the incident light drives the large amount of mobile electrons in the Au NP to oscillate, and the energy absorbed by the electrons is converted into heat. This generated heat is conducted through the medium and dissipated over a certain distance. The temperature enhancement and the size of the locally heated area depend on the absorption coefficient of the Au NP, the particle size, laser wavelength, laser power, as well as the thermal properties of the surrounding medium. For a 60 - 70 nm Au NP in water, the heating area is sub-micrometer in size. This allows one to study the influence of localized heat on cell membranes. Hence, Au@mal nanoparticles are not only lipid markers for single particle tracking measurements, but also localized heat sources to manipulate the lipid motion in the membrane.

5.2.1 Gold nanoparticle diffusion on living cell membranes

The lateral motion of lipids in the membrane is widely used to characterize the membrane properties, such as the membrane fluidity and the membrane structure. In this work, the lipid diffusion was tracked by following the movement of Au NPs that were labeled to lipids on cell membranes using the strategy discussed in 5.1. DFM was used to observe Au NPs that served as lipid markers, and the diffusion trajectories of Au NPs were extracted by following the Au NPs positions using a self-written program. In order to determine the diffusion mode, the mean square displacement (MSD, $\langle r^2 \rangle$) of the Au NP diffusion can be calculated from the diffusion trajectories. The MSD is the mean of the squared distance between the starting point at time t_0 and a point at a later position at time $t = n\Delta T$ as expressed follows:

$$\begin{aligned}
\langle r^2(t) \rangle &= \langle r^2(n\Delta T) \rangle \\
&= \frac{1}{N+1} \sum_{i=0}^N \{ [x(i\Delta T + n\Delta T) - x(i\Delta T)]^2 + [y(i\Delta T + n\Delta T) - y(i\Delta T)]^2 \}
\end{aligned} \tag{5.1}$$

where ΔT is the data acquisition time, N is the total number of frames and $n = 0, 1, 2, 3, \dots, N$, x and y indicate the positions of the Au NPs at time t . In this work, $\Delta T = 20$ ms.

The time dependence of the MSD gives information on the diffusion of Au@mal nanoparticles. The diffusion rate is described by the diffusion coefficient D ($\mu\text{m}^2/\text{s}$). On a short time scale, a linear correlation between MSD and time can be found, as described in the free diffusion expression $\langle r^2(t) \rangle = 4Dt$ (equation 2.40) and the D for the corresponding diffusion can be obtained.

The diffusion of the PTE-SH labeling Au@mal nanoparticle on the cell membrane was compared to the reference samples in which Au@mal and Au@mPEG-SH nanoparticles were attached to the cell membrane nonspecifically. Figure 5.7 summarizes the characteristic diffusion behavior of these three types of Au NPs on the cell membrane: Au@mal labeled to PTE-SH lipids on the cell membrane via fusogenesis (Figure 5.7b); Au@mal attached to the cell membrane in a non-specific manner by direct addition of Au NPs into the cell suspension (Figure 5.7c and d); Au@mPEG-SH attached to the cell membrane nonspecifically due to the absence of maleimide anchor points to the cell membrane (Figure 5.7e). The trajectories shown in panels b-e are $(x - y)$ projections of the particle diffusion on the cell surface, recorded at a constant focal plane in the DFM, as schematically sketched in Figure 5.7a.

Visually, the Au@mal nanoparticles bound to PTE-SH lipids and incorporated on the cell membrane via fusogenesis appeared to be immobile on the cell surface. Analysis of the diffusion trajectories revealed that these nanoparticles performed a rather slow and spatially limited diffusion over small cell membrane regions (Figure 5.7b). The average diffusion coefficient of 21 Au@mal nanoparticles on cell membranes was $\bar{D} = 0.0023 \mu\text{m}^2 \text{s}^{-1}$. In the above experiments, the cells were exposed at room temperature (ca. 21°C), much lower than the physiological temperature (37°C). Therefore, the diffusion of PTE-SH labeling Au@mal on Jurkat cell membranes at 37°C incubation was investigated. The average diffusion coefficient of 20 PTE-SH labeling Au@mal nanoparticles was $\bar{D} = 0.0038 \mu\text{m}^2 \text{s}^{-1}$, in the same order of magnitude as that at room temperature.

The slow and spatially confined diffusion behavior of Au@mal nanoparticles is consistent with the reported constrained lipid diffusion in cellular membrane compartments.[74, 156] For instance, single particle tracking of 40 nm Au NPs

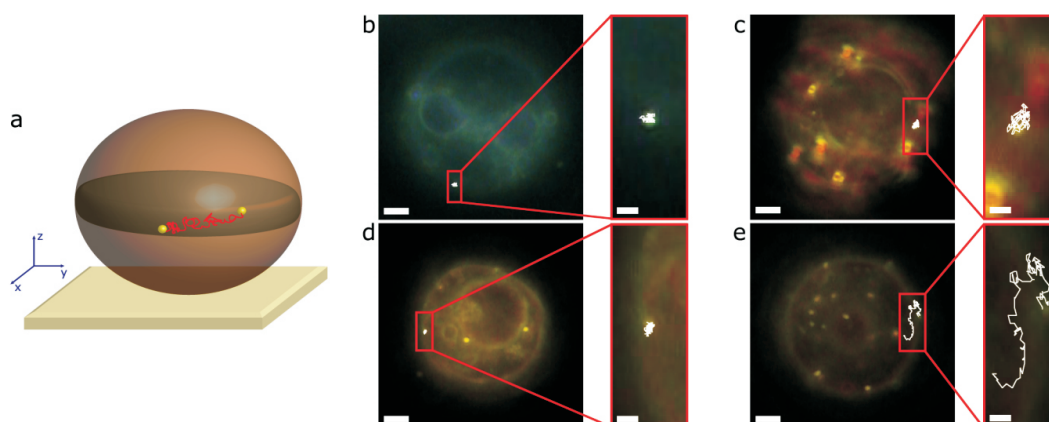


Figure 5.7: (a) Representative sketch (not to scale) depicting the diffusion of an Au NP on the cell surface. The particle remains at a constant focal plane during DFM observation and single particle tracking. (b-e) Optical DFM images showing representative two-dimensional ($x - y$ projection) diffusion trajectories of individual Au NPs on the surface of Jurkat cells. In each case Au-labeling was achieved via cell membrane fusogenesis with Au@mal-labeled liposomes (b) or after direct cell incubation with Au@mal (c, d) or Au@mPEG-SH (e) nanospheres. Scale bars, $2\mu\text{m}$. Right panels, enlargements (scale bars, 500nm). A Semrock 532 nm single-edge dichroic beam splitter was used for DFM imaging (c-e).

conjugated to DOPE lipids (via antigen-antibody recognition) has shown that the diffusion coefficient of DOPE in FRSK cells can be reduced $\sim 10\times$ (from 0.044 down to $0.0068 \mu\text{m}^2 \text{s}^{-1}$) after treatment with Jasplakinolide.[74] Jasplakinolide is a cyclic peptide that creates a coarser but stronger actin mesh work in the plasma membrane[157] and therefore sharply reduces lipid mobility. The immobilization of Au@mal nanoparticles on the cell membrane could be due to an increase in the amount of picket proteins anchored along the membrane skeleton or to a preferential PTE-SH partitioning to less fluidic membrane domains.[156] Nevertheless, the diffusion results support the mechanism according to which Au@mal-labeled liposomes merge with the cell membrane, lipid exchange occurs and PTE-SH lipids, to which the Au@mal nanoparticles are bound, integrate into the membrane.

Au@mal and Au@mPEG-SH nanoparticles directly incubated with Jurkat cells (in the absence of the carrier fusogenic liposomes) were investigated as references.

In both cases the yield of Au NP attachment to the cell surface was lower than that obtained when using the carrier Au@mal-labeled fusogenic liposomes. In contrast to the slow diffusion above, the unspecifically attached Au@mal and Au@mPEG-SH nanoparticles presented different diffusion behaviors. Most of the Au@mal nanoparticles diffused faster on the cell membrane over larger distances (Figure 5.7c, $D = 0.05 \mu\text{m}^2 \text{s}^{-1}$), while others performed a more limited, yet fast diffusion (Figure 5.7d, $D = 0.106 \mu\text{m}^2 \text{s}^{-1}$). Upon direct incubation with the cells, the Au@mal nanoparticles can unspecifically react with any thiolated component of the plasma membrane (e.g., cysteine residues from enzymes or ion channels). Therefore, different diffusion lengths and times (Figure 5.7, panels c and d) occur depending on the Au@mal-tagged membrane entity. In this context, the surface chemistry of the nanoparticles plays a major role on their nonspecific binding and diffusion on the cellular membrane.

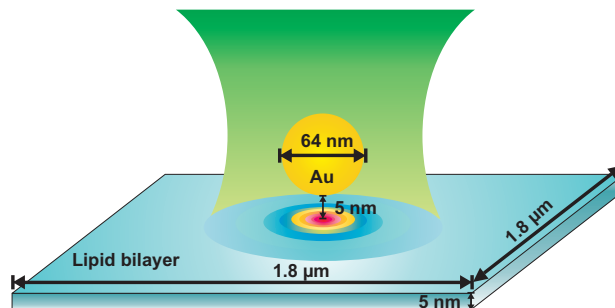
As for the Au@mPEG-SH nanoparticles, the lack of functional reactive groups at the particles' surface resulted in weak particle adsorption at the cellular membrane, with a consequent quick diffusion ($D=0.0815 \mu\text{m}^2 \text{s}^{-1}$) over much longer distances (Figure 5.7e). In contrast to the above cases, most of the adsorbed Au@mPEG-SH nanoparticles detached from the cell surface after few seconds.

5.2.2 Optothermal manipulation of gold nanoparticle diffusion on cell membranes

Laser induced Au NP heating of cells has been reported to cause pore formation on the membrane and induce cell death.[146, 158] In those studies, a large number of Au NPs were introduced into the cell medium, and laser irradiation was applied to heat up many Au NPs simultaneously. In this work, only one single Au@mal nanoparticle was irradiated in each experiment to avoid instant cell damage. The effectively heated area was limited to sub-micrometer size, and the laser power was precisely controlled to vary the membrane temperature in the range of 21~100°C.

The Finite-Element Method has been used to estimate the laser induced temperature on the cellular membrane. Figure 5.8 sketches the model of a 64 nm Au NP above a 5 nm thick lipid bilayer. The average size of Jurkat cells is ca. 10 μm , much larger than the size of the 64 nm Au NP. Hence, the cell membrane near the Au NP was approximated as a two-dimensional lipid bilayer sheet. The average hydrodynamic diameters of Au@CTAB and Au@mal nanoparticles were 77 nm and 93 nm respectively, thus one can estimate the PEG layer around Au@mal to be ca. 8 nm thick. Varying the distance between the Au NP and the membrane from 5 nm to 10 nm, the maximum temperature differences on the membrane is approx. 5°C. Hence, the spacing between the Au@mal surface and the cell mem-

Figure 5.8: Representative sketch (not to scale) depicting the system of Au@mal-labeled lipid on the cell membrane for finite-element simulation. The Au@mal nanosphere has a diameter of 64 nm, the lipid bilayer is represented as a $1.8 \mu\text{m} \times 1.8 \mu\text{m} \times 5 \text{ nm}$ two dimensional sheet, and the smallest distance between the Au NP and the membrane was set to 5 nm.



brane was set to be 5 nm (this may overestimate the temperature by maximum 5°C). Both the Au NP and the lipid bilayer were surrounded by a $20 \mu\text{m}$ water sphere (not shown in the figure). A 532 nm laser with a ca. $5 \mu\text{m}$ laser spot size was used to irradiate the Au NP. As the plasmon resonance of single Au@mal nanoparticles of 64 nm is ca. 540 nm, the Au NPs have large absorption cross-sections at 532 nm. The resonant laser irradiation could effectively be absorbed by the Au NPs.

Figure 5.9a shows the estimated temperature profile at the center of the lipid bilayer. The temperatures on the upper and lower surface of the membrane were different due to different distance from the Au NP, the temperature at the center presents the average temperature on the membrane. The membrane closest to the heating source (point O) i.e. Au NP, has the highest temperature, and the membrane temperature decays quickly with increasing distance from the Au NP. The effective heated membrane, where the membrane temperature is above the biological temperature (37°C), is within a 300 nm (diameter) area. Figure 5.9b further shows the relationship between the highest temperatures at the center of the membrane and the laser power densities. Fitting these data gives a quasi-linear equation of the highest membrane temperature at point O and the laser power density P : $T_{max} = 21.29 + 0.405P$. Hence the localized membrane temperature can be adjusted by tuning the applied laser power.

In order to investigate the influence of local heating to the Jurkat cell membrane, the PTE-SH lipid markers, i.e. Au@mal nanoparticles, were irradiated with a 532 nm laser, and the diffusion of PTE-SH labeling Au@mal nanoparticles were monitored by single particle tracking. By setting the laser power density (P) to $163 \text{ kW}/\text{cm}^2$ (ca. 87°C), the Au@mal nanoparticles started to diffuse faster on

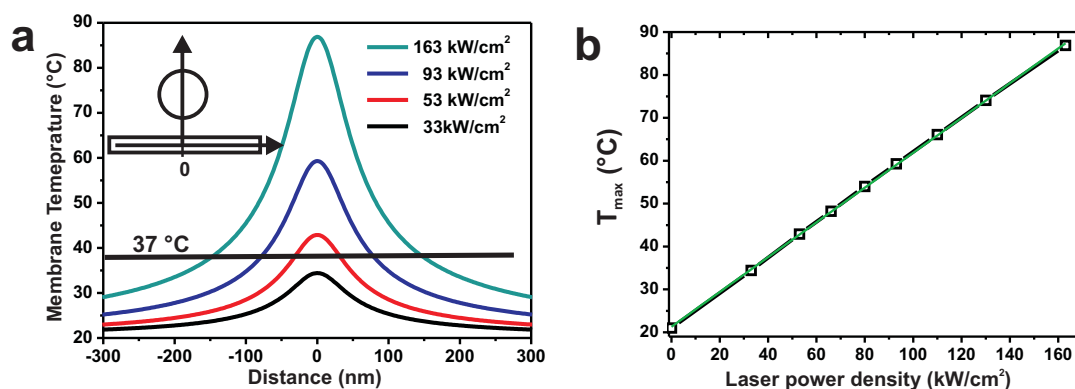


Figure 5.9: (a) Steady-state temperature at the center of the membrane as a function of the distance to the nanoparticle center for four power densities of the heating laser P . The horizontal line marks the physiological temperature (37°C) for Jurkat cells. (b) The highest temperature (T_{max}) at the center of the membrane (black square) with respect to different heating laser power densities. Fitting the temperature with laser power density (green curve) gives a quasi-linear relationship between P and T_{max} : $T_{max} = 21.29 + 0.405P$.

the cell membrane, and over a much larger area (Figure 5.10b). In comparison to the diffusion trajectories before laser irradiation (Figure 5.10a), the localized heat on the membrane had significant influence on the diffusion of the Au@mal nanoparticle on the cell membrane. Also, it is worth noting that no morphology changes of the laser irradiated cells were observed during the measurement. The fast diffusion of Au@mal nanoparticle continued for more than 10 minutes after the laser irradiation was stopped.

A further study of the local heat influence on the cell membrane was performed by following the Au@mal nanoparticle diffusion under several membrane temperatures T_{max} . Figure 5.11a demonstrates the average diffusion coefficient of Au@mal particle when the localized membrane temperature T_{max} induced by laser irradiation was 21°C ($P=0 \text{ kW/cm}^2$), 40°C , 50°C , 55°C , 60°C , 70°C , 75°C and 80°C , respectively. The diffusion under localized heating (Figure 5.11a, $\bar{D}=0.0017 \mu\text{m}^2 \text{ s}^{-1}$ at 40°C) matches well with the diffusion under 37°C cell incubation. Both bulk heating and localized heating below 40°C did not change the PTE-SH lipid diffusion behavior on the cell membrane. A clear increase of diffusion coefficient was observed when the membrane temperature reached $\sim 60^{\circ}\text{C}$. In comparison to the average D at 21°C ($\bar{D}=0.0023 \mu\text{m}^2 \text{ s}^{-1}$), the average D at 75°C increased 20

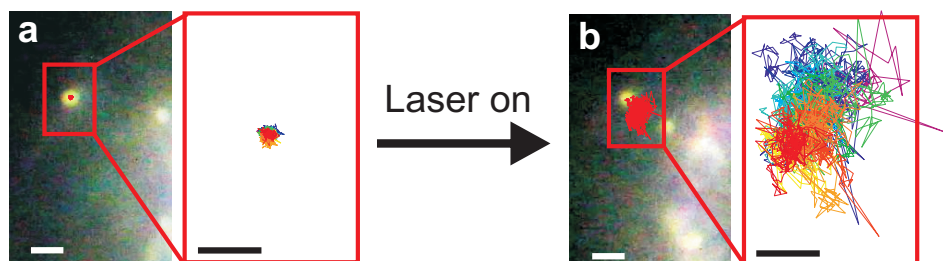


Figure 5.10: Representative DFM images and diffusion trajectories of Au@mal-labeled PTE-SH on the Jurkat cell membrane (a) before, (b) during laser irradiation. Scale bars, 1 μm . Right panels, enlargements of the trajectories (scale bars, 400 nm).

times ($\bar{D}=0.0512 \mu\text{m}^2 \text{s}^{-1}$). The nanoparticle diffusion area (diffusion area within 54 sec) also increased with increasing membrane temperature (Figure 5.11a, inset). Au@mal labeled PTE-SH diffused in an area of 100-150 nm (diameter) at a membrane temperature below 40°C. The diffusion area raised to ca. 500 nm (diameter) when the temperature was 60°C. The lipid marker diffused through a even larger area (ca. 1 μm) when the membrane temperature was above 70°C.

The slow and confined diffusion of Au@mal nanoparticle was broken by increasing the membrane temperature to over 60°C via laser induced local heating. Both the diffusion coefficient and the diffusion area increased dramatically. From the previous study of Au NP diffusion on artificial liposomes under laser irradiation,[27] the increase of diffusion coefficient occurred together with the membrane phase transition: from slow and confined diffusion in the gel phase to fast and free diffusion in the fluid phase. This change of diffusion is reversible, i.e. the fast diffusion slows down when the membrane temperature falls below the phase transition temperature. However, in the case of Au@mal diffusion on the cell membrane, the fast diffusion did not show any sign of decrease as measured for 10 minutes after stopping the laser irradiation. It seems that the cellular membrane phase transition is not likely to induce the observed accelerated Au NP diffusion behavior.

The cellular membrane is a mixed-lipid bilayer with incorporated membrane proteins, ion channels and receptors. The cytoskeleton, which anchors to certain proteins in the membrane, controls the membrane movement and adjusts the membrane shape.[159] The cytoskeleton may be influenced by the heat generated from laser irradiated Au@mal particle and consequently affect the membrane movement. Jurkat cells treated with cytochalasin D, an enzyme that disrupts actin microfilaments in living cells,[160] were labeled with Au@mal via fusogen-

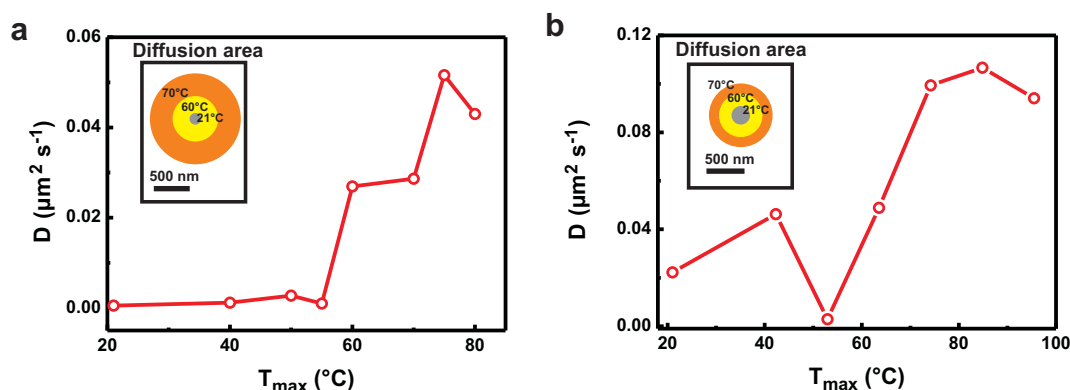


Figure 5.11: Average diffusion coefficient of Au@mal-labeled PTE-SH on the cell membranes of (a) normal Jurkat cells and (b) Jurkat cells treated with cytochalasin D, under various membrane temperature (optical heating induced membrane temperature T_{max} as calculated in Figure 5.9b). Insets: Au@mal-labeled PTE-SH diffusion area on the cell membranes under various membrane temperature T_{max} : 21°C (grey circle), 60°C (yellow circle) and 70°C (orange circle).

esis as described in section 5.1. Optical heating experiments were performed on the treated Jurkat cells and the diffusion trajectories of the labeling Au@mal particles were recorded. The change of the diffusion coefficient of a typical Au@mal nanoparticle under various local heating temperature was determined (Figure 5.11b). The diffusion coefficient at 21°C was $0.022 \mu\text{m}^2 \text{s}^{-1}$, 10 fold higher than the average D for cells with cytoskeleton ($\bar{D}=0.0023 \mu\text{m}^2 \text{s}^{-1}$). These results suggest that the existence of cytoskeleton may have a significant influence on lipid diffusion in the cellular membrane. With increasing membrane temperature, the diffusion coefficient increased by ca. 5 times in the cells without cytoskeleton. The impact of localized heat on the lipid diffusion in the cells without cytoskeleton is less significant than that in the nontreated Jurkat cells, suggesting that the control of cytoskeleton over membrane may be one reason for this increase of diffusion coefficient. Nevertheless, the diffusion change upon localized heating still exists in the absence of cytoskeleton and more information is required to explain this phenomenon.

The diffusion coefficients of PTE-SH labeling Au@mal particles on normal Jurkat cell membranes within the first, second and third minute of laser irradiation (membrane temperature $T_{max} = 60^{\circ}\text{C}$) were calculated to be $0.0037 \mu\text{m}^2 \text{s}^{-1}$, $0.0028 \mu\text{m}^2 \text{s}^{-1}$, and $0.020 \mu\text{m}^2 \text{s}^{-1}$, respectively. The diffusion coefficient in

the third minute is significantly higher than in the first two minutes. This phenomenon, however, was not observed for membrane temperatures above 70°C, where similar diffusion coefficients were found in different laser irradiation period. From our observation, the irradiation time required to accelerate the Au@mal diffusion depends on the membrane temperature: the higher the membrane temperature, the shorter the required time. Heating cells over 41°C starts to induce protein denaturation, which changes the protein solubility and functionality.[161] Membrane protein denaturation may reduce the amount of proteins in the cellular membrane, such as cytoskeleton anchored proteins, resulting in the increase of lipid diffusion in the membrane. The duration of the protein denaturation strongly depends on the temperature.[162] The denaturation process is slow at low temperatures (50°C),[163] but fast at high temperatures (above 70°C). The slow and confined diffusion of Au@mal nanoparticles on the cell membrane could be the result of an increase amount of membrane proteins, such as cytoskeleton anchored membrane proteins, in the cellular membrane. Localized heating of the cellular membrane may induce local denaturation of membrane proteins, and may influence the degree of freedom of lipid motion in the cellular membrane.

5.3 Conclusions

A new strategy to bind individual Au NPs covalently to lipids in living cell membranes via cell membrane-vesicle fusogenesis was presented. This strategy was applied to bind 64 nm Au nanospheres to PTE-SH lipids in the membrane of Jurkat cells. The CTAB-stabilized Au nanospheres were first grafted with a PEG mixture to protect the nanoparticles in high ionic cell media, and to enable further maleimide derivatization on the Au nanosphere surface. The maleimide derivatized Au NPs were bound to small fusogenic vesicles via maleimide-thiol binding to thiolated lipids in vesicle membranes. Here PTE-SH, a thiolated lipid with sulfhydryl group was used to realize the Au@mal-lipid binding. The Au NP-cell membrane binding was achieved through vesicle-cell membrane fusogenesis. Since this approach is based on lipid tagging through covalent binding, it allows for the preservation of the optothermal capabilities of the original Au NP. Additionally, as the Au NP-lipid is incorporated on the cell membrane via fusogenesis, without the involvement of specific membrane protein or antibody-antigen binding, this strategy may also be applied to other cell lines.

The diffusion of lipid labeling Au@mal nanoparticles on cell membranes was investigated by single particle tracking. As a result of lipid binding, the Au NPs performed a distinctively slow and spatially limited diffusion on the cell surface at both 21°C and 37°C. Optothermal manipulation of the Au@mal nanoparticles enabled controlled localized heating of the cellular membrane up to sub-

micrometer size. Optically heating the cell membrane to 87°C accelerated the Au@mal nanoparticle diffusion on cell membranes: their diffusion area increased and their diffusion coefficient increased 20-fold comparing to those at 21°C. Since this phenomenon is irreversible, it seems that the reason of membrane phase transition could not explain the change of diffusion upon heating, in contrast to studies on artificial membranes. The study of Jurkat cells treated with cytochalasin D, which removed the actin network in cells, revealed a much faster lipid diffusion at 21°C and a 5-fold increase of diffusion coefficient at 75°C. These results suggested that the existence of cytoskeleton or membrane proteins that anchored to the cytoskeleton may influence the diffusion of PTE-SH labeling Au@mal particles. The diffusion coefficient for different laser heating duration was compared and at 60°C it increased after laser irradiation for more than one minute, while at 70°C it increased almost instantly. The observation of the diffusion of Au@mal accelerates after certain laser irradiation time points toward the possibility of membrane protein denaturation in the locally heated membrane, which could influence the attachment of cytoskeleton, and reduce the amount of membrane proteins in the membrane. For this further evidences and investigations are needed. Nevertheless, we have shown that the optical heating of the labeling Au NPs to manipulate the local temperature of cellular membranes remotely opens a new way to optically manipulate the local behavior of biological cells.

6 Conclusions and outlook

Here we have successfully employed an optical trap to investigate single gold nanoparticle reactions in solution. The optical trap provided a stable 3D confinement of the nanoparticle without being immobilized to other surfaces. Dark field microscopy and spectroscopy have been combined with the optical trapping method to monitor the nanoparticle reaction spectroscopically. The oxidation of a single gold nanorod in an optical trap showed distinct behaviors in comparison to that in the bulk solutions. Varying the trapping laser power, their aspect ratio either increases or decreases, while in bulk it exclusively decreases. Such phenomenon was attributed to the optical heating of the nanorod to over 100°C, which on one hand destabilizes the CTAB bilayer on the particle surface and on the other hand reshaped the particle. Moreover, the high temperature on the nanoparticle accelerated the reaction rate, which was also observed in single nanoparticle growth experiments. The growth of the single gold nanosphere in the optical trap gave much bigger nanoparticle ($\sim 2\times$) within much shorter reaction time ($\sim 20\times$) in comparison to the bulk growth at room temperature.

The plasmonic heating effect of optically trapped nanoparticles was able to enhance and modify the particle surface chemical reactions. By adjusting the trapping laser power, the optically heated nanoparticle temperature could be varied, thus influencing the outcome and the kinetics of the reactions. The optical trap provided the single gold nanoparticle a minimized free-standing reaction volume within the solution, where the temperature of the reaction volume was determined by the laser power and the particle absorption coefficient. Since the kinetics and the reaction rate depended on the particle temperature, they were ultimately determined by the applied laser power. This method can be applied to realize many temperature dependent reactions in the vicinity of particle surfaces. The optical trapping can also be combined with nanofluidic systems, opening the possibility to perform laser controlled single particle fabrication in nanofluidic devices. Furthermore, the kinetics of single particle reactions can be investigated in the single particle level, due to the optical confinement of the nanoparticle in the free standing solution.

The optical manipulation of gold nanoparticles was further applied to living cells. A controlled and versatile strategy has been developed to bind individual gold nanoparticles to lipids in living cell membranes. This labeling method was

based on the PEGylation of CTAB-stabilized gold nanoparticles to functionalize the particle surfaces with maleimide functional groups, which bound the nanoparticle to lipids in fusogenic vesicles via maleimide-thiol binding prior to vesicle/cell membrane fusogenesis. The covalent binding between the nanoparticle and the lipid molecule on the cell membrane avoided the nonspecific, uncontrolled attachment of the nanoparticles to random cell membrane components, while retaining the full capabilities for optothermal manipulation in living cells. This strategy may be exploited to incorporate CTAB-stabilized colloids of varying composition, size, or shape onto cellular membranes and provides a powerful toolbox for the mapping, local sensing and manipulation of cell membrane processes.

The optothermal properties of gold nanoparticles allow for manipulating the individual Au nanosphere that has been labeled to PTE-SH lipids in the living cell membranes optically. The gold nanoparticles were both optical markers for dark field observations and local heating sources for laser manipulations. The diffusion behavior of the labeling gold nanoparticles changed dramatically upon optical heating. The lipid diffused slowly within a spatially confined area of the cell surface at room temperature. However, after heating the local cellular membrane to 60°C for more than one minute, the diffusion of the lipid started to accelerate along a longer distance on the cell membrane. As this transition was irreversible, the possibility of membrane phase transition seems to have little influence on this observation. Further experiments on the cells without the cytoskeleton suggested that the influence of cytoskeleton could hinder the lipid diffusion on the membrane. Although it is still unclear at this stage whether the accelerated Au NP diffusion upon localized heating is induced by changes of cytoskeleton or other biological factors such as membrane proteins, we have shown that the optical heating was able to manipulate the Au NPs on cellular membrane surface. The plasmonic heating of the gold nanoparticles covalently labeled to cell membrane provides a multifunctional tool to both manipulate the cell membrane and to investigate the membrane response upon local heating.

Bibliography

- [1] U. Leonhardt. Optical metamaterials: Invisibility cup. *Nature Photonics*, 1(4):207–208, April 2007.
- [2] M. Faraday. The bakerian lecture: Experimental relations of gold (and other metals) to light. *Philosophical Transactions of the Royal Society of London*, 147(0):145–181, January 1857.
- [3] J. Turkevich, P. C. Stevenson, and J. Hillier. A study of the nucleation and growth processes in the synthesis of colloidal gold. *Discussions of the Faraday Society*, 11:55, 1951.
- [4] T. Klar, M. Perner, S. Grosse, G. von Plessen, W. Spirkl, and J. Feldmann. Surface-plasmon resonances in single metallic nanoparticles. *Physical Review Letters*, 80(19):4249–4252, May 1998.
- [5] C. Sönnichsen, S. Geier, N. E. Hecker, G. von Plessen, J. Feldmann, H. Ditlbacher, B. Lamprecht, J. R. Krenn, F. R. Aussenegg, V. Z-H. Chan, J. P. Spatz, and M. Möller. Spectroscopy of single metallic nanoparticles using total internal reflection microscopy. *Applied Physics Letters*, 77(19):2949, 2000.
- [6] J. Gao, C. M. Bender, and C. J. Murphy. Dependence of the gold nanorod aspect ratio on the nature of the directing surfactant in aqueous solution. *Langmuir*, 19(21):9065–9070, October 2003.
- [7] J. E. Millstone, S. Park, K. L. Shuford, L. Qin, G. C. Schatz, and C. A. Mirkin. Observation of a quadrupole plasmon mode for a colloidal solution of gold nanoprisms. *Journal of the American Chemical Society*, 127(15):5312–5313, April 2005.
- [8] S. A. Maier. *Plasmonics : fundamentals and applications*. Springer, New York, NY, 2007.
- [9] M. Meier and A. Wokaun. Enhanced fields on large metal particles: dynamic depolarization. *Optics Letters*, 8(11):581, November 1983.

- [10] A. Dahlin, M. Zach, T. Rindzevicius, M. Kall, D. S. Sutherland, and F. Hook. Localized surface plasmon resonance sensing of lipid-membrane-mediated biorecognition events. *Journal of the American Chemical Society*, 127(14):5043–5048, April 2005.
- [11] J. N. Anker, W. P. Hall, O. Lyandres, N. C. Shah, J. Zhao, and R. P. Van Duyne. Biosensing with plasmonic nanosensors. *Nature Materials*, 7(6):442–453, June 2008.
- [12] X. Huang, I. H. El-Sayed, W. Qian, and M. A. El-Sayed. Cancer cell imaging and photothermal therapy in the near-infrared region by using gold nanorods. *Journal of the American Chemical Society*, 128(6):2115–2120, February 2006.
- [13] A. S. Angelatos, B. Radt, and F. Caruso. Light-responsive Polyelectrolyte/Gold nanoparticle microcapsules. *The Journal of Physical Chemistry B*, 109(7):3071–3076, February 2005.
- [14] D. P. O’Neal, L. R. Hirsch, N. J. Halas, J. D. Payne, and J. L. West. Photothermal tumor ablation in mice using near infrared-absorbing nanoparticles. *Cancer Letters*, 209(2):171–176, June 2004.
- [15] T. Niidome, M. Yamagata, Y. Okamoto, Y. Akiyama, H. Takahashi, T. Kawano, Y. Katayama, and Y. Niidome. PEG-modified gold nanorods with a stealth character for in vivo applications. *Journal of Controlled Release*, 114(3):343–347, September 2006.
- [16] K. Svoboda and S. M. Block. Optical trapping of metallic rayleigh particles. *Optics Letters*, 19(13):930, July 1994.
- [17] K. Sasaki, J. Hotta, K. Wada, and H. Masuhara. Analysis of radiation pressure exerted on a metallic particle within an evanescent field. *Optics Letters*, 25(18):1385, September 2000.
- [18] P. M. Hansen, V. K. Bhatia, N. Harrit, and L. B. Oddershede. Expanding the optical trapping range of gold nanoparticles. *Nano Letters*, 5(10):1937–1942, October 2005.
- [19] M. Righini, A. S. Zelenina, C. Girard, and R. Quidant. Parallel and selective trapping in a patterned plasmonic landscape. *Nature Physics*, 3(7):477–480, May 2007.

-
- [20] M. L. Juan, R. Gordon, Y. Pang, F. Eftekhari, and R. Quidant. Self-induced back-action optical trapping of dielectric nanoparticles. *Nature Physics*, 5(12):915–919, October 2009.
- [21] B. L. Frey, C. E. Jordan, S. Kornguth, and R. M. Corn. Control of the specific adsorption of proteins onto gold surfaces with Poly(L-lysine) monolayers. *Analytical Chemistry*, 67(24):4452–4457, December 1995.
- [22] J. Chen, D. Wang, J. Xi, L. Au, A. Siekkinen, A. Warsen, Z.-Y Li, H. Zhang, Y. Xia, and X. Li. Immuno gold nanocages with tailored optical properties for targeted photothermal destruction of cancer cells. *Nano Letters*, 7(5):1318–1322, May 2007.
- [23] A. M. Gobin, M. H. Lee, N. J. Halas, W. D. James, R. A. Drezek, and J. L. West. Near-infrared resonant nanoshells for combined optical imaging and photothermal cancer therapy. *Nano Letters*, 7(7):1929–1934, July 2007.
- [24] C. M. Pitsillides, E. K. Joe, X. Wei, R. R. Anderson, and C. P. Lin. Selective cell targeting with light-absorbing microparticles and nanoparticles. *Biophysical Journal*, 84(6):4023–4032, June 2003.
- [25] C. Sönnichsen, T. Franzl, T. Wilk, G. von Plessen, and J. Feldmann. Drastic reduction of plasmon damping in gold nanorods. *Physical Review Letters*, 88(7), January 2002.
- [26] S. Schultz, D. R. Smith, J. J. Mock, and D. A. Schultz. Single-target molecule detection with nonbleaching multicolor optical immunolabels. *Proceedings of the National Academy of Sciences*, 97(3):996–1001, February 2000.
- [27] A. S. Urban, M. Fedoruk, M. R. Horton, J. O. Rädler, F. D. Stefani, and J. Feldmann. Controlled nanometric phase transitions of phospholipid membranes by plasmonic heating of single gold nanoparticles. *Nano Letters*, 9(8):2903–2908, August 2009.
- [28] M. Beversluis, A. Bouhelier, and L. Novotny. Continuum generation from single gold nanostructures through near-field mediated intraband transitions. *Physical Review B*, 68(11), September 2003.
- [29] U. Kreibig and M. Vollmer. *Optical properties of metal clusters*. Springer, Berlin; New York, 1995.
- [30] P. B. Johnson and R. W. Christy. Optical constants of the noble metals. *Physical Review B*, 6(12):4370–4379, December 1972.

- [31] J. C. Maxwell. On physical lines of force. *Philosophical magazine*, 21&23:Part I &II; Part III&IV, 1861.
- [32] G. Mie. Beiträge zur optik trüber medien, speziell kolloidaler metallösungen. *Annalen der Physik*, 330(3):377–445, 1908.
- [33] H. C. van de Hulst. *Light scattering by small particles*. Dover Publications, New York, 1981.
- [34] M. Quninten. Mqmie 2.4. MQMie 2.4: Aldenhoven, 2004.
- [35] R. Gans. Über die form ultramikroskopischer goldteilchen. *Annalen der Physik*, 342(5):881–900, 1912.
- [36] K. Yee. Numerical solution of initial boundary value problems involving maxwell’s equations in isotropic media. *IEEE Transactions on Antennas and Propagation*, 14(3):302–307, May 1966.
- [37] A. Taflove. Application of the finite-difference time-domain method to sinusoidal steady-state electromagnetic-penetration problems. *IEEE Transactions on Electromagnetic Compatibility*, EMC-22(3):191–202, August 1980.
- [38] D. M. Sullivan, O. P. Gandhi, and A. Taflove. Use of the finite-difference time-domain method for calculating EM absorption in man models. *IEEE Transactions on Bio-Medical Engineering*, 35(3):179–186, March 1988.
- [39] Allen Taflove and Susan C Hagness. *Computational electrodynamics : the finite-difference time-domain method*. Artech House, Boston, 2005.
- [40] D. M. Sullivan and IEEE Microwave Theory and Techniques Society. *Electromagnetic simulation using the FDTD method*. IEEE Press, New York, 2000.
- [41] C. Oubre and P. Nordlander. Optical properties of metallodielectric nanostructures calculated using the finite difference time domain method. *The Journal of Physical Chemistry B*, 108(46):17740–17747, November 2004.
- [42] A. Ditkowski, K. Dridi, and J.S. Hesthaven. Convergent cartesian grid methods for maxwell’s equations in complex geometries. *Journal of Computational Physics*, 170(1):39–80, June 2001.
- [43] Lumerical fdtd solutions 7.5. Lumerical FDTD solutions 7.5:Lumerical Solutions Inc., 2011.

-
- [44] K. Puech, F.Z. Henari, W.J. Blau, D. Duff, and G. Schmid. Investigation of the ultrafast dephasing time of gold nanoparticles using incoherent light. *Chemical Physics Letters*, 247(1-2):13–17, December 1995.
- [45] B. Lamprecht, A. Leitner, and F.R. Aussenegg. SHG studies of plasmon dephasing in nanoparticles. *Applied Physics B: Lasers and Optics*, 68(3):419–423, March 1999.
- [46] T. A. Klar, E. Dulkeith, and J. Feldmann. Time resolved fluorescence measurements of fluorophores close to metal nanoparticles. In Chris D. Geddes and Joseph R. Lakowicz, editors, *Radiative Decay Engineering*, volume 8, pages 249–273. Springer US, Boston, MA.
- [47] J. D. Jackson. *Classical electrodynamics*. Wiley, New York, 1999.
- [48] A. Wokaun, J. P. Gordon, and P. F. Liao. Radiation damping in surface-enhanced raman scattering. *Physical Review Letters*, 48(14):957–960, April 1982.
- [49] B. Persson and A. Baratoff. Theory of photon emission in electron tunneling to metallic particles. *Physical Review Letters*, 68(21):3224–3227, May 1992.
- [50] J. P. Wilcoxon, J. E. Martin, F. Parsapour, B. Wiedenman, and D. F. Kelley. Photoluminescence from nanosize gold clusters. *The Journal of Chemical Physics*, 108(21):9137, 1998.
- [51] E. Dulkeith, T. Niedereichholz, T. Klar, J. Feldmann, G. von Plessen, D. Gittins, K. Mayya, and F. Caruso. Plasmon emission in photoexcited gold nanoparticles. *Physical Review B*, 70(20), November 2004.
- [52] W. Fann, R. Storz, H. Tom, and J. Bokor. Electron thermalization in gold. *Physical Review B*, 46(20):13592–13595, November 1992.
- [53] H. Hoewel, S. Fritz, A. Hilger, U. Kreibig, and M. Vollmer. Width of cluster plasmon resonances: Bulk dielectric functions and chemical interface damping. *Physical Review B*, 48(24):18178–18188, December 1993.
- [54] T. S. Ahmadi, S. L. Logunov, and M. A. El-Sayed. Picosecond dynamics of colloidal gold nanoparticles. *The Journal of Physical Chemistry*, 100(20):8053–8056, January 1996.
- [55] C.-K. Sun, F. Vallee, L. Acioli, E. Ippen, and J. Fujimoto. Femtosecond-tunable measurement of electron thermalization in gold. *Physical Review B*, 50(20):15337–15348, November 1994.

- [56] R. Schoenlein, W. Lin, J. Fujimoto, and G. Eesley. Femtosecond studies of nonequilibrium electronic processes in metals. *Physical Review Letters*, 58(16):1680–1683, April 1987.
- [57] S. D. Brorson, A. Kazeroonian, J. S. Moodera, D. W. Face, T. K. Cheng, E. P. Ippen, M. S. Dresselhaus, and G. Dresselhaus. Femtosecond room-temperature measurement of the electron-phonon coupling constant γ in metallic superconductors. *Physical Review Letters*, 64(18):2172–2175, April 1990.
- [58] A. G. Skirtach, C. Dejumat, D. Braun, A. S. Susa, A. L. Rogach, W. J. Parak, H. Moehwald, and G. B. Sukhorukov. The role of metal nanoparticles in remote release of encapsulated materials. *Nano Letters*, 5(7):1371–1377, July 2005.
- [59] A. O. Govorov, W. Zhang, T. Skeini, H. Richardson, J. Lee, and N. A. Kotov. Gold nanoparticle ensembles as heaters and actuators: melting and collective plasmon resonances. *Nanoscale Research Letters*, 1(1):84–90, July 2006.
- [60] A. O. Govorov and H. H. Richardson. Generating heat with metal nanoparticles. *Nano Today*, 2(1):30–38, February 2007.
- [61] COMSOL Multiphysics 4.0:COMSOL Inc., 2010.
- [62] S. Chu, J. Bjorkholm, A. Ashkin, and A. Cable. Experimental observation of optically trapped atoms. *Physical Review Letters*, 57(3):314–317, July 1986.
- [63] A. Ashkin, J. M. Dziedzic, and T. Yamane. Optical trapping and manipulation of single cells using infrared laser beams. *Nature*, 330(6150):769–771, December 1987.
- [64] A. Ashkin and J. Dziedzic. Optical trapping and manipulation of viruses and bacteria. *Science*, 235(4795):1517–1520, March 1987.
- [65] A. Ashkin. Forces of a single-beam gradient laser trap on a dielectric sphere in the ray optics regime. *Biophysical Journal*, 61(2):569–582, February 1992.
- [66] T. Sugiura, T. Okada, Y. Inouye, O. Nakamura, and S. Kawata. Gold-bead scanning near-field optical microscope with laser-force position control. *Optics Letters*, 22(22):1663, November 1997.

-
- [67] H. Kuwata, H. Tamaru, K. Esumi, and K. Miyano. Resonant light scattering from metal nanoparticles: Practical analysis beyond rayleigh approximation. *Applied Physics Letters*, 83(22):4625, 2003.
- [68] S Thomas, A Predapais, S Casares, and T Brumeanu. Analysis of lipid rafts in t cells. *Molecular Immunology*, 41(4):399–409, June 2004.
- [69] Z. Korade and A. K. Kenworthy. Lipid rafts, cholesterol, and the brain. *Neuropharmacology*, 55(8):1265–1273, December 2008.
- [70] P. L. Yeagle. Modulation of membrane function by cholesterol. *Biochimie*, 73(10):1303–1310, October 1991.
- [71] P. L. Yeagle. *The Structure of Biological Membranes*. CRC Press, 2nd edition, 2004.
- [72] H. Lodish, A. Berk, S.L. Zipursky, P. Matsudaira, D. Baltimore, and J. Darnell. *Molecular Cell Biology*. 3rd. W.H.Freeman, 1996.
- [73] K. Gaus. Visualizing lipid structure and raft domains in living cells with two-photon microscopy. *Proceedings of the National Academy of Sciences*, 100(26):15554–15559, December 2003.
- [74] K. Murase, T. Fujiwara, Y. Umemura, K. Suzuki, R. Iino, H. Yamashita, M. Saito, H. Murakoshi, K. Ritchie, and A. Kusumi. Ultrafine membrane compartments for molecular diffusion as revealed by single molecule techniques. *Biophysical Journal*, 86(6):4075–4093, June 2004.
- [75] C. Dietrich, B. Yang, T. Fujiwara, A. Kusumi, and K. Jacobson. Relationship of lipid rafts to transient confinement zones detected by single particle tracking. *Biophysical Journal*, 82(1 Pt 1):274–284, January 2002.
- [76] Y. Sako and A. Kusumi. Compartmentalized structure of the plasma membrane for receptor movements as revealed by a nanometer-level motion analysis. *The Journal of Cell Biology*, 125(6):1251–1264, June 1994.
- [77] P. J. Quinn and C. Wolf. An x-ray diffraction study of model membrane raft structures. *FEBS Journal*, 277(22):4685–4698, November 2010.
- [78] L. J. Pike. The challenge of lipid rafts. *The Journal of Lipid Research*, 50(Supplement):S323–S328, December 2008.
- [79] E. London. Insights into lipid raft structure and formation from experiments in model membranes. *Current Opinion in Structural Biology*, 12(4):480–486, August 2002.

- [80] K. Simons and E. Ikonen. Functional rafts in cell membranes. *Nature*, 387(6633):569–572, June 1997.
- [81] A. Blume. Apparent molar heat capacities of phospholipids in aqueous dispersion. effects of chain length and head group structure. *Biochemistry*, 22(23):5436–5442, November 1983.
- [82] H. Trauble. Electrostatic effects on lipid phase transitions: Membrane structure and ionic environment. *Proceedings of the National Academy of Sciences*, 71(1):214–219, January 1974.
- [83] T. Heimburg. *Thermal biophysics of membranes*. Wiley-VCH ; John Wiley distributor, Weinheim; Chichester, 2007.
- [84] M. B. Jackson. *Molecular and cellular biophysics*. Cambridge University Press, Cambridge, 2006.
- [85] W. Rawicz, B.A. Smith, T.J. McIntosh, S.A. Simon, and E. Evans. Elasticity, strength, and water permeability of bilayers that contain raft microdomain-forming lipids. *Biophysical Journal*, 94(12):4725–4736, June 2008.
- [86] A. Einstein. Ueber die von der molekularkinetischen theorie der waerme geforderte bewegung von in ruhenden fluessigkeiten suspendierten teilchen. *Annalen der Physik*, 322(8):549–560, 1905.
- [87] M.J. Saxton and K. Jacobson. Single-particle tracking: applications to membrane dynamics. *Annual Review of Biophysics and Biomolecular Structure*, 26:373–399, 1997.
- [88] C. Dietrich, L.A. Bagatolli, Z.N. Volovyk, N.L. Thompson, M. Levi, K. Jacobson, and E. Gratton. Lipid rafts reconstituted in model membranes. *Biophysical Journal*, 80(3):1417–1428, March 2001.
- [89] A. E. Hac, H. M. Seeger, M. Fidorra, and T. Heimburg. Diffusion in two-component lipid membranes: A fluorescence correlation spectroscopy and monte carlo simulation study. *Biophysical Journal*, 88(1):317–333, January 2005.
- [90] W. L. Vaz, E. C. Melo, and T. E. Thompson. Translational diffusion and fluid domain connectivity in a two-component, two-phase phospholipid bilayer. *Biophysical journal*, 56(5):869–876, November 1989.

-
- [91] M. Eigen. Sorting single molecules: Application to diagnostics and evolutionary biotechnology. *Proceedings of the National Academy of Sciences*, 91(13):5740–5747, June 1994.
- [92] Th. Schmidt, G. J. Schuetz, W. Baumgartner, H. J. Gruber, and H. Schindler. Characterization of photophysics and mobility of single molecules in a fluid lipid membrane. *The Journal of Physical Chemistry*, 99(49):17662–17668, December 1995.
- [93] R. W. Fisher and T. L. James. Lateral diffusion of the phospholipid molecule in dipalmitoylphosphatidylcholine bilayers. an investigation using nuclear spin-lattice relaxation in the rotating frame. *Biochemistry*, 17(7):1177–1183, April 1978.
- [94] G. Orädd, G. Lindblom, and P. W. Westerman. Lateral diffusion of cholesterol and dimyristoylphosphatidylcholine in a lipid bilayer measured by pulsed field gradient NMR spectroscopy. *Biophysical journal*, 83(5):2702–2704, November 2002.
- [95] S. König, W. Pfeiffer, T. Bayerl, D. Richter, and E. Sackmann. Molecular dynamics of lipid bilayers studied by incoherent quasi-elastic neutron scattering. *Journal de Physique II*, 2(8):1589–1615, August 1992.
- [96] B. Nikoobakht and M. A. El-Sayed. Preparation and growth mechanism of gold nanorods (NRs) using seed-mediated growth method. *Chemistry of Materials*, 15(10):1957–1962, May 2003.
- [97] T. K. Sau and C. J. Murphy. Seeded high yield synthesis of short au nanorods in aqueous solution. *Langmuir*, 20(15):6414–6420, July 2004.
- [98] C.-K. Tsung, X. Kou, Q. Shi, J. Zhang, M. H. Yeung, J. Wang, and G. D. Stucky. Selective shortening of single-crystalline gold nanorods by mild oxidation. *Journal of the American Chemical Society*, 128(16):5352–5353, April 2006.
- [99] W. Ni, X. Kou, Z. Yang, and J. Wang. Tailoring longitudinal surface plasmon wavelengths, scattering and absorption cross sections of gold nanorods. *ACS Nano*, 2(4):677–686, April 2008.
- [100] J. Rodríguez-Fernández, J. Pérez-Juste, F. J. García de Abajo, and L. M. Liz-Marzán. Seeded growth of submicron au colloids with quadrupole plasmon resonance modes. *Langmuir*, 22(16):7007–7010, August 2006.

- [101] N. R. Jana, L. Gearheart, and C. J. Murphy. Seeding growth for size control of 5-40 nm diameter gold nanoparticles. *Langmuir*, 17(22):6782–6786, October 2001.
- [102] W. P. Wuelfing, S. M. Gross, D. T. Miles, and R. W. Murray. Nanometer gold clusters protected by surface-bound monolayers of thiolated poly(ethylene glycol) polymer electrolyte. *Journal of the American Chemical Society*, 120(48):12696–12697, December 1998.
- [103] C. R. Miller, B. Bondurant, S. D. McLean, K. A. McGovern, and D. F. O'Brien. Liposome-cell interactions in vitro: effect of liposome surface charge on the binding and endocytosis of conventional and sterically stabilized liposomes. *Biochemistry*, 37(37):12875–12883, September 1998.
- [104] M. J. Murcia, D. E. Minner, G.-M. Mustata, K. Ritchie, and C. A. Naumann. Design of quantum dot-conjugated lipids for long-term, high-speed tracking experiments on cell surfaces. *Journal of the American Chemical Society*, 130(45):15054–15062, November 2008.
- [105] T. Pott, H. Bouvrais, and P. Méléard. Giant unilamellar vesicle formation under physiologically relevant conditions. *Chemistry and Physics of Lipids*, 154(2):115–119, August 2008.
- [106] U. Schneider, H. U. Schwenk, and G. Bornkamm. Characterization of EBV-genome negative "null" and "T" cell lines derived from children with acute lymphoblastic leukemia and leukemic transformed non-hodgkin lymphoma. *International Journal of Cancer. Journal International Du Cancer*, 19(5):621–626, May 1977.
- [107] T. G. Baier, E. W. Jenne, W. Blum, D. Schönberg, and K. K. Hartmann. Influence of antibodies against IGF-I, insulin or their receptors on proliferation of human acute lymphoblastic leukemia cell lines. *Leukemia Research*, 16(8):807–814, August 1992.
- [108] R. T. Abraham and A. Weiss. Jurkat t cells and development of the t-cell receptor signalling paradigm. *Nature Reviews. Immunology*, 4(4):301–308, April 2004.
- [109] A. Weiss, R. L. Wiskocil, and J. D. Stobo. The role of t3 surface molecules in the activation of human t cells: a two-stimulus requirement for IL 2 production reflects events occurring at a pre-translational level. *Journal of Immunology (Baltimore, Md.: 1950)*, 133(1):123–128, July 1984.

-
- [110] A. Ashkin, J. M. Dziedzic, J. E. Bjorkholm, and Steven Chu. Observation of a single-beam gradient force optical trap for dielectric particles. *Optics Letters*, 11(5):288, May 1986.
- [111] H. Misawa, M. Koshioka, K. Sasaki, N. Kitamura, and H. Masuhara. Spatial pattern formation, size selection, and directional flow of polymer latex particles by laser trapping technique. *Chemistry Letters*, (3):469–472, 1991.
- [112] M. Friese, J. Enger, H. Rubinsztein-Dunlop, and N. Heckenberg. Optical angular-momentum transfer to trapped absorbing particles. *Physical Review A*, 54(2):1593–1596, August 1996.
- [113] A. Ashkin, K. Schütze, J. M. Dziedzic, U. Euteneuer, and M. Schliwa. Force generation of organelle transport measured in vivo by an infrared laser trap. *Nature*, 348(6299):346–348, November 1990.
- [114] M. P. Houlne, C. M. Sjoström, R. H. Uibel, J. A. Kleimeyer, and J. M. Harris. Confocal raman microscopy for monitoring chemical reactions on single optically trapped, solid-phase support particles. *Analytical Chemistry*, 74(17):4311–4319, September 2002.
- [115] C. Hrelescu, T. K. Sau, A. L. Rogach, F. Jäckel, G. Laurent, L. Douillard, and F. Charra. Selective excitation of individual plasmonic hotspots at the tips of single gold nanostars. *Nano Letters*, 11(2):402–407, February 2011.
- [116] P. Anger, P. Bharadwaj, and L. Novotny. Enhancement and quenching of single-molecule fluorescence. *Physical Review Letters*, 96(11), March 2006.
- [117] C. Hrelescu, T. K. Sau, A. L. Rogach, F. Jäckel, and J. Feldmann. Single gold nanostars enhance raman scattering. *Applied Physics Letters*, 94(15):153113, 2009.
- [118] V. Faessler, C. Hrelescu, A.A. Lutich, L. Osinkina, S. Mayilo, F. Jäckel, and J. Feldmann. Accelerating fluorescence resonance energy transfer with plasmonic nanoresonators. *Chemical Physics Letters*, 508(1-3):67–70, May 2011.
- [119] N. Harris, M. J. Ford, and M. B. Cortie. Optimization of plasmonic heating by gold nanospheres and nanoshells. *The Journal of Physical Chemistry B*, 110(22):10701–10707, June 2006.
- [120] A. Kyrsting, P. M. Bendix, D. G. Stamou, and L. B. Oddershede. Heat profiling of three-dimensionally optically trapped gold nanoparticles using vesicle cargo release. *Nano Letters*, 11:888–892, February 2011.

- [121] H. Petrova, J. Perez Juste, I. Pastoriza-Santos, G. V. Hartland, L. M. Liz-Marzán, and P. Mulvaney. On the temperature stability of gold nanorods: comparison between thermal and ultrafast laser-induced heating. *Physical Chemistry Chemical Physics*, 8(7):814, 2006.
- [122] K.J. Laidler. *Chemical Kinetics*. Benjamin-Cummings Pub Co, 1997.
- [123] W. Ni, X. Kou, Z. Yang, and J. Wang. Tailoring longitudinal surface plasmon wavelengths, scattering and absorption cross sections of gold nanorods. *ACS Nano*, 2(4):677–686, April 2008.
- [124] L. Gou and C. J. Murphy. Fine-tuning the shape of gold nanorods. *Chemistry of Materials*, 17(14):3668–3672, July 2005.
- [125] A. Kyrsting, P. M. Bendix, D. G. Stamou, and L. B. Oddershede. Heat profiling of three-dimensionally optically trapped gold nanoparticles using vesicle cargo release. *Nano Letters*, 11:888–892, feb 2011.
- [126] P. M. Bendix, S. N. S. Reihani, and L. B. Oddershede. Direct measurements of heating by electromagnetically trapped gold nanoparticles on supported lipid bilayers. *ACS Nano*, 4:2256–2262, April 2010.
- [127] A. Yariv and P. Yeh. *Photonics: Optical Electronics in Modern Communications*. Oxford University Press, 6 edition, 2007.
- [128] A. K. Ohlinger. *Akustik mit optisch gefangenen Nanopartikeln*. Shaker, 2011.
- [129] K. C. Neuman and S. M. Block. Optical trapping. *Review of Scientific Instruments*, 75(9):2787, 2004.
- [130] K. Berg-Sorensen and H. Flyvbjerg. Power spectrum analysis for optical tweezers. *Review of Scientific Instruments*, 75(3):594, 2004.
- [131] J. Stehr, C. Hrelescu, R. A. Sperling, G. Raschke, M. Wunderlich, A. Nichtl, D. Heindl, K. Kürzinger, W. J. Parak, T. A. Klar, and J. Feldmann. Gold NanoStoves for microsecond DNA melting analysis. *Nano Letters*, 8(2):619–623, February 2008.
- [132] A. J. deMello. Control and detection of chemical reactions in microfluidic systems. *Nature*, 442(7101):394–402, July 2006.
- [133] P. S. Dittrich and A. Manz. Lab-on-a-chip: microfluidics in drug discovery. *Nature reviews. Drug discovery*, 5(3):210–218, March 2006.

-
- [134] N. Kitamura and F. Kitagawa. Optical trapping:chemical analysis of single microparticles in solution. *Journal of Photochemistry and Photobiology C: Photochemistry Reviews*, 4(3):227–247, December 2003.
- [135] H. Craighead. Future lab-on-a-chip technologies for interrogating individual molecules. *Nature*, 442(7101):387–393, July 2006.
- [136] J. El-Ali, P. K. Sorger, and K. F. Jensen. Cells on chips. *Nature*, 442(7101):403–411, July 2006.
- [137] R. Riehn. Restriction mapping in nanofluidic devices. *Proceedings of the National Academy of Sciences*, 102(29):10012–10016, June 2005.
- [138] W. Reisner, N. B. Larsen, A. Silahatoglu, A. Kristensen, N. Tommerup, J. O. Tegenfeldt, and H. Flyvbjerg. Single-molecule denaturation mapping of DNA in nanofluidic channels. *Proceedings of the National Academy of Sciences*, 107(30):13294–13299, July 2010.
- [139] R. Ranganathan. Signaling across the cell membrane. *Science*, 318(5854):1253–1254, November 2007.
- [140] Fabien Pinaud, David King, Hsiao-Ping Moore, and Shimon Weiss. Bioactivation and cell targeting of semiconductor CdSe/ZnS nanocrystals with phytochelatin-related peptides. *Journal of the American Chemical Society*, 126(19):6115–6123, May 2004.
- [141] G. Gopalakrishnan, C. Danelon, P. Izewska, M. Prummer, P.-Y. Bolinger, I. Geissbuehler, D. Demurtas, J. Dubochet, and H. Vogel. Multifunctional Lipid/Quantum dot hybrid nanocontainers for controlled targeting of live cells. *Angewandte Chemie International Edition*, 45(33):5478–5483, August 2006.
- [142] R. J. Mannix, S. Kumar, F. Cassiola, M. Montoya-Zavala, E. Feinstein, M. Prentiss, and D. E. Ingber. Nanomagnetic actuation of receptor-mediated signal transduction. *Nature Nanotechnology*, 3(1):36–40, December 2007.
- [143] N. A. Kotov, J. O. Winter, I. P. Clements, E. Jan, B. P. Timko, S. Campidelli, S. Pathak, A. Mazzatenta, C. M. Lieber, M. Prato, R. V. Bellamkonda, G. A. Silva, N. W. S. Kam, F. Patolsky, and L. Ballerini. Nanomaterials for neural interfaces. *Advanced Materials*, 21(40):3970–4004, October 2009.

- [144] R. A. Sperling, P. Rivera Gil, F. Zhang, M. Zanella, and W. J. Parak. Biological applications of gold nanoparticles. *Chemical Society Reviews*, 37(9):1896, 2008.
- [145] R. A. Alvarez-Puebla and L. M. Liz-Marzán. SERS-Based diagnosis and biodetection. *Small*, 6(5):604–610, March 2010.
- [146] C. Yao, R. Rahmzadeh, E. Endl, Z. Zhang, J. Gerdes, and G. Hüttmann. Elevation of plasma membrane permeability by laser irradiation of selectively bound nanoparticles. *Journal of Biomedical Optics*, 10(6):064012, 2005.
- [147] E. C. Cho, J. Xie, P. A. Wurm, and Y. Xia. Understanding the role of surface charges in cellular adsorption versus internalization by selectively removing gold nanoparticles on the cell surface with a $\text{H}_2\text{O}_2/\text{KI}$ etchant. *Nano Letters*, 9(3):1080–1084, March 2009.
- [148] C. Lee, M. Chen, J. Cheng, and P. Wei. Morphological studies of living cells using gold nanoparticles and dark-field optical section microscopy. *Journal of Biomedical Optics*, 14(3):034016, 2009.
- [149] M. Grzelczak, J. Pérez-Juste, P. Mulvaney, and L. M. Liz-Marzán. Shape control in gold nanoparticle synthesis. *Chemical Society Reviews*, 37(9):1783, 2008.
- [150] M. Grzelczak, J. Pérez-Juste, B. Rodríguez-González, M. Spasova, I. Bar-sukov, M. Farle, and L. M. Liz-Marzán. Pt-catalyzed growth of ni nanoparticles in aqueous CTAB solution. *Chemistry of Materials*, 20(16):5399–5405, August 2008.
- [151] H. Otsuka, Y. Nagasaki, and K. Kataoka. PEGylated nanoparticles for biological and pharmaceutical applications. *Advanced Drug Delivery Reviews*, 55(3):403–419, February 2003.
- [152] B. L. Frey and R. M. Corn. Covalent attachment and derivatization of Poly(L-lysine) monolayers on gold surfaces as characterized by Polarization-Modulation FT-IR spectroscopy. *Analytical Chemistry*, 68(18):3187–3193, January 1996.
- [153] S. Xiao, S. Brunner, and M. Wieland. Reactions of surface amines with heterobifunctional cross-linkers bearing both succinimidyl ester and maleimide for grafting biomolecules. *The Journal of Physical Chemistry B*, 108(42):16508–16517, October 2004.

-
- [154] G. Mattson, E. Conklin, S. Desai, G. Nielander, M. D. Savage, and S. Morgensen. A practical approach to crosslinking. *Molecular Biology Reports*, 17(3):167–183, April 1993.
- [155] S.-J. Xiao, M. Wieland, and S. Brunner. Surface reactions of 4-aminothiophenol with heterobifunctional crosslinkers bearing both succinimidyl ester and maleimide for biomolecular immobilization. *Journal of Colloid and Interface Science*, 290(1):172–183, October 2005.
- [156] A. Kusumi, C. Nakada, K. Ritchie, K. Murase, K. Suzuki, H. Murakoshi, R. S. Kasai, J. Kondo, and T. Fujiwara. Paradigm shift of the plasma membrane concept from the two-dimensional continuum fluid to the partitioned fluid: High-speed single-molecule tracking of membrane molecules. *Annual Review of Biophysics and Biomolecular Structure*, 34(1):351–378, June 2005.
- [157] M. R. Bubb, I. Spector, B. B. Beyer, and K. M. Fosen. Effects of jasplakinolide on the kinetics of actin polymerization. an explanation for certain in vivo observations. *The Journal of biological chemistry*, 275(7):5163–5170, February 2000.
- [158] D. Bartczak, O. L. Muskens, T. M. Millar, T. Sanchez-Elsner, and A. G. Kanaras. Laser-induced damage and recovery of plasmonically targeted human endothelial cells. *Nano Letters*, 11(3):1358–1363, March 2011.
- [159] Helen L. Yin and Paul A. Janmey. Phosphoinositide regulation of the actin cytoskeleton. *Annual Review of Physiology*, 65(1):761–789, March 2003.
- [160] A. M. Goldyn, B. A. Rioja, J. P. Spatz, C. Ballestrem, and R. Kemker. Force-induced cell polarisation is linked to RhoA-driven microtubule-independent focal-adhesion sliding. *Journal of Cell Science*, 122(20):3644–3651, October 2009.
- [161] A. Bettaieb and D. A. Averill-Bates. Thermotolerance induced at a fever temperature of 40 degrees c protects cells against hyperthermia-induced apoptosis mediated by death receptor signalling. *Biochemistry and Cell Biology (Biochimie Et Biologie Cellulaire)*, 86(6):521–538, December 2008.
- [162] J. R Lepock. How do cells respond to their thermal environment? *International journal of hyperthermia: the official journal of European Society for Hyperthermic Oncology, North American Hyperthermia Group*, 21(8):681–687, December 2005.

Bibliography

- [163] H. H. Kampinga. Thermotolerance in mammalian cells. protein denaturation and aggregation, and stress proteins. *Journal of cell science*, 104 (Pt 1):11–17, January 1993.

Acknowledgements

It was a great experience to do Ph.D research in this inter-culture and interdisciplinary group. There are nice memories of excellent moments involving many people that I would like to give thanks to.

First I would like to thank my supervisor Prof. Jochen Feldmann, for giving me the opportunity to work in his group and providing abundant supports in funding and scientific resources. I really appreciate the inspiring and fruitful conversations with him and I benefited a lot from these discussions.

Thanks to Dr. Jessica Rodríguez-Fernández, Dr. Andrey Lutich and Dr. Fernando Stefani, three assistants who supervised my experiments during my Ph.D time. Discussions with them made crucial steps for deeper understandings of different aspects of my work. Thanks to Dr. Jessica Rodríguez-Fernández and Dr. Frank Jäckel for their advises and proof-reading of my thesis; to Dr. Theobald Lohmüller for his comments and fresh input to improve my experiments.

Thanks to Prof. Hermann Gaub who generously allowed me to get access to cell facilities in his lab. Expressed thanks to technicians Thomas Nicolaus and Angelika Kardinal for their friendly help with cell cultures, and to Susanne Kempter for helping me with the TEM.

Thanks to Dr. Joachim Stehr, Dr. Carlin Hrelescu and Dr. Alexander Urban, former Ph.D students of the group whose knowledge and experience inspired my work. Many thanks to Dr. Alexander Ohlinger, my former officemate for his expertized support on computer and pioneer exploration on softwares that benefited my work. Thanks to Dr. Weihai Ni and Lizhe Liu, for the nice teamwork and lab experience we had together. Thanks to Michael Fedoruk, Spas Nedev and Dr. Sol Carretero Palacios for fruitful discussions on optical forces and optical heating and to Dr. Aliaksei Dubavik, Paul Kühler and Jaekwon Do for their encouragement. To my current officemate Felix Deschler, thanks for the brainstorming sharings and his support in German language.

Thanks to Ilka Kriegel, Lidiya Osinkina, Silke Kirchner, Shany Neyshtadt and Verena Baumann, for the nice moments in Girls' events; to Dr. Wei Li, Dr. Jianhong Zhang, and Dr. Haiyan Sun, my Chinese colleagues for the unforgettable happy moments we had together.

Thanks to Gerlinde Adam for her help on administration and to Anna Helfrich and Stefan Niedermaier for their technical support.

Acknowledgements

Last but not least, thanks to my family, especially my dear husband Kefei for his encouragement and accompany, and my parents who gave endless love and support to their daughter.

Erklärung

Ich erkläre hiermit, dass ich meine Dissertation mit dem Titel
**"Plasmonic Heating of Gold Nanoparticles in an Optical Trap and on
the Cell Membrane"**

selbständig verfasst, sowie keine anderen als die angegebenen Quellen und
Hilfsmittel benutzt habe.

München, den September 5, 2012

(Haojin Ba)

dissertation